New Hardware Avenues for Enabling Magnetic Resonance Thermometry Guided Radio Frequency Hyperthermia Treatment in Head & Neck

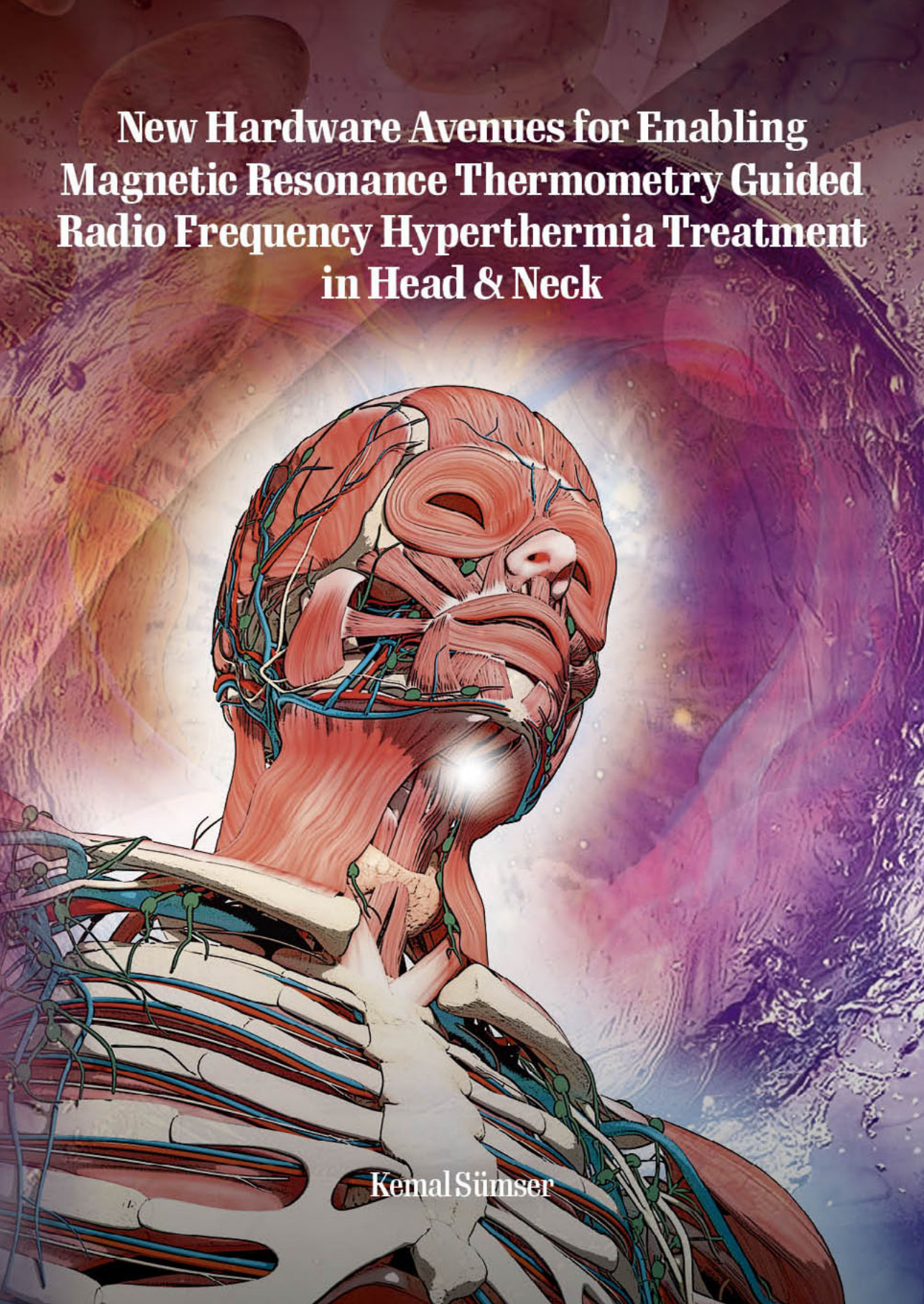

Kemal Sümser

NEW HARDWARE AVENUES FOR ENABLING MAGNETIC RESONANCE THERMOMETRY GUIDED RADIO FREQUENCY HYPERTHERMIA TREATMENT IN HEAD & NECK

Kemal Sümser

Colofon:

The investigations presented in this thesis were carried out at the Department of Radiation Oncology, Erasmus MC - Cancer Institute, Rotterdam.

This research was financially supported by the Technology Foundation STW (grant 10846) and the Dutch Cancer Society, grant EMCR2012-5472. Financial support for the printing of this thesis was provided by the Erasmus University Rotterdam.

Address for correspondence:
K. Sümser, Department of Radiotherapy: Unit Hyperthermia, Erasmus MC - Cancer Institute, P.O. Box 2040, 3000 CA Rotterdam, The Netherlands.
k.sumser@erasmusmc.nl

ISBN: 978-94-6416-533-3

Printed by: *Ridderprint | www.ridderprint.nl.*

New Hardware Avenues for Enabling Magnetic Resonance Thermometry Guided Radio Frequency Hyperthermia Treatment in the Head & Neck

Nieuwe hardware technologieen voor magnetische resonantie thermometrie-gestuurde radiofrequentie hyperthermie behandeling in het hoofd-hals gebied

Thesis

for the purpose of being admitted to the degree of Doctor at
Erasmus University Rotterdam
on the authority of the
rector magnificus

Prof.dr. F.A. van der Duijn Schouten

and in accordance with the decision of the Doctorate Board.

The public defence ceremony shall take place on
Tuesday 2 June 2021 at 15:30

by

Kemal Sümser

born in Ankara, Turkey

Erasmus University Rotterdam

Doctoral Committee

Promotors:	Prof. dr. ir. G.C. van Rhoon
	Prof. dr. J.A. Hernandez-Tamames
Other members:	Prof. dr. R.A. Nout
	Prof. dr. C.T.W. Moonen
	Assoc. prof. dr. D.S. Rivera
Co-promotor:	Assoc. prof. dr. ir. M.M. Paulides

Contents

Page

1 Introduction **9**
- 1.1 Head and Neck Cancer . . . 9
- 1.2 Clinical hyperthermia treatment . . . 10
- 1.3 Dosimetry in head and neck hyperthermia . . . 11
- 1.4 Approach . . . 13
- 1.5 Outline of this thesis . . . 15

Part I: Status quo and standardization **18**

2 State of the art in MR - RF hyperthermia **19**
- 2.1 Introduction . . . 21
- 2.2 Materials and Methods . . . 23
- 2.3 MR-guided RF HT devices . . . 24
  - 2.3.1 Decoupled devices (HT-only inserts) . . . 25
  - 2.3.2 Dual-function devices . . . 28
- 2.4 Discussion . . . 34
  - 2.4.1 Reporting of validation results . . . 35
  - 2.4.2 The further development of MRgRFHT . . . 37
- 2.5 Conclusion . . . 38

3 A new MR compatibility assessment procedure and clinical benchmark **41**
- 3.1 Introduction . . . 43
- 3.2 Material & Methods . . . 43
  - 3.2.1 Sigma Eye and Quality Assurance Phantom . . . 43
  - 3.2.2 Experimental Setup . . . 44

3.3 Results . . . 45
3.4 Discussion & Conclusions . . . 46

Part II: MR guided hyperthermia treatment 50

4 The need for MR thermometry in H&N hyperthermia 51
4.1 Introduction . . . 53
4.2 Methods . . . 54
4.2.1 Patient Data and Scan Protocols . . . 54
4.2.2 Arterial vessel tree segmentation . . . 54
4.2.3 Electromagnetic modeling and optimization . . . 55
4.2.4 Thermal modeling . . . 55
4.2.5 Evaluation parameters . . . 57
4.3 Results . . . 58
4.4 Discussion . . . 59
4.5 Conclusion . . . 63

5 Design of the MRcollar 65
5.1 Introduction . . . 67
5.2 Methods . . . 68
5.2.1 Antenna encasing - DiPRA module . . . 68
5.2.2 DiPRA module verification measurements . . . 69
5.2.3 MRcollar design . . . 70
5.2.4 MRcollar model heating capabilities . . . 71
5.2.5 MR assesment of antenna encasing - DiPRA module . . . 72
5.3 Results . . . 73
5.3.1 Antenna encasing - DiPRA module . . . 73
5.3.2 DiPRA module verification measurements . . . 74
5.3.3 MRcollar design . . . 74
5.3.4 MRcollar model heating capabilities . . . 74
5.3.5 MR assessment of antenna encasing - DiPRA module . . . 76
5.4 Discussion . . . 76
5.5 Conclusion . . . 81

6 Experimental assessment of the MRcollar 83
6.1 Introduction . . . 85
6.2 Materials and Methods . . . 86
6.2.1 Mechanical Design . . . 86
6.2.2 Phantoms . . . 86
6.2.3 Antenna Characterization Measurements, Heating and Focusing Steering Capabilities . . . 87
6.2.4 MR compatibility Measurements . . . 88

6.3 Results . . . 89
6.3.1 Reflection and cross-coupling measurements . . . 89
6.3.2 Heating, Steering Capabilities and Focus-Size . . . 89
6.3.3 MR Compatibility Measurements . . . 90
6.4 Discussion . . . 91
6.4.1 EM compatibility . . . 91
6.4.2 Heating Capabilities . . . 92
6.4.3 MR compatibility . . . 93
6.5 Conclusion . . . 94

Part III: New hardware avenues 98

7 Improving MR thermometry by optimizing waterbolus filling 99
7.1 Introduction . . . 101
7.2 Materials and Methods . . . 103
7.2.1 Requirements for the Water Bolus Fluid . . . 103
7.2.2 Preparation of the Samples . . . 103
7.2.3 MR Relaxometry Measurements . . . 103
7.2.4 Electromagnetic Property Measurements . . . 104
7.2.5 Effects on Power Deposition Pattern . . . 104
7.2.6 Effects on MRT Precision . . . 104
7.3 Results . . . 105
7.3.1 MR Relaxometry Measurements . . . 105
7.3.2 Electromagnetic Property Measurements . . . 105
7.3.3 Effects on SAR Patterns and Applicator Efficiency . . . 106
7.3.4 Effect on MRT Precision . . . 108
7.4 Discussion . . . 109
7.5 Conclusions . . . 112

8 Potential of multi-coil MRcollar 115
8.1 Introduction . . . 117
8.2 Materials and Methods . . . 118
8.2.1 Dual-Function Integrated Experimental System . . . 118
8.2.2 Experimental Setup . . . 119
8.3 Results . . . 122
8.3.1 Characterization of the Integrated System . . . 122
8.3.2 Heating Experiments . . . 123
8.3.3 MR Imaging Experiments . . . 123
8.4 Discussion . . . 125
8.5 Conclusion . . . 126

9 General discussion and perspectives **129**
9.1 Status quo and standardization in MR guided hyperthermia 129
9.2 MR guided hyperthermia in the head and neck 130
9.3 New hardware-avenues for MRT 130
9.4 Future outlook 131

Summary **135**

References **147**

List of Publications **173**

PhD portfolio **177**

Curriculum Vitae **181**

Acknowledgments **183**

CHAPTER 1

Introduction

1.1 Head and Neck Cancer

Cancer is the second leading cause of death worldwide and is responsible for about 1 in 6 deaths[1]. Worldwide ≈830.000 (≈4% of all cancer patients) patients suffering from cancer has a tumor in head and neck region[2]. Head and neck cancers are categorized in five regions, as illustrated in Figure 1.1.

90% of all head and neck cancers are due to head and neck squamous cell carcinomas[4]. Head and neck cancers are mainly associated with alcohol and tobacco use[5]. In current

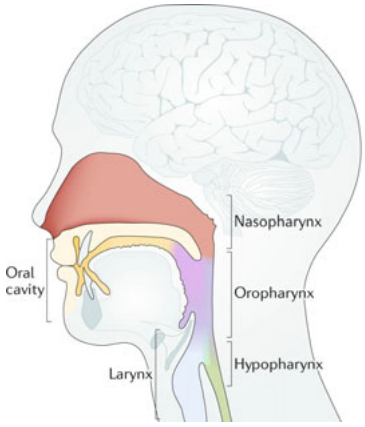

Figure 1.1: Head and neck cancer regions. Image from Cramer et al.[3]

clinical practice, tumors in the head and neck region are treated with surgery, radiotherapy, chemotherapy or a combination of them. Recent technological advances provided patients with multiple treatment options including the potential benefit of decreased morbidity.[3]. For postoperative treatment, the EORTC 22931 and the RTOG 9501 trials established adjuvant chemoradiotherapy with high-dose cisplatin and conventional fractionation radiotherapy (60 to 66 Gy) as the standard of care in high-risk patients with squamous-cell carcinoma of the head and neck[6]. Despite these efforts, still 30-40% of the patients experience recurrence or secondary tumor development[7]. Additionally, these treatments are associated with high late toxicities and side effects, such as difficulties in swallowing, speaking etc.[8,9]. Treatment of recurrent or secondary tumor remains a challenge due to an increased risk of radiotherapy-related normal tissue toxicities and tumor radioresistance[10]. Hence, therapeutic strategies that minimize toxicity while maintaining treatment outcome are desired.

1.2 Clinical hyperthermia treatment

The beneficial effects of chemotherapy and radiotherapy can be enhanced by heat treatments with no or minimal additional toxicity[11–13]. Hyperthermia treatment is used in combination with radiotherapy and/or chemotherapy by heating tumor sites to a supraphysiological level of 40-44 °C by applying external energy[14–18]. Hyperthermia is combined with radiotherapy and/or chemotherapy for its known enhancing effects on these modalities. Tumors cells under hypoxic conditions are resistant to radiotherapy and/or chemotherapy[19,20] due to lack of blood flow, oxygenation, and low pH distribution[21,22]. Firstly, hyperthermia increases the blood flow[23,24] and subsequently the blood flow increase triggers several mechanisms[25], it increases drug delivery[26], and improves oxygenation[27] and stimulates the immune response[28]. Also, the cells in environments with low oxygenation are specifically sensitivity for hyperthermia[29]. Moreover, DNA damage repair is inhibited at at temperatures of 41 °C and higher[30].

Clinical benefits of hyperthermia treatment in head and neck cancer is demonstrated by several studies[31–37]. A recent meta-analysis by Datta et al.[38] on hyperthermia and radiotherapy in the management of head and neck cancers found that overall complete response was improved from 39.6% (92/232) by radiotherapy alone to 62.5% (137/219) when radiotherapy was combined with hyperthermia. Of relevance to note is that late toxicity observed in these studies were similar.

Hyperthermia is achieved by application of internal or external energy. The most common type of applied external energy are radio frequency (RF) electromagnetic waves at frequencies below and above 300 MHz, i.e. microwaves (MW). Lately a growing interest exist to use ultrasound for heating for its high spatial control of energy deposition. Hyperthermia can be applied for superficial tumors (targets up to 4 cm from the skin surface) or for deep seated tumors (targets deeper than 4 cm from the skin surface)[39]. The heating target can be local, i.e. heating target is the tumor target volume itself or locoregional, i.e. heating target is the tumor target volume with an additional margin of normal tissue[40].

At Erasmus MC, three types of locoregional RF hyperthermia treatments are applied. The Lucid cone applicator (Figure 1.2a) is used to treat superficial tumors less than 4 cm from the skin, mainly in the chest wall. The BSD2000-3D and the MR compatible BSD2000-3D-MRI (Figure 1.2b) systems are used to treat deeply located cancers of the pelvis (e.g. cervix, rectum, vagina). Lastly, the HYPERcollar3D is being used for hyperthermia treatments in the head and neck region (Figure 1.2c).

Treatment of deep seated head and neck tumors at Erasmus MC started with the development of HYPERcollar[41]. Between February 2007 and July 2013, 27 patients were treated with the HYPERcollar[42] and received 119 treatments. 87% of the treatments were completed, proving that hyperthermia treatment of deep seated tumors at head and neck region is feasible. Based on this clinical experience plus the feedback of patient, technician and medical doctor, a complete overhaul of the HYPERcollar was made. The development of the HYPERcollar3D was completed in 2014[43,44]. A major advancement of the HYPERcollar3D entailed the increase in number of antennas from 12 to 20 to improve the focusing capabilities and reduce hotspots. Furthermore, a new water bolus concept was developed that has a much more reproducible shape and a tailored shape to provide unrestricted breathing[45]. Since its clinical introduction to the clinic in July 2014 until 2019, 22 patients have received 107 treatment sessions with the HYPERcollar3D.

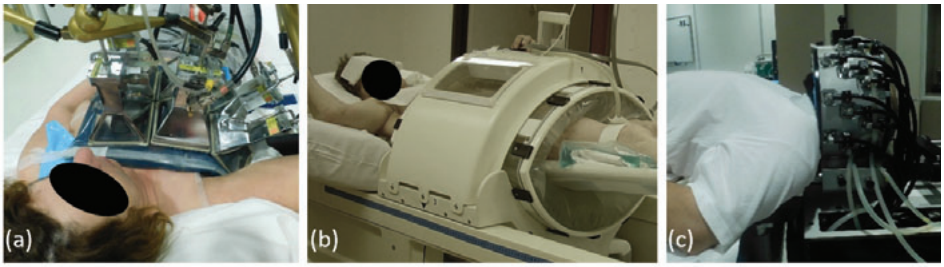

Figure 1.2: Hyperthermia applicators at the Erasmus MC (a) Lucid cone applicator, (b) BSD2000-3D, (c) HYPERcollar3D used to for treatment of superficial and deep (pelvic, head and neck) tumors.

1.3 Dosimetry in head and neck hyperthermia

Clinically demonstrated thermal dose effect relationships suggest that higher temperatures improve the treatment outcome[46–49]. During a hyperthermia treatment, tumor temperature is aimed to kept between 40-44 °C for 30 to 60 minutes[40,50,51]. Key to achieve a high thermal dose is to optimize treatment such that the energy delivery is focused at the target volume while healthy and sensitive tissues are kept below safety limits. The head and neck region includes several temperature sensitive organs (e.g. eyes, spinal cord) and has strong and

inhomogeneous thermoregulation. To achieve maximum treatment efficacy it is important to provide the clinician with advanced technology to be accurately informed on the applied thermal dose. In current clinical practice, we aim to achieve this by pre-treatment planning, real-time targeted energy deposition predictions and invasive temperature measurements.

Integral part of hyperthermia treatment at Erasmus MC is pre-treatment planning. Each patient receives personalized hyperthermia treatment to maximize targeted energy deposition as a part of standard clinical care[52]. This treatment workflow is illustrated in Figure 1.3 and starts with generating the numerical model of the patient from CT images[53,54]. By using the standard CT images available for radiotherapy treatment planning, the procedure for hyperthermia treatment planning is smoothly integrated in the patient preparation procedure. Then, in the simulation environment, this patient model is positioned inside the hyperthermia applicator, and the EM fields generated by each antenna are calculated using an electromagnetic simulator. Due to uncertainties and variations in thermal properties[55], amplitude and phase of the signal fed to each antenna are optimized to maximize the specific absorption rate (SAR) in the target region while minimizing the SAR in hotspots, i.e. those regions receiving the highest SAR in healthy tissues[52].

Predicted SAR hotspots do not always translate to temperature hotspots or patient complaints do not always correlates with the predicted location of the hotspots. The dose distribution of each setting is displayed on top of the image data so that the operator can correlate the location of the hotspot with the location of the complaint or too high temperature. Based on this information, the operator can place in real time a sensitive region and make a new adapted optimized treatment plan with a restriction for the allowed SAR at the indicated region[56]. This is implemented on our in-house developed online dosimetry tool, the Visualisation Tool for Electromagnetic Dosimetry and Optimization (VEDO)[52].

While SAR distributions provide valuable information, it is necessary to have temperature measurements for accurate dosimetry during the treatment. This is achieved whenever possible by invasive temperature measurements. Temperature probes are placed in closed tip catheters that are interstitially placed in the tumor or hotspot area. Out of 22 patients treated with HYPERcollar3D, only 5 had a probe in the target volume during a treatment

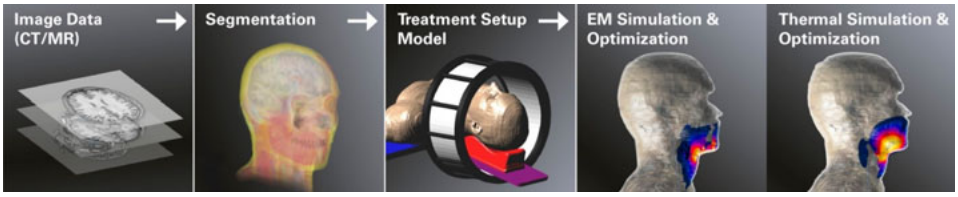

Figure 1.3: The hyperthermia treatment planning workflow. The process starts with imaging (CT and/or MR), followed by delineating the tissues to generate a 3D numerical model of the patient and ends with calculation of the SAR distribution that is optimized to deliver maximum treatment efficacy.

session. Temperature measurements are also desired at hotspot locations. In order to acquire a complete information, invasive temperature measurements needs to be made in multiple locations. This will allow clinician to see whether the focus of energy deposition is at the target and, also whether the temperature in hot spots is not too high, i.e. prevents toxicity. However, placement of invasive temperature probes has been extremely challenging and is often avoided due to possibility of complications[57]. Therefore, a non-invasive temperature imaging technique that can monitor multiple locations is highly desired.

Several non-invasive thermometry methods such as impedance tomography or microwave imaging were proposed for treatment monitoring during hyperthermia but only MR techniques have been applied clinically[58]. MR thermometry is not only a non-invasive temperature imaging technique but also monitors the temperature change in a volume. Hence, it can be used to monitor temperature both in tumor and in healthy tissue during the treatment. The 3D temperature increase information during the treatment can also be used to calculate thermal dose CEM43[59] or biological equivalent dose (BED)[60]. The desire to have non-invasive thermometry during head and neck hyperthermia prompted the development of an MR compatible applicator by altering the HYPERcollar design and led to the development of the MRlabcollar[61]. Large electric conductive surfaces in the HYPERcollar such as the ground-plane were reduced in size. The applicator was successfully adapted for RF heating and MR imaging. However, it was shown that the reduced metallic regions in the design still resulted in large dark regions. Further it was noted that circulation of water in the water boli will degrade the MR thermometry accuracy.

In summary, at the start of this project, real-time temperature dosimetry was only available through a limited number of temperature probes, i.e. mostly only a single catheter track with a multi-sensor probe and seldom in the target volume. 3D Dosimetry and guidance during the treatment relied on electromagnetic modeling which do not always translate into same temperature distributions. A clinical MR compatible head and neck hyperthermia applicator was non-existent. In addition, current approaches for MR thermometry guided hyperthermia lack the accuracy due to innate problems such as low SNR and signal degradation by the water circulation.

1.4 Approach

In this thesis first the needs to achieve precise application of MR thermometry guided head and neck hyperthermia are identified. Next new avenues for MRT guided head and neck RF hyperthermia are explored and experimentally validated. The research efforts in the thesis are grouped in three themes, each consisting of two or more chapters:

Part 1: Status quo and standardization in MR guided hyperthermia
During hyperthermia treatment the body's inhomogeneous and variable thermoregulation properties require close monitoring of temperature to optimize power distribution and sparing of healthy tissues. This is best achieved with non-invasive 3D thermometry since invasive

thermometry is hampered by accessibility related to critical organs (nerves, arteries, etc.) and the risk for toxicity. Hence, it is infeasible to insert the required amount of temperature probes needed for informative 3D thermometry. To this end, MR thermometry has been developed and integrated in hyperthermia treatments which resulted in several devices and approaches. For this thesis, all research work done in the field of magnetic resonance guided radio frequency hyperthermia has been reviewed in Chapter 2. This review attempts to highlight the technical advances, validation status and standards. Furthermore, we proposed standards on reporting the device validation both for EM and MRI compatibility. In Chapter 3, we quantitatively evaluated the MRI compatibility of BSD2000-3D-MRI, currently the only clinical used hybrid system for simultaneous RF-heating and MR-thermometry, to create a benchmark for MR compatible hyperthermia applicators.

Part 2: MR guided hyperthermia in the head and neck
Patient-specific head and neck (H&N) hyperthermia treatment planning (HTP) to maximize the EM energy inside the tumor while minimizing exposure of healthy tissues is the focal point of the Rotterdam treatment strategy. This procedure is based on power absorption-based optimization methods which does not take the patient specific vasculature information into account and might result in under delivery of thermal dose. To investigate the effect of the vasculature, we compared the effect on thermal simulations by incorporating the patient specific vasculature segmentation, showing the need for MR thermometry in head and neck in Chapter 4. In this regard, we integrated automatic segmentation of the blood vessels into our existing automatic tissue segmentation routine. Then, we compared the resultant hyperthermia treatment planning quality parameters with and without the inclusion of the vasculature to highlight the need for real-time dosimetry.

Erasmus MC Cancer Institute is the only center in the world that treats deep seated tumors with hyperthermia in the head and neck area with a phased array applicator since 2007. Application of the hyperthermia treatment to deeply located H&N tumors were and are administered using in house developed applicators, first the HYPERcollar and later using its successor the HYPERcollar3D. As shown in Chapter 4, thermoregulation in the head and neck region is strong and unpredictable. In addition, the head and neck region also includes several temperature sensitive tissues and organs. Therefore, temperature monitoring is highly desired by clinicians to see whether the focus of energy deposition is at the target and, also whether the temperature in hot spots is not too high. This prompted us develop an MRI compatible head and neck hyperthermia applicator, the MRcollar. A novel antenna module which minimizes the interaction with the scanner has been designed in silico in Chapter 5. Using this module, the MRcollar dimensions were optimized to the average hyperthermia patient. A prototype applicator has been built based on this design and we experimentally validated the numerical model and MR compatibility in Chapter 6.

Part 3: New hardware avenues for MRT
The potential of MR thermometry formed the fertile soil for development of the MRcollar in Part 2. However, early MRT accuracy experiments using the MRlabcollar demonstrated that existing approaches will not suffice for MRT accuracy in the H&N[61]. In this regard, we identified two key components that can improve MR thermometry. In Chapter 7, we

focused on optimizing the water bolus properties to reduce its effect on MRI imaging. While the water bolus is mandatory since it cools the patient skin and improves the delivery of the electromagnetic energy, it enforces enlarged field of view (reduced SNR, longer scanning time), skews pre-scan calibrations (inhomogeneous SNR), and its water flow creates flow artifacts (errors in temperature predictions). We explored a cost-effective solution to prevent these issues by altering its MRI properties with compounds that affect the MRI properties of their base solutions, while keeping EM behavior of the water bolus the same. As a second key enabler for accuracy, we identified that integration of receiver coils in the hyperthermia applicator might improve MRT. All current clinically used MR compatible RF hyperthermia devices use the MR scanners body coil for imaging since commercial coils close to the body cannot be used in conjunction with these devices due to space and coupling constraints. To solve this issue, in Chapter 8 we conducted a proof of concept study to integrate an MR receive coil array into the hyperthermia array by using geometric decoupling.

1.5 Outline of this thesis

Chapter 2 (Part 1) provides the state of the art in MR guided RF hyperthermia devices, identifies the common characteristics of devices and provide the groundwork for improved device validation.

Chapter 3 (Part 1) describes a new MR compatibility assessment procedure and clinical benchmark for MR guided RF hyperthermia devices.

Chapter 4 (Part 2) demonstrates the effect of large vessels in head and neck region on hyperthermia treatment planning and gives insight on why MR guided hyperthermia is needed.

Chapter 5 (Part 2) introduces a new antenna concept, and describes the simulation guided design of the MRcollar.

Chapter 6 (Part 2) experimentally validates the MRcollar design and MRI compatibility.

Chapter 7 (Part 3) explores the potential of adjusting water bolus filling properties to improve MR thermometry.

Chapter 8 (Part 3) reports the investigations done towards the integration of the coils in the MRcollar.

Chapter 9 provides the general conclusions and future perspectives to finalize the scientific content of the thesis.

Part I:

Status quo and standardization

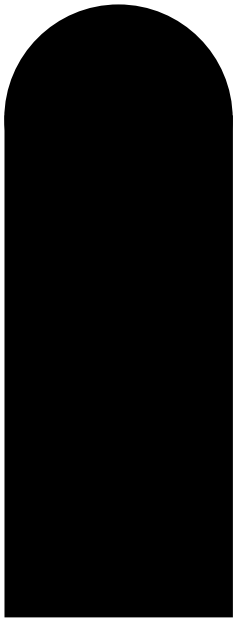

CHAPTER 2

State of the art in MR - RF hyperthermia

This chapter is based on:
F Adibzadeh*, **K Sumser***, S Curto, DT Yeo, AA Shishegar, MM Paulides. Systematic review of pre-clinical and clinical devices for magnetic resonance-guided radiofrequency hyperthermia. *International Journal of Hyperthermia*. 2020 Jan 1;37(1):15-27. *Joint first author.

Abstract

Clinical trials have demonstrated the therapeutic benefits of adding radio-frequency (RF) hyperthermia (HT) as an adjuvant to radio- and chemotherapy. However, maximum utilization of these benefits is hampered by the current inability to maintain the temperature within the desired range. RF HT treatment quality is usually monitored by invasive temperature sensors, which provide limited data sampling and are prone to infection risks. Magnetic resonance (MR) temperature imaging has been developed to overcome these hurdles by allowing non-invasive 3D temperature monitoring in the target and normal tissues. To exploit this feature, several approaches for inserting the RF heating devices into the MR scanner have been proposed over the years. In this review, we summarize the status quo in MR-guided RF HT devices and analyze trends in these hybrid hardware configurations. In addition, we discuss the various approaches, extract best practices and identify gaps regarding the experimental validation procedures for MR - RF HT, aimed at converging to a common standard in this process.

2.1 Introduction

Hyperthermia (HT) treatments involve heating tissues to the range of 40-44 °C for 60-90 minutes[62]. The majority of the HT treatments are applied using external devices employing radiofrequency (RF) electromagnetic waves[63,64]. Clinical trials have shown that RF HT improves clinical outcome, without adding to the toxicity, of radiotherapy and a number of chemotherapies[65–67]. Clinical work showed that intra-tumoral temperatures are correlated with clinical outcome parameters such as local control of tumors[13,33,68–74]. Due to the bodys strong, inhomogeneous and variable thermoregulation[23,24,75,76], close monitoring of the temperature is required to optimize the power distribution accordingly. Here, the goal is to focus energy at the target region and prevent unwanted hotspots in normal tissues. Several different approaches for non-invasive thermometry, like impedance tomography, active and passive microwave imaging, CT, laser, infrared, ultrasound, MR-techniques, have been investigated in the last decades. Among all these different techniques, MR thermometry (MRT) has been elaborated most extensively and validated in clinical and experimental settings[77,78]. In addition, the gantry of the current MRI systems provides the possibility for mechanical integration with hyperthermia applicators[58]. MR imaging also provides the possibility to image the complete treatment setup, i.e. patient surrounded by the applicator, as well as monitoring perfusion/tissue cooling and the response to treatment. To enable all the aforementioned benefits of using MRI with RF hyperthermia devices, the compatibility of these devices with the MRI system (MR compatibility) is crucial, especially in terms of how they impact image quality. These properties are often not quantified and reported in a standardized way for interventional devices. An overview of such systems and an inventory of the required image quality metric is however currently lacking.

The important potential benefits of non-invasive thermometry can be highlighted best when compared to invasive thermometry, which is the current golden standard for intra-tumoral temperature assessment during RF HT therapy. In invasive thermometry, temperature probes are inserted into closed-tip catheters and placed in body cavities or pierced into tissue. Invasive thermometry can be done using commercially available types of thermocouples and thermistors suitable for use in clinical hyperthermia. Available thermistors are the Bowman thermistor probe[79] (BSD Medical Corp.) and the fiber-optic (FISO) thermistor probe (gallium arsenide (GaAs)[80] and fluorescence (fluoroptic)[81] probes). Thermocouples and the Bowman thermistor probes rely on detection of a voltage and fiber-optic probes rely on the temperature dependency of band gap and refraction index. The reported accuracy of the fiber-optic and bowman probes are better than ±0.1 °C and ±0.2 °C respectively, taken from datasheets by the manufacturer. Although accurate, such thermometry provides very limited spatial information, i.e., only along the line of the catheter. Specifically, for RF HT treatment where a large volume is heated, the probability that invasive thermometry detects all the hotspots of interest is low. This is due to the limited number of temperature probes, and clinical restrictions for placement of thermometry catheters. In addition, probe insertion may be painful and hazardous. Complications such as infection or neurological complaints and other discomfort were observed along with a low acceptance in patients

and physicians[57,82]. Therefore, MRT has the potential to replace the invasive thermometry in the clinic because of its non-invasive nature, high spatial resolution and 3-dimensional (3D) anatomical coverage per unit time.

The first decade after the advent of MRT was devoted to developments in techniques allowing temperature assessment during thermal therapies[83–87]. Several temperature-sensitive parameters were studied, like the proton-resonance frequency shift (PRFS), apparent diffusion coefficient (ADC), longitudinal relaxation time (T_1), transversal relaxation time (T_2), and equilibrium magnetization (M_0)[88–90]. Of these endogenous temperature indicators, techniques that leverage the PRFS effect observed in water-rich tissue have been studied more extensively[88,89,91]. This technique is based on the fact that the change in image phase in a pair of gradient echo images acquired at two different temperatures is linearly proportional to the temperature change. This arises from a proton resonance frequency that linearly decreases as temperature increases in the water molecule (-0.01 ppm/°C)[92]. The second decade saw the development of techniques that enabled more robust and reliable results, especially for in vivo applications[93–96]. However, the PRFS effect is small and thus is highly sensitive to magnetic field perturbations, which degrade MR thermometry accuracy. Such degradation is especially pronounced in long duration hyperthermia treatments (≈90 min). These magnetic field perturbations may be caused by a number of possible mechanisms that manifest themselves differently. For example, gradient-induced heating of passive shim elements may cause non-periodic temporal B_0 drift that vary smoothly in space across the imaging field-of-view, while patient respiratory/ cardiac motion may induce periodic B_0 perturbations in a local region, especially near interfaces of tissues that have different magnetic susceptibility values. Non-periodic and local B_0 perturbations may also arise from intestinal/ bowel movement. The removal of these temporal field perturbation effects is crucial for successful MRT for thermotherapy monitoring, and the different variants of B_0 perturbation may require different types of correction methods. The inherent signal-to-noise-ratio (SNR) of MR signals is another very important quantity that impacts the accuracy and robustness of MRT.

For MR guided radiofrequency hyperthermia (MRgRFHT), the RF body coil in the MRI scanner is typically used to receive MR signals for MRT since HT devices are not designed to allow the concurrent placement and use of commercial MR flexible coils. Hence, the SNR available is relatively low since the RF body coil is positioned much further from the region of interest (ROI) compared to a surface coil array that could have been placed in close proximity to the patient. Moreover, RF body coils in commercial MRI scanners can only receive MR signals in single (quadrature) channel mode and thus do not exploit parallel imaging for scan time reduction. To address this problem, new hardware designs are being researched to improve SNR and enable MR parallel imaging, while simplifying and reducing equipment footprint (physical space that a device occupies). This can increase the reliability of MR-temperature measurements and improve patient access to MRgRFHT in the clinic.

The purpose of this paper is to analyze all research work done in the space of MRgRFHT, and review the status in terms of device validation, preclinical investigations and clinical trials. In this analysis, we excluded papers on devices aimed at thermal ablation and those focused

on MR thermometry techniques and algorithms. The current review attempts to review the scope of technical advances in MRI guided RF HT for new scientists, clinicians and other professionals and provide the groundwork for improved validation by summarizing and proposing standards on its reporting.

2.2 Materials and Methods

We performed a literature search in the Scopus and the Web of Science (WoS) databases using the following search strings:

TITLE-ABS-KEY [((("magnetic resonance" OR mr) AND thermometry) OR "thermal magnetic resonance" OR "thermal mr" OR temperature imaging) AND "hyperthermia"

OR

TITLE-ABS-KEY (hyperthermia AND mri) AND (clinical OR preclinical) AND (evaluation OR validation OR verification)]

AND

TITLE-ABS-KEY (hybrid OR integrated OR hardware OR configuration OR setup OR set-up OR system OR device OR applicator OR prototype OR platform)

where TITLE-ABS-KEY indicate either the title, abstract or keywords of the paper. This resulted in 325 articles (249 in Scopus and 76 WoS). The duplicated results in the two databases were removed. We further added 4 articles that were not found in the structured literature search and 2 conference abstracts that were not available in the Scopus or WoS databases.

Two exclusion steps were then introduced for selecting only papers concerning RF-HT (exclusion criterion 1) and original papers (exclusion criterion 2). The selection process is summarized in Figure 2.1.

In exclusion criterion 1, all papers were excluded having TITLE-ABS-KEY on the following:

Ablation

Non-RF HT, e.g. HIFU/Laser studies

Methodology, algorithm (e.g. theory of temperature monitoring and resolution, evaluation of temporal spatial resolution, estimation and correction of induced errors due to breath or organ displacement (motion)).

Application of exclusion criterion 1 reduced the number of papers to 106 articles (85 Scopus 19 WoS and 2 conference abs) after reading title-abstract and to 57 articles (46 Scopus, 9 WoS and 2 conference abstracts) after reading the full text. This selection comprised the relevant papers on MR guided RF-only HT devices.

Exclusion criterion 2 intended to only include original studies which presented novel design and prototypes. Articles including the following were excluded:

Review articles

Non-English language articles

Book series or only insufficient abstracts available

After exclusion criterion 2, 46 papers (39 Scopus, 5 WoS and 2 conference abstracts) remained presenting or investigating novel hybrid MRgRFHT devices. These devices are categorized in the next section and summarized in Table 2.1. In this work, we defined quantitative validation as the agreement between the measured quantities in MRT versus a gold standard technique, e.g., average error between MRT and invasive probe measurements. Those papers reporting only the quality of the agreement as an impression or distribution, i.e., quantifying only the shape and size of the heated zones in the MR images, were scored as qualitative.

2.3 MR-guided RF HT devices

Various approaches aiming to integrate RF-HT applicators and MRI system have been proposed and can be roughly categorized into: 1) decoupled systems (HT-only inserts) 2) integrated systems (Dual-function inserts).

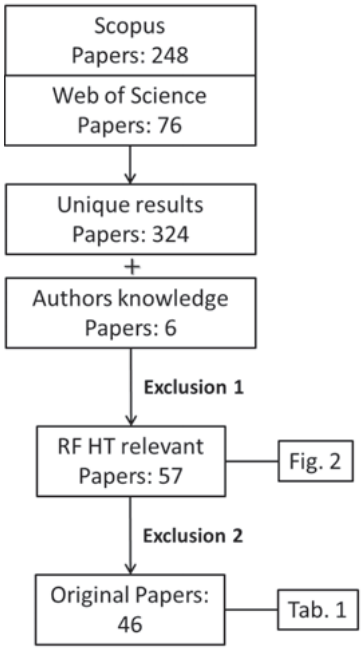

Figure 2.1: Selection process for inclusion of papers with criteria reported in the text.

2.3.1 Decoupled devices (HT-only inserts)

These devices are based on an independent RF transmission chain and an RF-HT applicator insert that operates inside the bore of a MRI scanner. Since such hyperthermia devices operate independently from the MR system, heating and imaging can be performed simultaneously. Unless mentioned otherwise, the MRI scanners RF body coil is used for both RF transmit and receive of the MR signals. Such developed devices are:

Non-invasive clinical setups

- BSD2000-3D-MRI applicator is the only MR-guided RF HT device that has led to a commercial prototype, in combination with 1.5 T MRI systems. This applicator consists of 12 dipole antenna pairs operating at 100 MHz, arranged on three rings of four dipole pairs each, that are independently controlled to steer the energy focus towards deep seated tumor volumes. This device has been validated both preclinically[95,97–99] and clinically[100,101]. A systematic comparison of 3D specific absorption rate (SAR) distribution between MRT and planning calculations in a homogenous cylindrical and heterogeneous elliptical phantom demonstrated a deviation in the range of 23 W/kg, i.e., below 10%[98]. The possibility to adapt/optimize SAR pattern in a phantom by employing MR thermometry in an iterative procedure were also shown for this applicator[102]. A recent more systematic quality assurance analysis of this system in a 1.5 T MRI scanner showed a mean maximum temperature increase (Tincrease, max) in a Perfax homogeneous phantom of 5.9 ± 0.4 °C, using 1000 W input power for 12.4 min, and a mean steering error of 0.4 ± 0.2 cm[99]. Clinical experiments in 15 patients[101] with pre-irradiated rectal recurrences showed significant correlation between the MRT-derived mean temperatures in the tumor with invasive measurements, tumor features (volume and location) and clinical response ($p = 0.04$)[101].

- The mini-annular-phased array (MAPA) RF HT applicator is the only other applicator which has been used on patients. The MAPA consists of four pairs of flared dipole antennas and was designed to treat limb tumors in extremities and modified for insertion into MRI scanner[103]. Usually a single frequency (140 MHz) and signals of equal amplitude and phase have been used. Hybrid operation was validated by inserting the MAPA into a 0.5 T whole body MRI system and its head coil during synchronous heating and imaging[87,103,104]. In these studies, diffusion coefficient based temperature imaging methods were used to monitor temperatures in a gel based phantom. Temperatures in 1 cm^2 regions of interest were found to be within 0.2 °C from invasive measurements. Clinical validation was performed in 4 patients with high-grade primary sarcoma tumors of the lower leg[105] and 10 patients with high grade extremity soft tissue sarcomas[106]. On the tumor ROIs, the mean difference between PRFS-MRT and interstitial point measurements was 0.62 °C in steady state.

- The MRlabCollar, is an MR-compatible laboratory prototype of the HYPERcollar3D HT applicator consisting of two rings of six patch antennas operating at 434 MHz. Pilot measurements by Numan et al. 2013 using the lower half of the original LabCollar showed an average PRFS-MRT accuracy of 0.4 °C (0.1 - 0.7 °C) against fiber-optic probe thermometry.[107].

Heating size and shape had a good correlation with predictions ($R^2 = 0.76$). Paulides et al. 2014 introduced the design of an MR compatible head and neck laboratory prototype applicator and showed the focused heating capabilities of MRlabcollar[61]: a maximum SAR of 100 W/kg and a temperature increase of 4.5 °C in 6 min was feasible using 300 W input power in a cylindrical fat/muscle phantom. The central heated region in this phantom corresponded very well to those obtained earlier by infrared measurements in a muscle-only split-phantom phantom for the setup without MR compatibility feature (LabCollar)[108]. This device was again validated pre-clinically in an oilgel phantom by applying a combination of MR imaging and 3D spline fitting for accurate probe localization[109]. The result corresponds to a reduced average error of $\Delta T < 0.14$ °C with a maximum error of $\Delta T = 0.22$ °C.

- The MRCollar, the clinical implementation of the MRlabcollar, consists of twelve dielectric parabolic reflector antenna (DIPRA) modules, i.e. parabolic water-filled encasings around printed reflector-backed dipole antennas[110]. Two arrays of six antenna structures were placed in two semi-circular structures. By electromagnetic simulations, the authors showed that the power focusing ability of the device in terms of the target coverage of the 25% iso-SAR contour (TC25) is 83.7 ± 15.6% for head and neck tumors in clinic. A reduced scale phantom experiment demonstrated that only very localized image distortion was observed. MR imaging was obtained using the body coil of 1.5 T MRI scanner.

- Capacitive: a two-channel capacitive RF heating system, consisting of four electrodes operating at 26 MHz, was evaluated on a phantom aiming to heat a deep-seated target region in which electrical conductivity was elevated by nanoparticle mediation[111,112]. When one electrode pair was activated, the other electrode pair was electrically isolated to prevent RF current leakage between the electrodes. MRT, using a 3 T MRI sequentially with the RF heating, showed maximum ΔT_{ave}<0.5 °C relative to fiber-optic measurements after phase error correction in the center of the phantom. Using this system, Hernandez et al. 2016 proposed a correction method of B_0 drift effects in MR thermometry[113], for which they placed magnetic field monitoring (MFM) probes around the subject to compute phase correction maps for MRT by interpolating the center frequencies of MFM signals on the imaging slice. Using phantom measurements, the authors showed that this B_0 drift correction reduced the mean squared temperature error of MR thermometry to an average of 0.47 °C. This device is the only capacitive MR guided RF HT device and the only system that used MFM probes instead of fat references for B_0 field drift corrections.

- The current sheet antennas (CSA) is a phased array consisting of two identical MR-compatible current sheet antennas operating at 100 MHz. Hoffmann et al. 2002 used CSA for heating a tissue-equivalent phantom inside a 3 T MRI[114]. The heating capabilities were measured with PRFS method in sequential heating and imaging experiments. The maximum error between the MR-derived and fiber-optic measured temperatures was estimated to be ±1 °C and the SD was 0.4 °C. This development has not translated into a clinical product.

- The clinical WACOA applicator (CWA) is a HT applicator consisting of twelve separate WAter COated Antenna (WACOA) modules operating within a 1.5 T MRI scanner. The modules are designed as MR-compatible, specially shaped and adjustable, cylindrical dipole struc-

tures embedded into hermetically closed cassettes filled with deionized water. Experimental and numerical evaluations demonstrated that the CWA is able to steer the 3D temperature pattern[115]. In 2005, the device was evaluated by a 3D comparison of predicted and measured temperature data sets for an inhomogeneous phantom[116]. The average error of the calculated versus measured temperature comparison was 0.45 °C. CWA was the first device which had its numerical model validated with 3D MR-temperature measurements, but it was not translated into a clinical version.

- The hexagonal flared-type whole body phased array applicator operates at 130 MHz and consists of 3 pairs of flared dipole antennas. The root mean square (RMS) and average difference between the MR-derived temperatures (1.5 T) and probe temperatures in phantom were 1.23 °C and 0.92 °C, respectively[117]. The standard error of the mean temperature change was found to be 0.22 °C in a 50 mm^3 region of a gel phantom for echo time of 20 ms[118]. The group also performed in vivo experiments to evaluate the ability of MRT in canine brain and muscle[118–120]. The results showed a standard error of 0.6 °C in a 16 mm^3 volume for brain tissue and muscle tumor (sarcoma)[118].

Invasive clinical setups

- The intravascular MRI guidewire is an interstitial system that simultaneously produces RF heating and high SNR imaging/temperature mapping used for enhancement of vascular gene transfer. The system consists of MRI guidewire placed within the guidewire channel of a gene delivery catheter and is connected to an 1.5 T MR scanner and external RF generator/amplifier through a filter box[121]. The system was validated both in vitro (cylindrical phantom, qualitative validation) and in vivo (in the aorta of rabbits), For the in vivo experiment, the SD error between the MR-derived temporal curve and that of the fiber-optic measured temperature curve was 1.2 °C. Moreover, the maximum temperature increase in target aortic wall was approximately 7 °C from a baseline temperature of 37 °C using 45 W input power for about 4 min. The intravascular MRI guidewire was the first device that used the same antenna for RF heating and MR imaging in a simultaneous operation.

Preclinical (animal) setups

Preclinical setups are small and flexible in comparison to conventional HT systems and generally combined with ultrahigh field preclinical MRI systems. The antennas predominantly operate at 2.45 GHz.

- The Slot&Dipole applicator by Demura et al. in 2006 are two MR-compatible microwave applicators operating at 2.45 GHz of dipole-type and slot-type and evaluated using phantoms and living animals[103]. A 10-mm-deep area could be heated at an average target temperature of 42.60 ± 0.14 °C and a skin surface temperature of 43.27 ± 0.45 °C, using 60 110 W input power intermittently (2 s power-on, 2 s power-off) for 60 min experimental period. The 95% limits of agreement between MR and fluoroptic thermometry in the three rabbits were +0.318/-0.339 °C, +0.693/ -0.661 °C, and +0.564/-0.526 °C, respectively.

- The coaxial applicator incorporates a 3.5 mm directional microwave antenna operating at 2.45 GHz designed for small animal investigations inside the 30mm bore of the 14 T ultrahigh field MRI scanner[122]. Simulations and experiments in tissue mimicking phantoms demonstrated the feasibility of heating 21 982 mm^3 targets to temperature rises of $T_{increase}$ >3 °C at radial distances up to ≈6 mm from the applicator, with 8 - 12 W input power. ΔT_{max} between MR thermometry and fiber-optic temperatures was ≤0.6 °C. In vivo experiments demonstrated the feasibility of delivering HT to implanted tumors in two experimental mice in combination with PRFS based MRT[122]. ≈4 °C and ≈11 °C temperature increase were achieved with 20 W microwave exposure for 5 min and 15 min, respectively.

- The Yagi-Uda-based small animal HT applicator operating at 2.45 GHz was designed and validated by Raaijmakers et al. in 2018 for superficial HT in small animals in a 7 T MR scanner[123]. The antenna was based on an earlier designed MR-compatible YagiUda antenna presented by Paulides et al. 2017[124]. The antenna was designed for a low MR-footprint and directional radiation properties to minimize inter-element coupling for typical array configurations (S_{21} < -23 dB). Validation in a homogenous muscle phantom showed PRFS-MRT to correlate with temperature probe measurements (root mean square error: RMSE = 0.51 °C and $R^2 = 0.99$) and the ability to create a small heating focus (<1 cm^3) in an animal-sized muscle-mimicking phantom. The applicator was mechanically redesigned by reducing the distance between antenna arms and the target[125] to reduce losses in the deionized water (severe at 2.45 GHz) between antenna and animal. In vivo experiments in leg tumors of four nude mice showed a ΔT of 7 °C in 5 minutes using 7 W power and no artefacts were observed in the MR images during simultaneous heating and imaging.

- The Annular-phased Array (APA) is composed of six dipole antennas for heating deep seated regions of the body. Kowalski et al. 2002 proposed a phase/amplitude optimization technique using only information from MRT[126]. Preclinical validation of the device, operating at 915 MHz, was performed by heating a homogeneous cylindrical phantom[126,127]. The applicator and phantom were placed inside an MRI birdcage coil, and the entire assembly was inserted into a 4.7 T MRI magnet. Fluoroptic probe measurements demonstrated control of the heat focus position employing only MRT-based temperature feedback information. The APA is the only applicator where the ultimate goal of MRgRFHT, i.e. control of the temperature distribution based on MRT, was realized during a phantom heating experiment.

2.3.2 Dual-function devices

These devices use the same antenna array for heating and imaging. When the MRI RF body coil is used for imaging, problems such as inter-system cross-talk, signal oscillations and low image SNR arises. Dual-function devices overcome these limitations since they only have a single system, they have multichannel antenna operation and the antennas are closer to the target for higher signal pickup. However, since these devices require interleaved operation, simultaneous operation cannot occur.

Electronic switching

These devices consist of a single set of conductive structures that can alternately be used for MRI receive and RF heating using fast electronic switches. The two possible implementations use either the scanners RF transmit chain for heating at the Larmor frequency or a separate transmit chain to apply RF energy at a different frequency. Inter-system coupling and RF HT equipment footprint is theoretically smaller in such devices compared to decoupled two-system configurations. Yeo, et al., 2011 introduced one such device operating at 128 MHz (Larmor frequency at 3 T), which switches between a loop coil array for MR imaging and a C-shaped dipole antenna array that generates focused electric fields for RF heating via selective inclusion/ exclusion of impedance matching and tuning capacitors using fast RF switches[128]. The results indicated that C-shaped dipole antenna arrays can induce steerable heating similar to straight dipole antenna arrays. The loop coil array functions as a 3 T MRI RF receiver that yields an imaging SNR that is about three times higher than that of an RF body coil. Therefore, C-shaped dipole antenna arrays could potentially enable 3D heat steering and MRI with the same physical hardware.

Thermal MR

Another approach, designated as thermal MR, allows RF heating and MR imaging application using the same antenna array and the power amplifier of the MR system. Here, part of the regular imaging sequence time, e.g., the last 10%, is used to apply RF for heating. This approach is particularly effective in MR scanners at ultra-high magnetic fields ($\geq$ 7 T) for which the Larmor frequency approaches the optimum frequency for semi-deep heating[129,130]. The advantage of the pulse modulated signal used for RF HT and MRT is the ability to modify the imaging technique in order to perform RF HT and MRI at the same frequency without the need for electronic switching which further reduces the dead time for contemporaneous operation. In addition, the electric fields for imaging and heating are equal, thus in vivo quality assurance can be applied using $B_1{}^+$ imaging as a surrogate for the electric field induced in the patient. One such device is an 8-channel transmit/receive (Tx/Rx) hybrid RF applicator consisting of bow-tie dipole antennas (dual function bowtie array) that generate an E-field pattern for RF heating and a circular polarized H-field for MRI[129]. Each channel has independent control of phase and amplitudes. The applicator was connected to the MR system via a coil interface comprising 8 Tx/Rx switches.

In 2015, Winter et al. presented the preclinical results derived from the same applicator at 300 MHz using a cylindrical phantom mimicking brain tissue with the size of a human head[130]. The experiments demonstrated that the pulsed multi-channel transmit system of a 7 T MR scanner supports targeted RF heating and provides enough power ($P_{avg} > 400$ W) to induce a temperature increase of $\approx$11 °C in 3 min in the center of a head sized phantom.

Table 2.1: Table summarizing original studies on MR-guided RF HT devices. Note that in view of clarity, for each parameter, only the best achieved data is summarized in this table. Unless stated, all reported accuracies were measured vs. fiber-optic temperature probe. R^2: correlation coefficient, ΔT_{ave}: average temperature error, ΔT_{SD}: standard deviation of temperature error, ΔT_{max}: maximum temperature error, Treso: thermal resolution, SAR: specific absorption rate, SNR: signal to noise ratio.

Device	MRI insert configuration (HT-only/ dual-function)	Intended application (Preclinical/ clinical) and body site	MRI System Information	Validation status Not validated vs. validated (preclinical/ clinical)	Heating validation metric (Qualitative/ Quantitative)	MR compatibility validation metric (Qualitative/ Quantitative	MRT sequence parameters used for quantitative validation	MRT accuracy validation metric (Qualitative/ Quantitative)
BSD2000-3D-MRI: 12 dipole pairs (100MHZ) [95,97–101,101]	HT-only	Clinical Lower extremities and the pelvis	1.5 T Body Coil RX/TX chain Simultaneous heating and imaging	Preclinical: cylindrical and elliptical phantoms	Quant.: $Mean - T_{incr,max} = 5.9 \pm 0.4°C$, Mean-steering error $= 0.4 \pm 0.2$ cm [99]	Not reported	SPGR sequence TR: 600 ms TE: 20 ms FA:50 Reso:not reported [97] SPGR sequence TR: 600 ms TE: 5, 20 ms FA:50 Reso: 3.9x3.9x10 mm^3 [95] SPGR sequence TR: 750 ms TE: 4, 20 ms FA:50 Reso: 3.9x3.9x10 mm^3 [98]	Quant.: ΔTave = ±0.4°C [97] T_{reso} =±0.51°C [95] ΔSAR_{ave} <10% [98]
				Clinical: 24 patients: 15x rectum/bladder [101] 9x high grade sarcoma - lower extremities/pelvis [100]	Qual.: $T_{ave,MR}$ of the tumor is a useful variable to evaluate the quality and effectivity of treatments [101] Not reported	Qual.: MRgHT is feasible. [100,101]	SPGR sequence TR: 600 ms TE: 20 ms FA:50 Reso: 3.9x3.9x10 mm^3 [100]	Quant.: P = 0.04: $MRT_{ave,tumor}$ vs. clinical response [100] $R^2 = 0.96$: MRT vs. conventional invasive thermometry* [101]
MAPA: 4 flared pairs (140MHz) [103–105]	HT-only	Clinical Extermities	1.5 T Head Coil RX - Body Coil RX/TX chain Simultaneous heating and imaging	Preclinical: cylindrical phantom [103]	Not reported	Qual: No artefacts were observed	GRE sequence TR: 34 ms TE: 20 ms FA:50 Reso: 0.9x0.9x10 mm^3 [104,105]	Quant: $\Delta T_{ave} < 0.2°C$, $R^2 = 0.998$ [104]

Continued on next page

Table 2.1 – continued from previous page

Device	MRI insert configuration (HT-only/ dual-function)	Intended application (Preclinical/ clinical) and body site	MRI System Information	Validation status Not validated vs. validated (preclinical/ clinical)	Heating validation metric (Qualitative/ Quantitative)	MR compatibility validation metric (Qualitative/ Quantitative	MRT sequence parameters used for quantitative validation	MRT accuracy validation metric (Qualitative/ Quantitative)
				Clinical: 14 patients (leg sarcomas) 4 patients [104] 10 patients [105]	Not reported	Quant: $SNR_{tumor} = 115$, $SNR_{muscle} = 90$ [105]	SPGR sequence TR: 600 ms TE: 20 ms FA:50 Reso: 3.9x3.9x10 mm^3 [100]	Quant.: $R^2 = 0.84$ $\Delta T_{ave,tumor}$ < 0.62°C
MRlabCollar (434 MHz) [61,107,109]	HT-only	Preclinical H&N	1.5 T Body Coil RX/TX chain Sequential heating and imaging	Preclinical: cylindrical phantom	Quant.: $T_{increase,max}$ $= 4.5$°C [61] $R^2 = 0.76$: Thermal distribution size and shape in MRT vs. simulations [107] Qual: capability of the focused heating was confirmed [61]	Qual: No severe distortions in ROI in the MRT image [61]	SPGR sequence TR: 34 ms TEs: 14.9, 17.3, 19.7 ms FA:29 Reso: 1.6x1.6x10 mm^3 [109]	Quant: ΔT_{ave} <0.14 °C, ΔT_{max} $= 0.22$ °C [109]
MRCollar: (434 MHz) [110]	HT-only	Clinical H&N	1.5 T Not reported	Preclinical: reduced scale setup (continuation of MRlabcollar)	Not reported	Qual: No large artifacts for the modules containing the antennas	Not reported	Not reported
RF capacitive (26 MHz) [111,112]	HT-only	Clinical Brain (nanoparticle)	3 T Body Coil RX/TX chain Sequential heating and imaging	Preclinical: cylindrical phantom	Not reported	Not reported	GRE sequence TR: 110 ms TE: 10 ms FA:60 Reso: 1.6x1.6 mm^2 slice thickness not reported [111,112]	Quant: ΔT_{ave} < 0.5°C [111,112]
APA (915 MHz) [126]	HT-only	Clinical deep seated tumor	4.7 T Body Coil RX/TX chain Simultaneous heating and imaging	Preclinical: cylindrical phantom	Qual: ability to control of the position of the focal point [126]	Not reported	Not reported	Not reported
CSA (100 MHz) [114]	HT-only	Clinical deep-seated pelvic and abdominal	3 T Body Coil RX/TX chain Sequential heating and imaging	Preclinical: cuboid phantom	Not reported	Not reported	GRASS sequence TR: 160 ms TE: 20 ms FA:40 Reso: 2x2x10 mm^3 [114]	Quant: $\Delta T_{ave} = \pm 1$°C, $\Delta T_{SD} = 0.4$°C [114]

Continued on next page

Table 2.1 – continued from previous page

Device	MRI insert configuration (HT-only/ dual-function)	Intended application (Preclinical/ clinical) and body site	MRI System Information	Validation status Not validated vs. validated (preclinical/ clinical)	Heating validation metric (Qualitative/ Quantitative)	MR compatibility validation metric (Qualitative/ Quantitative	MRT sequence parameters used for quantitative validation	MRT accuracy validation metric (Qualitative/ Quantitative)
CWA (100 MHz) [115,116]	HT-only	Clinical pelvis and abdomen	1.5 T Body Coil RX/TX chain Simultaneous heating and imaging	Preclinical: cylindrical phantom	Qual.: good ability of field pattern steering [115,116]	Qual.: MR-compatibility has been verified in preliminary tests [115]	SPGR sequence TR: 600 ms TE: 20 ms FA:50 Reso: 3.9x3.9x10 mm^3 [116]	Quant.: ΔT_{ave} =0.45°C [116]
Intravascular MRI guidewire (180 MHz) [121]	HT-only	Clinical vessel wall	1.5 T Body Coil TX chain/ Intravascular MRI guidewire RX Simultaneous heating and imaging	Preclinical: cylindrical phantom Aorta of rabbits	Not reported Not reported	Qual.: The SNR profile was comparable to the pattern of simulated RF power distribution Quant.: T_{incr}, max ≈7°C	SPGR sequence TR: 68 ms TE: 15 ms FA:30 Reso: 0.9x0.9x8 mm^3	Qual.: The simulated RF power distribution was comparable to that of MRT Quant.: ΔT_{SD}= 1.2°C
Slot & Dipole-type (2.45 GHz) [103]	HT-only	Preclinical Animal thigh muscle	7 T Body Coil RX/TX chain Sequential heating and imaging	Preclinical cuboid phantom 10 male rabbits: thigh muscle In 6 rabbits: VX2 tumor cells were inserted	Not reported Not Reported Quant.: $T_{incr_{ave_{tumor}}}$ = 42.60 ±0.14°C $T_{incr_{ave_{skin}}}$ = 43.27 ± 0.45°C	Not reported	SPGR sequence TR: 20 ms TE: 8 ms FA:20 Reso: 1.2x1.2x3 mm^3 SPGR sequence TR: 20 ms TE: 8 ms FA:20 Reso: 0.8x0.8x3 mm^3	Quant.: ΔT_{2SD} = +0.318/-0.339°C Quant.: ΔT_{SD} = +0.693/-0.661°C ΔT_{2SD} = +0.564/-0.526°C
Coaxial-type (2.45 GHz) [122]	HT-only	Preclinical local tumors in small animals	7 T Body Coil RX/TX chain Simultaneous heating and imaging	Preclinical: cylindrical phantom 2 experimental mice with implanted tumors	Quant.: $T_{incr} \geq 3$°C Not reported	Not reported	SPGR sequence TR: 40 ms TE: 4 ms FA:25 Reso: 2.3x2.3x1 mm^3	Quant. : ΔT_{max} ≤ ±0.6°C Qual.: Feasibility of in vivo MRgHT

Continued on next page

Table 2.1 – continued from previous page

Device	MRI insert configuration (HT-only/ dual-function)	Intended application (Preclinical/ clinical) and body site	MRI System Information	Validation status Not validated vs. validated (preclinical/ clinical)	Heating validation metric (Qualitative/ Quantitative)	MR compatibility validation metric (Qualitative/ Quantitative	MRT sequence parameters used for quantitative validation	MRT accuracy validation metric (Qualitative/ Quantitative)
Hexagonal flared-type (130 MHz) [117–120]	HT-only	Preclinical whole body	1.5 T Body Coil RX/TX chain Simultaneous heating and imaging	Preclinical: cylindrical phantom 2 canines: brain and muscle	Not reported Not reported	Qual.: Simultaneous heating and imaging without deterioration of SNR [117] Not reported	GRE sequence TR: 34 ms TE: 20 ms FA:25 Reso: 0.6x0.6x4 mm^3	Quant.: $\Delta T_{ave} = 0.92°C$, $T_{RMS} = 1.23°C$ [117] $T_{reso} = 0.22°C$ [118] $T_{reso} = 0.22°C$ [118]
Yagi-Uda-based (2.45 GHz) [123,125]	HT-only	Preclinical whole body	7 T Body Coil RX/TX chain Simultaneous heating and imaging	Preclinical: cylindrical phantom 4 mice: tumor on leg [125]	Qual.: ability to create a small heating focus ($< 1mm^3$). Satisfactory agreement between simulated vs. MRT distribution. Quant.: T_{incr} =7°C	Qual.: The applicator is MR-compatible. No disturbances are visible in the area of interest. Qual.: No artefact in MR images	Not reported	Not reported
Electronic switching: Coil/C-shaped dipole (Larmor freq.) [128]	Dual-function	Preclinical not mentioned	3 T Integrated RX/TX chain Sequential heating and imaging	Preclinical: cylindrical phantom	Qual.: Ability for steerable heating. Repeatable heating patterns in subsequent experiments.	Not reported	SPGR sequence TR: 100 ms TE: 12 ms FA:35 Reso: 3.75x3.75x10 mm^3	Quant.: $T_{incr,max}$ ≈4.3°C in 45 mins
Thermal MR: Bow-tie dipoles (Larmor freq.) [129,130]	Dual-function	Preclinical not mentioned	7 T Integrated RX/TX chain Sequential heating and imaging	Preclinical: cylindrical phantom	Qual.: ability to generate and steer deep-seated temperature focus [129] Quant.: T_{incr} ≈11 °C: center of a head sized phantom. [130]	Not reported	Not reported	Not reported
Statistics of preclinical devices	5x HT only 2x Dual-function	7x Preclinical devices		12x Preclinical validations	5x Quant 2x only Qual 5x Not reported	0x Quant 4x only Qual 8x Not reported	5x SPGR 2x GRE	5x SPGR 2x GRE
Statistics of clinical devices	8x HT only	8x Clinical devices		9x Preclinical validations	2x Quant 2x only Qual 5x Not reported	0x Quant 5x only Qua 14x Not reported	6x SPGR 2x GRE 1x GRASS	6x Quant 1x only Qual 2x Not reported

2.4 Discussion

The purpose of this comprehensive review article is to inform scientists, clinicians, engineers and hardware professionals of the state-of-the-art in MRgRFHT devices to potentially accelerate technical and clinical investigations in this space. Our literature search shows that an increasing number of groups are investigating approaches to apply HT under MR guidance (Figure 2.2). Although most of the devices developed (Table 2.1) have not been evaluated in the clinic, multiple in vivo experiments demonstrated the maturity of MRT for clinical applications. Especially for the BSD and MAPA applicators, the results of clinical validations show a high correlation between MR-derived temperature and invasive probe measurements. However, these results were obtained in anatomical regions where MR signals were minimally affected by motion, i.e., distal from tissues impacted by moving air in intestines, cardiac, bowel, and respiratory motion. Hence, improved motion robust MR thermometry approaches for HT are still highly warranted.

In our list, 10 devices were intended for clinical use. However, only two of them were actively used in the clinic (BSD2000-3D-MRI, MAPA), and only the BSD2000-3D-MRI is commercially available. Both of these applicators operate in a 1.5 T MRI system. This is convenient since 1.5 T systems are cheaper and more available than the 3 T systems. Furthermore, it is easier to filter the high-power RF hyperthermia signals (100 MHz or 140 MHz) from the 1.5 T RF transmit/ receive signals (64 MHz) compared to the 3 T RF signals (128 MHz) during simultaneous RF hyperthermia treatment and MR imaging. Dual function devices by design do not have to tackle this issue. Higher field strengths are also preferable because the Larmor frequency approaches the optimum heating frequency, which is between 150-300 MHz in the pelvic region and between 300-915 MHz for head and neck and extremities[131]. After the early feasibility studies of diffusion-based MR thermometry methods, PRFS-based MRT methods were used in all studies. Spoiled gradient echo sequence with echo times close to the T_2* of muscle tissue is commonly used for PRFS-based MRT scans[99,104,114,116,118,132]. In addition to treatment monitoring, MRT also provides unique opportunities to validate EM models with 3D measurements. Validation by MRT was only utilized for the BSD, MRlab-collar, CWA and dual function bowtie array applicators.

The MR compatibility of complex assemblies like RF hyperthermia arrays coupled to water-bolus structures is often difficult to achieve. In addition, MR-compatible applicators are typically less efficient and controllable in comparison to the corresponding applicators outside MRI. Since MR compatibility requires the use of non-magnetic components, many off-the-shelf connectors, baluns (required to go from unbalanced coax to a balanced dipole) and matching network approaches cannot be used. The circulatory movement of water in the water bolus often generates MR image artifacts. Consequently, the efficiency and the capability to control the RF heating pattern might be compromised in MR-compatible applicator types. On the other hand, the availability of 2D/ 3D MRT temperature maps now provides a unique opportunity to improve and optimize the treatments. If MRT cannot be utilized to improve thermotherapies, MR-compatible applicator types will only be useful for accurate modeling of treatment setup.

2.4.1 Reporting of validation results

Comparing the performance of these devices is currently not straight-forward. This stems from the fact that, there is a lack of general metrics for quantitative and qualitative validation of MRgRFHT devices. In several cases, performance of devices were reported in vague terms such as reasonable correlations and relatively comparable. As the data in Table 2.1 shows, different investigations reported different goals and metrics for the validation. Out of 25 clinical and pre-clinical validation experiments for 15 reviewed devices, 12 contain reports on heating ability (7 quantitative and 5 qualitative validations), 12 on MR compatibility (1 quantitative and 11 qualitative validations) and 20 on MRT accuracy (18 quantitative and 2 qualitative validations).

In our view, validation of an MR-guided RF HT device can be broken down into three distinct topics: heat focusing and steering, MR compatibility, and MRT accuracy. Based on our review, we extracted and recommended metrics for standardization of the validation (Table 2.2).

First, an RF HT devices ability to apply heat in a targeted manner may be characterized by minimum hot spot size, steerability of hot spots, and spatial conformality of heated re-

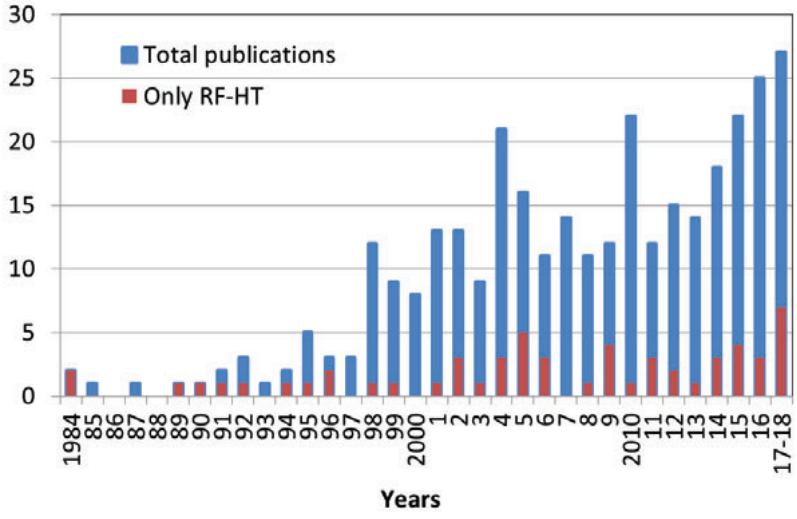

Figure 2.2: The number of publications over years after applying the search string and exclusion criterion 1 provided in the text (Material and methods). An increased number of publications on MR-guided RF HT (red bars) can be seen after 2001 (development of the BSD2000-3D-MRI) and after 2014 (development of the MRlabcollar and Thermal MRI).

Table 2.2: Summary of proposed validation stages and metrics for standardization of the validation of MRgHT devices.

Topic	Sub-topic	Quantification metric
Heating ability	Focusing	Option 1: Ttarget, increase Option 2: SARmax for 1 W input power Option 3: 50% iso-SAR
	Focus steering	Option 1: relocation of maximum heating point (mm) Option 2: relocation of centre of the 50% iso-SAR contour (mm)
Compatibility	B_0	No standardized metrics were found in literature Proposal: average and maximum ΔB_0 changes with/without the RF HT device present
	$B_1{}^+$	No standardized metrics were found in literature. Proposal: average and maximum $\Delta B_1{}^+$ changes with/without the RF HT device present
	Decoupling	No standardized metrics were found in literature. Proposal: Option 1: Coupling between the systems (S-matrix). Option 2: Image quality degradation metrics during contemporaneous operation of MRI and RF HT
	Image noise	Image signal to noise ratio (SNR)
	Geometric distortion	DICE score, normalized cross-correlation of landmarks in calibration phantoms
MRT accuracy	ΔT Accuracy	Root mean squared error (RMSE)
	ΔT Bias & precision	Mean error (ME) & Standard error (SE)
	Correlation	Coefficient of determination (R^2) and probability (p-value)

gions to some desired region. Metrics to describe these qualities may be defined in terms of temperature rise or SAR. Second, the devices interaction with the MR environment, i.e. MR Safety and MR compatibility, should be assessed. The test methods for MR safety have been identified by committees[133–136] but there is currently no set of tests for MR compatibility. We recommend that a devices effect on B_0 homogeneity, $B_1{}^+$ homogeneity, and SNR should be measured for MR compatibility assessment. To that end, image SNR[137–140] and geometric distortions[141,142] should be quantified. Furthermore, sufficient decoupling between MRI RF frequency and HT RF frequency (and its harmonics and parasitic frequencies) needs to be demonstrated. Lastly, the validation of MR thermometry should be quantified as the difference between the MR-derived versus invasive measured temperature increase for various probe sensor points based on National Institute of Standards and Technology (NIST). For experiments that involve the use of phantoms, the phantoms dimensions, shape, material, and probe locations should be reported. In the case of in vivo experiments, the number of subjects, region of interest, pathology type, and probe insertion locations should be reported, where applicable. For all MRI-based measurements, the MRI pulse sequence type, scan parameters (e.g., echo time, repetition time, flip angle, matrix size, slice thickness, field of view, total acquisition time, etc.) should be reported.

2.4.2 The further development of MRgRFHT

Future work will aim to improve thermotherapy delivery performance by enabling more accurate temperature monitoring with dedicated sequences and post processing techniques that mitigate artifacts, e.g., motion. Accurate temperature monitoring enables to adjust the SAR for better targeting the heat into the tumor area. New hardware solutions are urgently needed to simplify and reduce equipment profile to increase patient access to MR-guided RF HT in the clinic, e.g., low-profile liquid bolus for permittivity matching and cooling, and dual-function integrated MR-RF HT applicators for improved SNR in MR thermometry.

An excellent potential of using a single integrated antenna array structure for dual-function devices has been demonstrated in the literature. However, that approach is hampered by 1) the need for sequential heating and imaging, and 2) potentially contradicting requirements in terms of frequency and coil/antenna design. Decoupled devices have the benefit that different frequencies can be used for imaging and heating, which enables 1) simultaneous operation and 2) the possibility of exploiting optimal heating frequencies regardless of the imaging frequency. Another benefit of the latter approach is that it allows RF HT to be applied on the most commonly available MRI field strength in the clinic (1.5 T) today, which can potentially increase patients access to RF HT and lower operational costs. Hence, accessibility of electronic switching and thermal MR approaches are strongly dependent on the progress in the clinical availability of scanners based on 3 T, 7 T or beyond.

The ability to quickly reconfigure the setup of an MRI scanner from RF hyperthermia treatment to standard diagnostic imaging mode, and vice versa, is also important in a clinical setting. This is especially if the clinic aims to maximize patient throughput on the scanner,

regardless of whether it is used for therapy or diagnostic imaging. Thus, the RF hyperthermia equipment and associated software needs to be configured such that a quick change between diagnostic and interventional modes of an MRI scanner can be made. This may involve dedicated scanner tables and software for diagnostic versus therapy modes.

The current clinical application of MR guided RF hyperthermia is strongly hampered by motion, heterogeneities, clips, and physiological changes (bladder filling, perfusion, swelling). The major problem with the PRFS (used in most cases) is the strong disturbance by motion and heterogeneities. Other MR parameters (T_1 or T_2) might be better suitable since these are less sensitive to motion, and motion correction techniques like gating could be applied. Note that many of these techniques are studied in the context of thermal ablation[143–145], but application for the range of 40-44 °C still has to be studied. For all methods, increasing SNR is highly warranted since this allows for faster scanning and/or more accurate measurements. We foresee that clinical translation of the novel applicator approaches reported in this review will provide big steps toward achieving sufficient SNR as groundwork for accurate MRT in the clinic. This, in turn, will aid in the development of more precise heating devices and truly, i.e. MRT feedback controlled, application of MRgRFHT.

2.5 Conclusion

In conclusion, on-line non-invasive 3D MR thermometry (MRT) offers very valuable information about the tumor and normal tissues to improve treatment planning, treatment monitoring and assessment of treatment effectiveness. The results obtained thus far from the MR-guided RF HT devices described are very promising, and MRT during RF HT treatment has been demonstrated to be feasible in selected cases. Still, improvements are highly warranted to enable MRT guided treatment and treatment optimization in more anatomical locations with greater robustness to motion-induced artefacts. Technical advances during recent years may provide promising solutions to overcome many of the technical obstacles such as poor temperature measurement accuracy, low temporal resolution and low imaging SNR. Unfortunately, it is difficult to truly compare the advances since very little standardization was observed in the ongoing work on device validation. In this paper, we therefore list currently used metrics and propose new ones in case of gaps for experimental validation of such devices. We believe that homogeneous reporting of validation results will help selecting the best approach for all clinical scenarios. Hence, this paper will form a major drive for clinical implementation of new MR hyperthermia technologies and, hence, will reduce one roadblock for achieving spatially and biologically selective exploitation of the pallet of hyperthermia benefits.

CHAPTER 3

A new MR compatibility assessment procedure and clinical benchmark

This chapter is based on:
K Sumser, MM Paulides, GG Bellizzi, GC van Rhoon, JA Hernandez-Tamames, S Curto. Influence of the BSD-2000 3D/MR hyperthermia applicator on MR Image Quality: A Quantitative Assessment. *In 2020 14th European Conference on Antennas and Propagation (EuCAP)* 2020 Mar 15 (pp. 1-3). IEEE.

Abstract

MR compatible hyperthermia devices exploit MR thermometry capabilities for non-invasive treatment monitoring. These devices, which have been tested to be MR safe, can potentially influence the MR image quality. One such device is the Pyrexar BSD2000-3D-MRI applicator. In this study, we quantitatively evaluated the impact of the applicator for different setups on MR imaging by $B_1{}^+$ and signal-to-noise (SNR) measurements. Our results show 30% decrease in the $B_1{}^+$ transmit efficiency and 20% decrease in the SNR. We have found the biggest impact was caused by the devices water bolus. This effect can be overcome by increasing the B_1 transmit gain or using a thinner water bolus in the device design.

3.1 Introduction

During hyperthermia treatments, target volume temperature is increased to 40-44 °C to sensitize the tumor cells for chemo or radiotherapy[66]. MRI can provide valuable information on anatomy and temperature changes non-invasively. Hence, it has become a valuable tool for hyperthermia therapies. Several MRI guided hyperthermia devices have been developed to take advantage of the capabilities of MRI[95,103,107,116,128]. These devices operating within the MR environment are thoroughly tested and quantified for MR safety according to the safety guidelines[146]. Additionally, these devices can affect the imaging quality. While the effect on imaging does not affect the safety aspect, it can hamper the diagnostic/monitoring capabilities, therefore it also requires quantitative evaluation.

The Pyrexar BSD2000-3D-MRI (referred as Sigma Eye) is an MR compatible hyperthermia applicator which utilizes radio frequency radiation for selective heating of deep seated pelvic and extremity tumors. Compared to the non-MR compatible model, this applicator also utilizes MR thermometry in addition to the gold standard high resistance thermistor probes[79] or fiber optic temperature sensors[100]. Several studies have evaluated the electrical characteristics, heating performance and validated MRI compatibility qualitatively of the Sigma Eye[99,147]. However, no quantitative evaluation on the influence of the Sigma Eye on MR image quality has been published yet.

In this study, we quantitatively evaluated the impact of the Sigma Eye, its water bolus and its 100 MHz RF heating signal on MR imaging using an homogeneous cylindrical phantom. We have measured B_1^+ (flip angle (FA) maps) and Signal-to-Noise Ratio (SNR) measurements in four different setups and compared it to the baseline measurements, i.e., when only the phantom was in the scanner bore.

3.2 Material & Methods

3.2.1 Sigma Eye and Quality Assurance Phantom

The Sigma Eye (shown in Figure 3.1a) consists of 12 dipole antenna pairs which are arranged over three elliptically shaped rings. Phase and amplitude of each dipole pairs are independently controlled. To transfer the electromagnetic energy, a 100 MHz RF heating signal is used. A dedicated water bolus is placed between the patient and the applicator and it provides coupling between the antennas and the human body and also cools the patient skin during treatment. In Erasmus MC, the Sigma Eye operates in conjunction with the GE MR450w 1.5 T MR scanner. The scanner is equipped with bandpass filters at 100 MHz to filter out this signal during MRI imaging to enable simultaneous operation. To evaluate the influence of the Sigma Eye on MR image quality, we chose a homogeneous cylindrical phantom. This cylindrical phantom is filled with a mixture of demineralized water and premixed Perfax wallpaper paste (T_1: 2400 ms; T_2: 1000 ms).

3.2.2 Experimental Setup

The phantom has been imaged in four different setups:

1) phantom only (indicated as baseline scenario). The results of these measurement were used as a baseline.

2) applicator around the phantom in treatment position with empty water bolus (heating off). The results of these measurements were used to show the influence of the metallic parts of the Sigma Eye.

3) applicator around the phantom in treatment position with filled water bolus (heating off). The results of these measurements were used to show the influence of the water bolus.

4) setup 3 and applicator is turned on with 600 W input power (heating on). The results of these measurements were used to show the influence of the 100 MHz RF heating signal.

FA maps were acquired using Bloch-Siegert shift method[148]. SNR was evaluated on clinically used MR thermometry pulse sequence, i.e. double echo gradient echo. The sequence parameters used for imaging were as follows: TR/TE1/TE2 620/4.6/18.4 ms, slice thickness 10 mm, slice spacing 22 mm, 5 slices, FOV 500x500 mm^2, matrix size 256x256, NEX 1. Two acquisitions were made one with excitation RF pulse and one without. The first acquisition was used to calculate the signal and the second acquisition was used to calculate the noise in the images. 37 ROIs (each 45 $pixel^2$) for every slice (5 in total) were chosen inside the phantom (Figure 3.1b) to evaluate FA variation and the SNR inside the phantom.

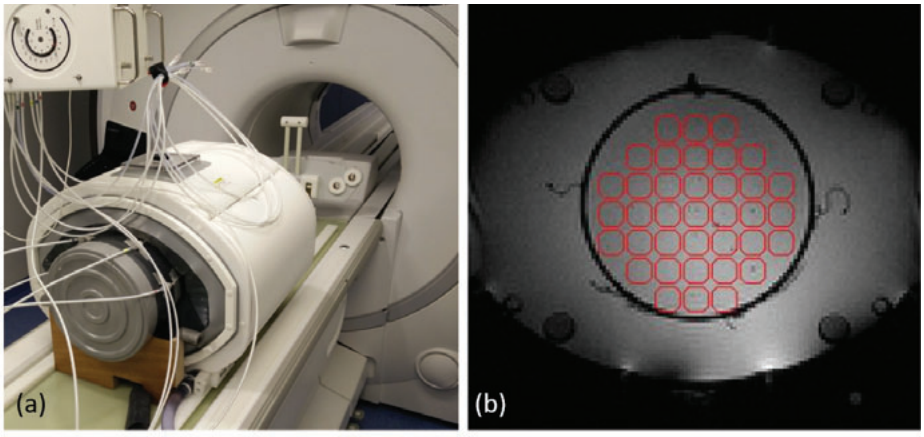

Figure 3.1: Experimental Setup and Post Processing ROIs (a) Sigma Eye MR compatible hyperthermia applicator with cylindrical phantom placed inside (b) Example Magnitude Image and ROIs used for SNR and FA homogeneity analysis

3.3 Results

In Figure 3.2, the measured FA maps for all four setups are shown. The baseline FA maps showed a homogeneous distribution intra-slice (std: 1.8°) as well as along the phantom (std: 1.4°). The measured mean FA was slightly lower than the prescribed value (27.6° vs 30°). The device caused a further reduction, by 1.3°, in the mean FA values. The more drastic effect was observed when the water bolus was filled. The mean FA values dropped to 21.6°, a 28% reduction from the prescribed FA. The heating signal had a smaller but non-negligible impact than the water bolus. The measured mean FA for the final setup was 21.0°.

The applicator didnt change the homogeneity of FA maps intra-slice and along the phantom. The water bolus increased the intra-slice inhomogeneity (std: 2.4°).

In Figure 3.3, the measured SNR for all four setups for two different echo times are illustrated. Results have shown homogeneous values of the baseline SNR intra-slice (0.5 dB) and inter-slice (1.5 dB) with a mean SNR values of 48 dB. The applicator only had a small impact on SNR (reduction by 0.6 dB) while it did not affect the homogeneity. The water bolus caused a big reduction in the measured SNR values for the measurements made with both echo times (38.7 dB and 38.3 dB). It also increased the inhomogeneity to 2.5 dB. The heating signal caused a further 0.8 dB reduction in the SNR.

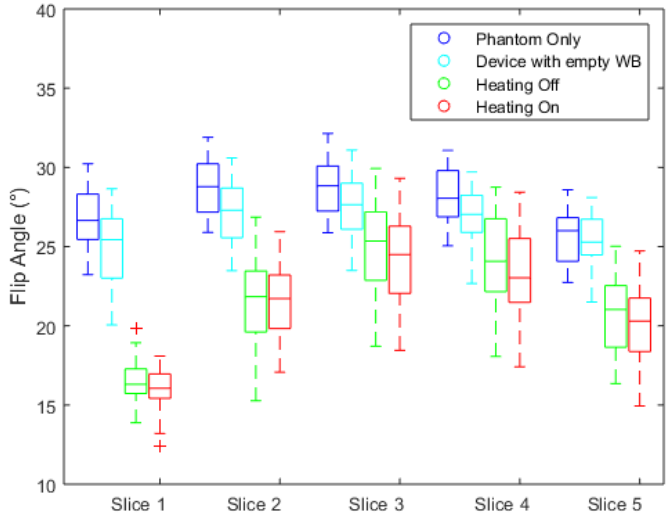

Figure 3.2: Change in Flip angle for four different experimental settings; prescribed FA is 30°.

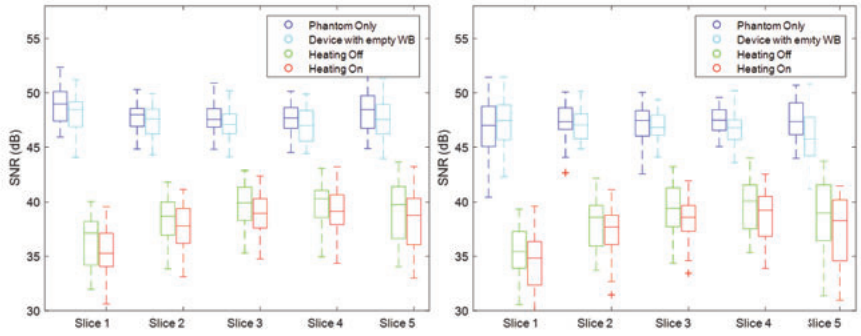

Figure 3.3: Change in SNR for three different experimental settings and different echo times (left) Echo Time 4.6 ms (right) Echo Time 18.4 ms

3.4 Discussion & Conclusions

Our quantitative analysis have shown that the water bolus is the component of the Sigma Eye with the largest impact on the MR image quality. The water bolus reduces the MR RF transmit efficiency and increases the inhomogeneity of the $B_1{}^+$ field. Compared to the effect of water bolus the Sigma Eye applicator (metallic parts) and the 100 MHz RF heating signal, had a less but non-negligible reduction on mean $B_1{}^+$ and SNR values. The reduction in the SNR can be explained by the reduction in signal intensity when a lower flip angle was used.

The negative effect of transmission efficiency can be potentially overcome by increasing the transmit gain of the MRI B_1 field or by altering the prescribed FA value. But another effect that can not be corrected in easy modifications is the increase in inhomogeneity of the FA and SNR maps. This problem calls for more sophisticated approaches on B_1 field shaping or using a thinner water bolus in device design.

Part II:

MR guided hyperthermia treatment

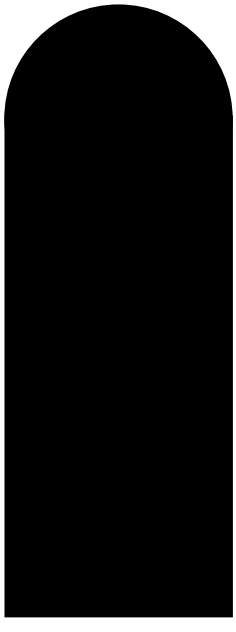

CHAPTER 4

The need for MR thermometry in H&N hyperthermia

This chapter is based on:
K Sumser, E Neufeld, RF Verhaart, V Fortunati, GM Verduijn, T Drizdal, T van Walsum, JF Veenland, MM Paulides. Feasibility and relevance of discrete vasculature modeling in routine hyperthermia treatment planning. *International Journal of Hyperthermia*. 2019 Jan 1;36(1):800-10.

Abstract

Purpose: *To investigate the effect of patient specific vessel cooling on head and neck hyperthermia treatment planning (HTP).*
Materials and methods: *12 patients undergoing radiotherapy were scanned using computed tomography (CT), magnetic resonance imaging (MRI), and contrast enhanced MR angiography (CEMRA). 3D patient models were constructed using the CT and MRI data. The arterial vessel tree was constructed from the MRA images using the graph-cut method, combining information from Frangi vesselness filtering and region growing, and the results were validated against manually placed markers in/outside the vessels. Patient specific HTP was performed and the change in thermal distribution prediction caused by arterial cooling was evaluated by adding discrete vasculature modelling (DIVA) to the Pennes Bioheat Equation (PBHE).*
Results: *Inclusion of arterial cooling showed a relevant impact, i.e. DIVA modelling predicts a decreased treatment quality by on average 0.19 °C (T90), 0.32 °C (T50) and 0.35 °C (T20) that is robust against variations in the inflow blood rate ($|\Delta T|<0.01$ °C). In three cases, where the major vessels transverse target volume, notable drops ($|\Delta T|>0.5$ °C) were observed.*
Conclusions: *Addition of patient-specific discrete vasculature into the thermal modelling can significantly change predicted treatment quality. In cases where clinically detectable vessels pass the heated region, we advise to perform DIVA modelling.*

4.1 Introduction

During hyperthermia cancer treatments, the temperature in the target region is increased to therapeutic levels of 40-44 °C to sensitize tumors cells for the effects of radiotherapy and/or chemotherapy treatments[72]. For head and neck (H&N) cancers, the effectiveness of hyperthermia has been shown in Phase III clinical trials[32,34,149,150]. Hyperthermia dose-effect relationships show that an increase of temperature will further improve treatment outcome[12,47,151]. Our H&N hyperthermia applicator (HYPERcollar3D[41]) allows conformal focused microwave heating of tumors located deeply in the entire H&N region. Mandatory in our treatment strategy is patient-specific hyperthermia treatment planning (HTP) to maximize the microwave power absorption inside the target region while minimizing exposure of sensitive healthy tissues. To improve this procedure, we are investigating replacing the power absorption-based optimization by optimization using patient-specific thermal simulations. In this work we studied if incorporation of vasculature segmentation and discrete vasculature (DIVA) modelling in routine planning would be feasible and if this would result in a relevant change in temperature prediction.

Accurate HTP requires patient specific information: positioning of the patient in the applicator, delineation of the target volume (CTV: clinical target volume as used in radiotherapy planning), tissue segmentation, and electrical and thermal properties of the tissues[55,152]. For the H&N region, we have developed an auto segmentation routine[53,153] and showed that it performs within intra-observer variations[54]. Based on this method, we showed that patient specific thermal properties, i.e. blood perfusion and thermal conductivity, can strongly improve 3D temperature simulation accuracy[154]. That study showed the crucial importance of taking patient specific cooling due to perfusion into consideration. Still, the impact of cooling by the large vessels on top of this microvasculature cooling is unknown.

Cooling in tissues is generally modelled using the bioheat equation described by Pennes[155]. Pennes modelled the heat removal by blood using a homogeneous heat sink term, which scales proportional to the tissue temperature increase above the blood temperature. Although the Pennes model (PBHE) takes the cooling by capillaries adequately into account, the effect of discrete vasculature is ignored which may lead to inaccurate temperature predictions[156,157]. Several thermal models to describe the heat exchange between vessels and tissue have been proposed[158–162], but the discrete vasculature (DIVA) implementation described by Kotte et al.[163,164] and validated by Van Leeuwen et al.[165,166] is the only one that connects vessel tree and 3D FDTD thermal modelling.

An integral part of DIVA is an accurate segmentation of the vessels. Recent developments in angiography made clinical imaging of vessels as small as 0.5 mm possible using computed tomography (CT) or magnetic resonance (MR) scanners[167,168]. For routine HTP, contrast enhanced MR angiography (CEMRA) has advantages over CT angiography since it is non-ionizing, i.e. repeatable, and more sensitive.

In this study, we investigated the impact of arteries on the prediction of the temperature distribution using DIVA modelling added to the classical PBHE thermal model. Twelve rep-

resentative patients underwent CT and MR imaging of the anatomy, as well as CEMRA. The graph-cut method, combining information from Frangi vesselness filtering and region growing, was implemented and validated against manual markers 1) to study the feasibility of auto-segmentation as required in routine HTP and 2) to obtain a detailed vessel model. Next, specific 3D anatomy and vessel tree models of twelve patients were constructed. HTP was performed for each patient and the results of PBHE and combined PBHE+DIVA modelling were compared using predicted hyperthermia treatment quality parameters.

4.2 Methods

4.2.1 Patient Data and Scan Protocols

Institutional review board approval was obtained and 12 patients eligible for radiotherapy treatment in the head and neck region were randomly selected and asked to participate in this study. CT and MRI scan parameters to create the 3D patient models were previously described[169]. For vasculature tree generation, both blanco (pre contrast injection) and arterial sequences were used: TE/TR: 1.93/5.71 ms, FOV 260 mm, slice thickness 0.7 mm, acquisition matrix: 384Œ256, number of slices: 128, flip angle: 25°, contrast injection: 6.5 ml gadolinium contrast agent at 2.5 ml/s, followed by 15 ml saline solution at 2.5 ml/s.

4.2.2 Arterial vessel tree segmentation

Pre-processing of the image data

The images were processed for noise correction using HDCS[170] and bias field correction using the N3 method[171]. To normalize the image intensities all image histograms were matched to a reference image[172] in the dataset. The default parameters were used for HDCS as available in its ITK implementation, and the N3 method parameters were chosen as previously optimized for anatomical sequences of the H&N[173]. For histogram matching, we used 16 landmarks using histograms built with 256 bins.

Graph-cut vessel segmentation

The segmentation method was derived from our previous work[174]. Atlas-based segmentation was combined with intensity modelling using a Graph-cut optimization algorithm for minimization and regularization. Following the terminology of[174], the spatial prior model was based on Frangi vesselness filtering[175] and the intensity model was estimated over the target image using Frangi vesselness combined with region growing based segmentation. The intensity model was built in three steps:

1) Local maxima were found in the Frangi response and used as seed for region growing.

available at http://www.insight-journal.org/browse/publication/748

2) Region growing segmentation was run using the arterial image as input, and seed points from step 1; the lower intensity was determined by getting the 5% level of the intensity histogram of the arterial image in the region of high vessel-probability (defined as having a Frangi response image value higher then 0.05).

3) Using this lower intensity threshold, the region growing algorithm was run using a 26-voxels 3D neighborhood model. The foreground and background intensity models were built by sampling all voxels, within <3mm from foreground, in or outside the region growing segmentation of the vessels, respectively. The models were constructed using Parzen window estimation with a Gaussian kernel of 50 (intensity value unit).

For the graph-cut optimization, we set the association potential weight λ_1 to 1 and the spatial prior weight λ_2 to 0.5 based on visual inspection.

Vessel centerline and radius reconstruction

The MeVisLab skeletonization algorithm[176] was applied using the binary segmentation of the vessels as input. Vessel centerline points and vessel radii per point were obtained and, using a distance based sorting, we determined the vessels' points connectivity, i.e. which points are starting points, end points, bifurcation and normal vessel points. In Figure 4.1, we show an example of the skeletonization algorithm (for each point the vessel radius is available) and the same points with connectivity information. Each vessel tract was defined as the sequence of points from a starting/bifurcation point to an end point/bifurcation point as shown in Figure 4.1. For each tract, we estimated the radius as the average radius of all vessels centerline point in the tract and we use this information to build the vasculature model for thermal simulation.

4.2.3 Electromagnetic modeling and optimization

Patient models were generated from automatic segmentation of CT and MR scans[53,153] and positioning inside the HYPERcollar3D was done by an experienced technician. Electromagnetic distributions were computed using Sim4Life (v.4.0.0.2832, Zurich MedTech, Zurich, Switzerland). The resulting 3D electric field distributions were imported into the treatment planning and guidance software VEDO[52] and amplitude and phase settings per antenna were optimized to maximize the target-to-hotspot energy deposition quotient[52]. EM tissue parameters at 434 MHz are given in Table 4.1 and are from[177].

4.2.4 Thermal modeling

Transient 3D temperature distributions were calculated using the PBHE and the combined PBHE+DIVA solvers in Sim4Life. A 1 mm uniform grid was used in all simulations. Models were simulated for 900 seconds to ensure that steady state is reached. The tissue thermal parameters given in Table 4.1 were used for both models. The listed thermal properties were

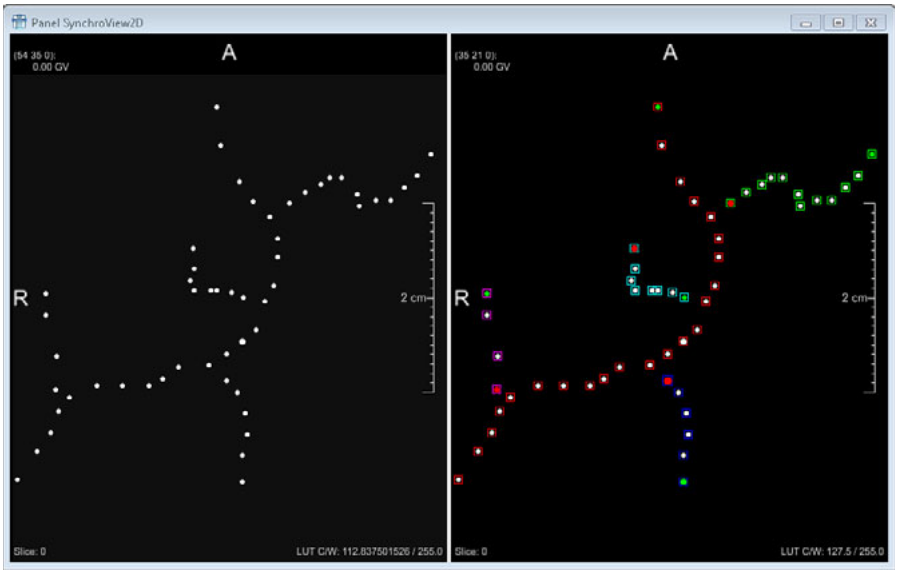

Figure 4.1: Left: vessels skeleton and right: skeleton and connectivity. In this example, green points are starting points, red points are end points and purple points are bifurcations. The color of the squares around the points indicates that the point belongs to a separate tract of the vasculature.

taken from [178], except for tumor perfusion and thermal conductivity in muscle, fat and tumor, which were taken from [154]. The effect of thermoregulation was not modelled and values for constant perfusion were used. The SAR level, i.e. total input power, was increased until the maximum temperature in the healthy tissue reached 44 °C in the PBHE model. For the first analysis, an identical power level was used in the combined PBHE+DIVA modelling to compare the maximum predicted temperature in healthy tissue. Subsequently, the total input power of the PBHE+DIVA simulation was increased to reach a maximum healthy temperature of 44 °C. The patient initial temperature was set to 37 °C and mixed boundary conditions were applied using the following values for the heat transfer coefficients (h) and outside temperature (T): tissue background (h = 8 [W/m^2/°C], T = 20 °C, [179]), tissue internal air / lungs / (dental) metal implants (h = 50 [W/m^2/°C], T = 37 °C, [179]), tissue water bolus (h = 292 [W/m^2/°C], T = 30 °C; derived from in house measurement involving the devices water bolus).

For DIVA simulations, the inflow temperature of the blood was set to 37 °C. For every vessel the following settings were used: bucket density = 1000 m^{-1}, Nusselt Number = 3.66, blood initial temperature = 37 °C, blood thermal conductivity = 0.52 W/m/°C, blood heat capacity = 4.05x10^6 J/m^{-3}/°C. The inflow rate values for the arterial tree were fixed as in [180], i.e. 275 mL/min for the two internal carotid arteries (ICA) and 90 ml/min for the two

Table 4.1: EM and thermal simulation properties of tissues. ϵ_r: relative permittivity; σ: conductivity (S/m); ρ: density (kg/m^3); c: Specific heat capacity (J/kg/°C); k: thermal conductivity (W/m/°C); Q: metabolic heat generation rate (W/kg); ω: perfusion rate (mL/min/kg)

Tissue	ϵ_r	σ	ρ	c	k	Q	ω
Internal air	1.00	0.0	1.2	-	-	-	-
Bone	13.07	0.09	1908	1313	0.32	0.15	10
Brainstem	55.11	1.05	1045.5	3630	0.51	11.4	558.6
Cartilage	45.14	0.60	1099.5	3568	0.49	0.54	35
Cerebellum	55.11	1.05	1045.5	3696	0.55	15.5	763.3
Cerebrum	56.81	0.75	1044.5	3653	0.51	15.7	770
CSF	70.63	2.26	1007	4096	0.57	0.0	763.3
Fat	11.59	0.08	911	2348	0.50	0.51	255
Grey matter	41.66	0.45	1041	3696	0.55	15.54	764
Lens	37.29	0.38	1075.5	3133	0.43	-	-
Lung	23.58	0.38	394	-	-	-	-
Muscle	56.87	0.80	1090.4	3421	0.4	0.96	442.8
Myelum	35.04	0.46	1075	3630	0.51	2.48	160.3
Optical nerve	35.04	0.46	1075	3613	0.49	2.48	160.3
Sclera	57.37	1.01	1032	4200	0.58	5.89	380
Thyroid gland	61.33	0.89	1050	3609	0.52	87.1	5624.3
Tumor	59.00	0.89	1050	3950	1.5	-	848
Vitreous humor	69.00	1.53	1004.5	4047	0.59	-	-
White matter	56.81	0.75	1044.5	3583	0.48	4.32	212

vertebral arteries (VA). To assess the robustness against inflow rate variations, they were modified to represent high (ICA 325 mL/min, VA 108 mL/min) and low (ICA 225 mL/min, VA 72 mL/min) flow rates. At bifurcations, the flow rates were distributed over child vessels proportional to the cubic ratio of their diameters according to Murrays Law[181].

Each DIVA simulation required 30M Cells and took on average 4 hours at a standard desktop computer with i5-3550 processor.

4.2.5 Evaluation parameters

The results of the graph-cut vessels segmentation method were benchmarked against manual annotations regarding sensitivity, specificity, accuracy, and precision:

- Sensitivity= TP/(TP+FN)
- Specificity= TN/(TN+FP)
- Accuracy= (TP+TN)/(TP+TN+FP+FN)

- Precision= TP/(TP+FP)

As ground truth, vessel and background (no vessel) landmarks points were manually placed in pairs by a medical student. In total, 1760 vessel and 5585 background points were placed axially distributed over all patients and over 10 slices per patient. Every vessel landmark is matched with a background landmark near the vessel surface to be sensitive to mis-segmentation.

The impact of the extension of PBHE modelling with DIVA on the temperature simulation was analyzed using the hyperthermia quality parameters T90, T50, and T20, i.e. the iso-temperature levels encompassing 90%, 50% and 20% of the CTV, respectively. A two sample t-test was used to test for statistical significance.

4.3 Results

In Figure 4.2, a visual example of vessel segmentation by the graph-cut method is shown. On the left, the detected voxels (highlighted in purple) are shown overlaid on coronal MRA image. On the right, the resulting full arterial tree ready to be inserted in the thermal simulation, is visualized.

The sensitivity of the graph-cut segmentation method was 0.85, and specificity was 0.97. These high sensitivity and specificity values are desired to correctly identify the vessel locations. The method also provided high accuracy (0.94) and precision (0.9), which is very desirable since the thermal modelling is severely affected by false positives and false negatives. Hence, the good all-round performance of the method and visual inspection suggest that it is sufficient for thermal modelling.

Figure 4.3 shows the maximum temperature reached in the healthy tissue with the DIVA model when the same power as in the PBHE is used in the PBHE+DIVA model. In DIVA+PBHE models for 5 patients (Patient 1, 7, 9, 11, and 12), the achieved maximum temperatures in the healthy tissue (using the same power levels as in the corresponding PBHE models) decreased by more than 0.2 °C. The maximum change in the peak temperature was observed in Patient 9, where the maximum temperature was 1.4 °C lower than in the PBHE model.

Figure 4.4 shows the difference in achieved HTP quality parameters in the CTV. T50 of 5 / 12 patients decreased notably ($|\Delta T50| \geq 0.20$ °C) in the presence of arterial cooling. The T50 values in the DIVA simulations were on average 0.30 °C lower, but 1 / 12 patient showed an insignificant increase in T50 ($\Delta T50 = 0.05$ °C). In two cases, where the heating target-volume was in the vicinity of a blood vessel, cooling was increased by up to 1 °C. There was no clinically relevant difference in the lowest target temperature indicator, i.e., average $\Delta T90$ = -0.16 °C. The maximum temperature surrogate T20 showed the biggest change between the models (average $\Delta T20$= -0.33 °C). The maximum drop in predicted T50 was 1.00 °C, where the temperature distributions for both models are illustrated in Figure 4.5. The vessels pass through the target area and create cold tracks in their paths.

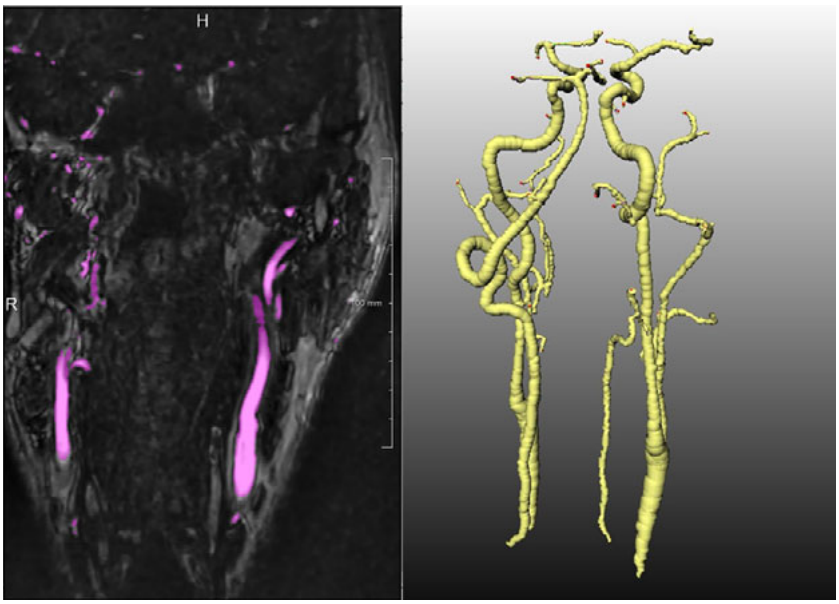

Figure 4.2: An example result of the graph-cut vessel segmentation algorithm. Pre-processed coronal slice of the MRA image of a patient with vessels segmentation color overlay in purple (left), and the skeletonization of the arterial vessel tree (right).

Still, our statistical analysis did not show a significant reduction in HTP quality parameters (T90: $p = 0.64$, T50: $p = 0.45$, T20: $p = 0.38$) for the total of the 12 patients. The robustness study regarding variations in the flow rates produced changes below 0.01 °C in all cases.

4.4 Discussion

In this paper, we report our analysis on the effect of discrete vasculature in the H&N region. We found a notable drop in treatment quality parameters with the arterial DIVA model compared to the PBHE model. Although the differences in the values are moderate on average (0.30 °C), for three patients (Patient 6, 7, and 8), a large drop in the achieved temperature metrics was observed (average drop 0.92 °C), presumably because the target volumes in these patients are significantly exposed to traversing parts of the arterial trees. Exclusion of these three patients brings the average difference in HTP quality parameters to 0.09 °C. This fact highlights the importance of DIVA modelling in specific cases when the target volume is in the vicinity of the vessel tree.

To our knowledge, these are the first reported results on the use of a clinical workflow

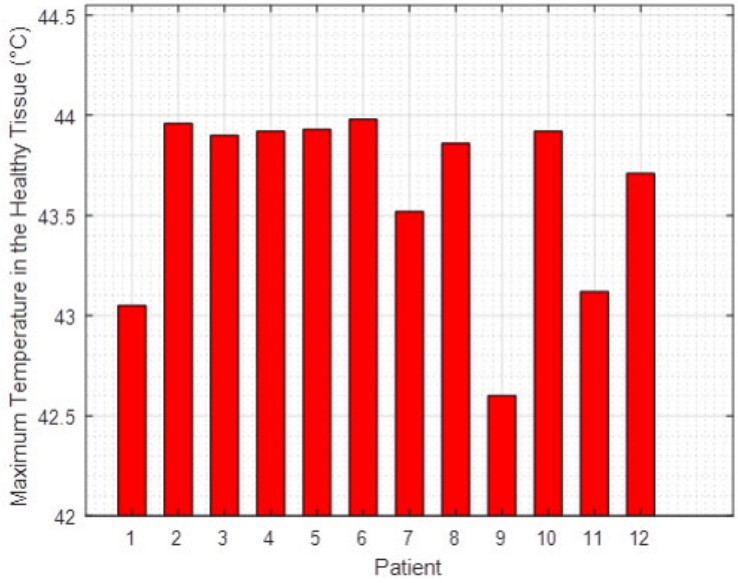

Figure 4.3: Maximum temperatures in the healthy tissue reached in PBHE+DIVA models with the same input powers as in PBHE models. The maximum temperature in the healthy tissue was 44 °C in the PBHE model.

to implement patient specific thermal modelling of discrete vasculature in HTP including acquisition of vasculature data. Other authors did study the impact of DIVA modelling for other scenarios or using a non-patient specific vessel network. Van Lier et al.[182] evaluated and compared PBHE and PBHE+DIVA models regarding the maximum temperature increase in the head after exposure to a 300 MHz radiofrequency field induced by MRI coils. They reported 0.5 °C difference in the maximum temperature increase predictions. Our approach of focusing on target volume prevents a comparison with their results, which were obtained using a more homogenous B_1 field that is desirable in MRI. Our findings confirm that PBHE only predictions can overestimate the temperature increase. For exposure by a mobile phone, Flyckt et al.[183] also reported lower maximum temperature rise with a DIVA model of the eye. Using data from a healthy volunteer, supplemented by a vessel network from a previous study[157], Kok et al.[184] studied the differences in HTP quality parameters in the pelvis region when using DIVA modelling. They saw 0.2 °C, 0.4 °C, and 0.6 °C decrease in T90, T50, and T10. The higher difference they found can be explained by the fact that their maximum allowed temperature in the healthy tissue was 45 °C, which is higher than in our clinical protocol.

The graph-cut segmentation is a trade-off between region growing and Frangi vesselness

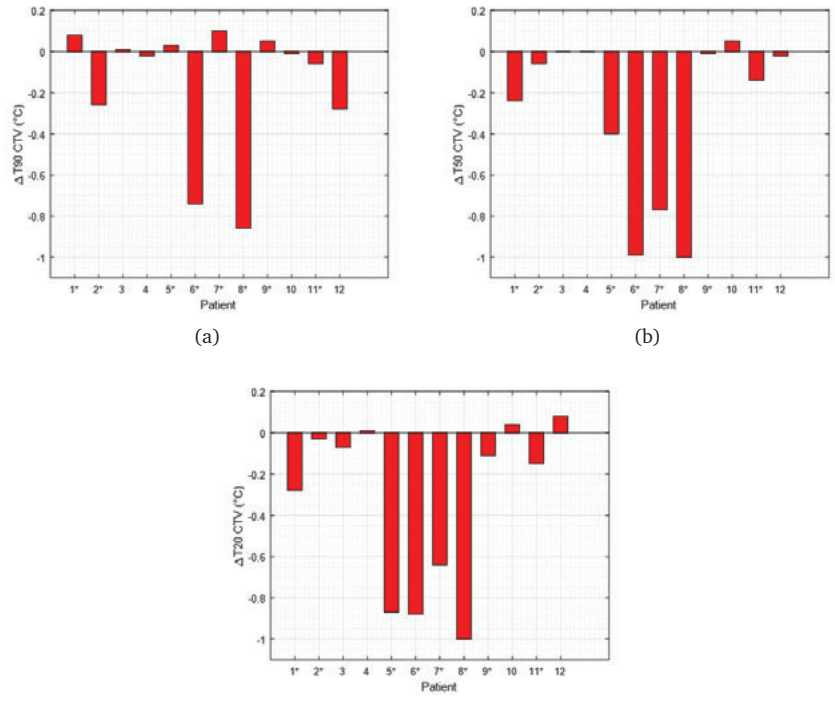

Figure 4.4: Differences in HTP quality parameters in the CTV (a) ΔT90 ($|\Delta T90_{avg}| = 0.16$ °C), (b) ΔT50 ($|\Delta T50_{avg}| = 0.30$ °C), (c) ΔT20 ($|\Delta T20_{avg}| = 0.33$ °C). * next to the patient number denotes a target volume that includes a part of the vessel tree.

based segmentation. Frangi has a low sensitivity because the vessel boundaries are not accurately segmented due to the effect of the Gaussian smoothing. Conversely, region growing segmentation tends to 'leak' including high intensity background region as foreground. Graph-cut segmentation provides better boundaries without including spurious high intensity regions in the vessel segmentation.

There are some limitations regarding the accuracy of thermal modelling in this study. Arteries with diameters larger than 0.5 mm were captured in the MRA images. Arteries with diameters in the range of 0.1-0.5 mm may affect the accuracy of PBHE+DIVA models[185]. This resolution is not achievable with current clinically available imaging technologies. Furthermore, the arteries reconstructed in this study (diameter $>$ 0.5 mm), nearly always are accompanied by a counter-current vein[186]. When this venous flow originates from a heated

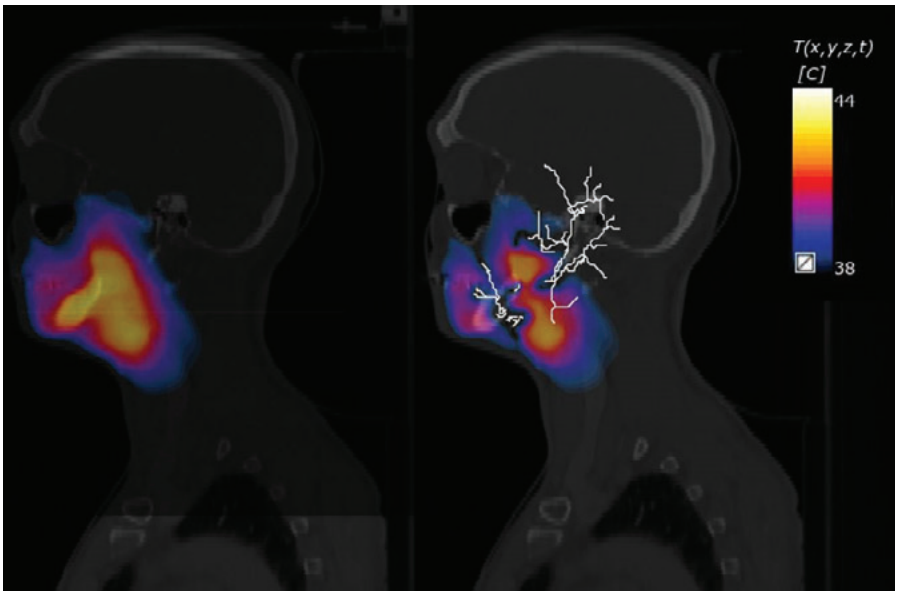

Figure 4.5: Example temperature distribution maps overlaid on CT images for PBHE (left), and DIVA (right).

volume, counter-current heat exchange will increase the temperature of arterial flow (venous rewarming). A correction coefficient has been suggested to account for this effect[161]. If the venous flow originates from a cold volume; there will be no venous rewarming. As the target volume in the H&N hyperthermia is only about 250 ml, i.e. much smaller than in pelvic hyperthermia, counter-current venous rewarming is not expected. Since venous flow is much slower than arterial flow, very little independent cooling by the veins is expected[185]. Thus, we regard the effect of arteries reported in this study a good estimate of the minimum difference that can be expected in the clinic.

In vivo validation of the vasculature effect on head and neck hyperthermia treatment quality has some challenges. The concept of DIVA thermal modelling was validated ex vivo by Raaymakers et al.[187] using a perfused bovine tongue. A specific validation for the H&N region would require in vivo temperature measurements near vessels. During H&N hyperthermia, placement of invasive temperature probes is challenging and risky and therefore often not feasible[42]. In addition, the thermo-sensors are positioned at a safe distance from the vessels to avoid complications like artery puncturing[57]. Hence, non-invasive measurements like magnetic resonance temperature imaging (MRTI) hold the greatest promise for validation of the discrete vasculature modelling. However, the accuracy of MRTI strongly varies depending on the distance to distortions and confounders. Hence, a validation study requires the most advanced MRTI techniques, dedicated MR-hyperthermia equipment and careful

planning.

Although the HTP quality parameters are commonly used as surrogates and have been shown to correlate with the treatment outcome[47,188], they are not sensitive to minimum temperatures. Hence, local vessel cooling may create small under-dosed areas where hyperthermia is less effective potentially leading to tumor recurrences. We hypothesize that the correlation between macroscopic quality parameters and treatment outcome is an indicator that ionizing radiation alone is sufficiently effective in those regions, which are highly oxygenized regions. An analysis on the thermal enhancement ratio[189] in these regions might provide different results. However, more research on the biology of hyperthermia on a local scale is needed for definite answers.

Inclusion of DIVA into the HTP scheme is necessary for correct thermal dose estimation. Additionally, to reach maximum allowed temperature limits in the healthy tissue, we showed that power on average needs to be increased by more than 6% when considering DIVA. Failing to deliver the correct power levels can result in a decrease in T50 by on average 0.45 °C. However, the benefits of patient specific vasculature information come with additional burden to the patient. Patients have to stay in the scanner for another ten minutes. In addition, although fast DIVA simulation tools have been developed[184], these are not commercially available and only predict temperatures in steady state. Transient implementations of the DIVA model involve long simulation times, which makes the integration of DIVA into complaint adaptive online HTP unrealistic[52].

4.5 Conclusion

Our analysis, based on twelve patient models, showed no significant decrease of the target temperature isopercentiles when including the effect of patient specific vasculature information into the PBHE model. Nevertheless, in specific cases, where major vasculature traverses the strongly heated target volume, a clinically relevant difference was observed. Based on these findings about the impact of the vasculature above 0.5mm in diameter, we advise to consider DIVA modelling if such vessels are passing through the heated region. For the vessel tree segmentation and extraction from CEMRA, the graph-cut method has good automation potential: it performs well in terms of accuracy, precision, and specificity without losing on sensitivity.

CHAPTER 5

Design of the MRcollar

This chapter is based on:
T Drizdal, **K Sumser**, GG Bellizzi, O Fiser, J Vrba, GC van Rhoon, DTB Yeo, MM Paulides, Simulation guided design of the MRcollar: a MR compatible applicator for deep heating in the head and neck region. *International Journal of Hyperthermia*. 2021 March 7;38(1):382-392.

Abstract

Purpose: *To develop a head and neck hyperthermia phased array system compatible with a 1.5 T magnetic resonance (MR) scanner for non-invasive thermometry.*

Materials and methods: *We designed a dielectric-parabolic-reflector antenna (DiPRA) based on a printed reflector backed dipole antenna and studied its predicted and measured performance in a flat configuration (30 mm thick water bolus and muscle equivalent layer). Thereafter, we designed a phased array applicator model (MRcollar) consisting of 12 DiPRA modules placed on a radius of 180 mm. Theoretical heating performance of the MRcollar model was benchmarked against the current clinical applicator (HYPERcollar3D) using specific (3D) head and neck models of 28 treated patients. Lastly, we assessed the influence of the DiPRA modules on MR scanning quality.*

Results: *The predicted and measured reflection coefficient (S_{11}) of the DiPRA module are below -20 dB. The maximum specific absorption rate (SAR) in the area under the antenna was 47% higher than for the antenna without encasing. Compared to the HYPERcollar3D, the MRcollar design incorporates 31% less demineralized water (-2.5 l), improves the predicted TC25 (target volume enclosed by 25% iso-SAR contour) by 4.1% and TC50 by 8.5%, while the target-to-hotspot quotient (THQ) is minimally affected (-1.6%). MR experiments showed that the DiPRA modules do not affect MR transmit/receive performance.*

Conclusions: *Our results suggest that head and neck hyperthermia delivery quality with the MRcollar can be maintained, while facilitating simultaneous non-invasive MR thermometry for treatment monitoring and control.*

5.1 Introduction

Hyperthermia has proven beneficial when added to standard radiotherapy and chemotherapy for treatment of many tumor locations, including the head and neck (H&N) [11,17,72,190]. In order to elevate the temperature in the H&N region to the desired range of 40-44 °C, we have previously developed the unique HYPERcollar3D applicator consisting of 20 patch antennas operating at 434 MHz [43,44]. At Erasmus MC, hyperthermia using the HYPERcollar3D is being applied once a week for 75 minutes after the radiotherapy treatment [42]. The temperature during the hyperthermia is measured superficially and, whenever possible, interstitially by sets of fiber optic probe sensors placed in closed tip catheters. Magnetic resonance (MR) imaging has shown to have a clinical potential for noninvasive temperature measurement in the pelvic region, however no device exists for MR-hyperthermia in the H&N [191,192]. In 2012, we therefore started to study the feasibility of integrating the hyperthermia H&N device into an MR scanner for noninvasive MR thermometry by developing a novel applicator: the MRcollar.

Integrating a hyperthermia system into the MR requires the use of nonmagnetic components and design principles that minimize system-induced image artifacts. One example for this is the minimization of large electrically conductive surfaces that can generate undesired gradient-induced eddy-currents or shield certain regions of interest from the MR radiofrequency (RF) transmit fields. Previously, we redesigned the HYPERcollar3D and experimentally showed the feasibility of applying hyperthermia in a 1.5 T GE 450w MR scanner using the "MRlabcollar", a laboratory prototype consisting of 12 patch antennas operating at 434 MHz [61,107,109]. In those measurements, we observed that the connectors of the antennas caused image distortion in the MR thermometry images, even if the effects were located on the periphery of the water bolus structure and not within the region of interest. Motivated by the negligible MR distortions found for the self-grounded bow-tie antenna, we developed the Yagi-Uda antenna, which has a smaller cross-section of metal obstructing the B_1^+ field [124,193,194].

Noninvasive MR thermometry using the MR scanner is clinically available for deep hyperthermia in the pelvic region using the Sigma Eye system (Pyrexar Medical, Salt Lake City, USA) [99,100]. Sigma Eye and MRlabcollar use independent systems for MR thermometry and hyperthermia heating. This differs from other approaches where the hyperthermia and MR imaging functionalities are embedded into a common antenna structure. It was demonstrated that a 3 T MR surface loop coil array can be modified in real time into a C-shaped dipole antenna phased array for hyperthermia heating using fast RF switches [128,195]. As an alternative, Winter et. al proposed to use a bowie-tie antenna system for imaging and heating at 7 T (298.6 MHz) [77,130]. Both these approaches use the MR scanner RF amplifiers for heating and thus do not allow truly simultaneous heating and imaging. Further they also restrict the heating frequency to the Larmor frequency, which is often not the optimum choice considering focusing and operational costs. Hence, the optimum choice might be an appropriate co-design of a heating antenna array and imaging coil arrays. We selected 434 MHz as operating frequency as it is within the band of optimum frequencies [196] and an ISM

(industrial, scientific and medical) frequency for which low-cost amplifiers are available. This frequency is also sufficiently far from the Larmor frequency (64 MHz) and higher order modes of a 1.5 T MR scanner, which enables decoupled operation for truly simultaneous noninvasive MR thermometry[192].

The purpose of this study was to use 3D electromagnetic (EM) field modelling to design a clinical applicator prototype for MR guided deep hyperthermia treatment in the H&N region. In the first step, we designed the dielectric parabolic reflector antenna (DiPRA) module. In the second step, we used a dedicated measurement setup to verify the predicted reflection coefficient and radiation characteristic of the DiPRA module. Based on this module, we then created a phased array applicator (MRcollar) model and tailored its dimensions to the average H&N patient. Forth, the predicted heating capabilities of the MRcollar design were evaluated against the clinically used HYPERcollar3D applicator[55]. Finally, MR experiments were carried out to assess the influence of the DiPRA modules on MR scanning quality.

5.2 Methods

5.2.1 Antenna encasing - DiPRA module

Figure 5.1a shows the original Yagi-Uda antenna model in Sim4Life, for which heating performance and MR compatibility were verified in a previous study[124]. The antenna was manufactured of an FR-4 printed circuit board and operates at 434 MHz. It is partly submerged in the de-mineralized water bolus, which allows reducing the antenna size, efficient EM energy transfer and cooling of the patient surface. The director of the printed circuit board (PCB) Yagi-Uda antenna (Figure 5.1a) was removed to reduce axial size and because it induced significant sensitivity in impedance characteristics to the cavity enclosing. This removal resulted in a reflector backed dipole antenna shown in Figure 5.1b. To reduce the amount of water needed, minimize the cross-coupling and improve focusing, we designed a specific encasing with a parabolic back shape shown in Figure 5.1c, a dielectric parabolic reflector antenna (DiPRA). The width of the DiPRA encasing (we), shown in Figure 5.1c, is determined by the 70 mm printed reflector backed dipole antenna width. The height (he) was selected such that the specific absorption rate (SAR) in the muscle equivalent phantom was not influenced by this dimension. The distance between antenna and cavity top (d_{a-e}) and the thickness of the top encasing part (d_{et}), shown in Figure 5.1d, were selected to have a minimum influence on the antenna reflection characteristics.We placed the DiPRA module on a 30x300x300 mm^3 water bolus and a 100x300x300 mm^3 muscle equivalent phantom model, and studied reflection coefficient and SAR characteristics. For the FR-4 substrate we applied $\epsilon_r = 4.66$, $\sigma = 1.9$ mS/m, $\sigma = 1850$ kg/m^3 dielectric properties, for the antenna encasings $\epsilon_r = 2.6$, $\sigma = 4$ mS/m, $\rho = 1180$ kg/m^3, for the water bolus $\epsilon_r = 80$, $\sigma = 0.04$ S/m, $\rho = 1000$ kg/m^3 and for the phantom $\epsilon_r = 56.9$, $\sigma = 0.81$ S/m, $\rho = 1090$ kg/m^3.

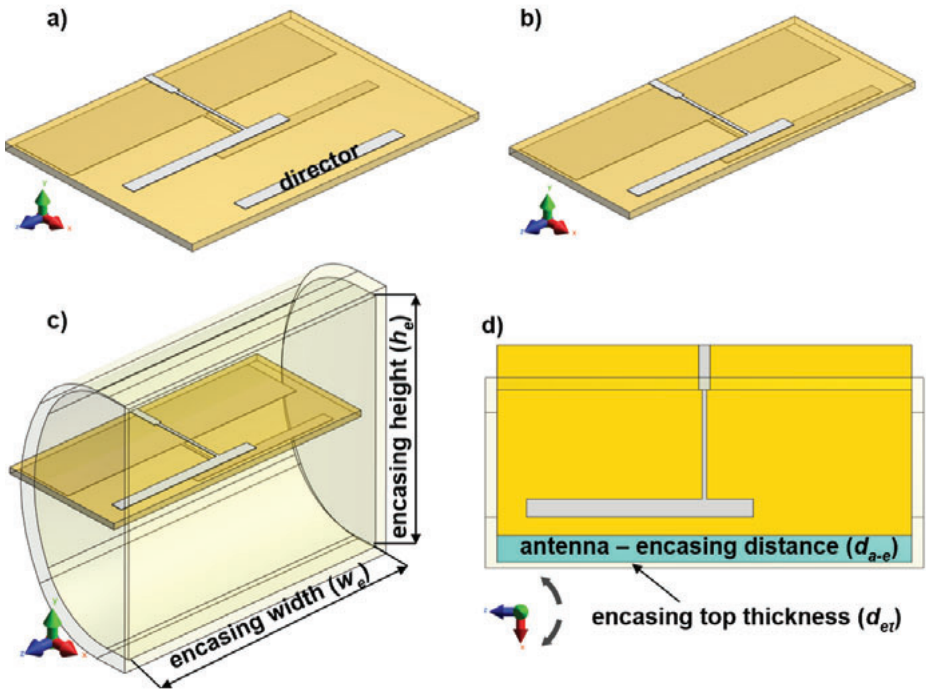

Figure 5.1: Models of a) original Yagi-Uda antenna including director, b) reflector backed dipole antenna, c) dielectric parabolic reflector antenna (DiPRA) module, d) 2D planar cross-section of the DiPRA module.

5.2.2 DiPRA module verification measurements

To validate this embedded antenna concept, we created a dedicated measurement setup in Sim4Life, as shown in Figure 5.2a. Figure 5.2b shows the manufactured setup using polyethylene terephthalate glycol (PET-G) filament printed with 0.4 mm nozzle diameter, 0.25 mm layer height and 100% filling factor at Prusa i3 MK3 (Prusa Research, Prague, Czech Republic) 3D printer. A two-component epoxide glue (Chemex POX Z 21, Prague, Czech Republic) was applied for antenna fixation and coating of the 3D printed part ensuring water resistance of the entire measurement setup. We also 3D printed a 30 mm height frame for the water bolus filled with demineralized water. For the reflection coefficient measurements, we created a phantom with muscle equivalent properties at 434 MHz consisting of demineralized water, salt and isopropyl alcohol. The concentrations of the individual components were adjusted in a few iterative steps using dielectric assessment kit DAK-12 (SPEAG, Zürich, Switzerland) connected to N9923A (Keysight, Santa Rosa, USA) and a FieldFox vector network analyzer. This procedure resulted in a liquid phantom with a relative permittivity of

$\epsilon_r = 56.4$ and an electric conductivity of $\sigma = 0.79$ S/m. These values were very close to the literature values for muscle of $\epsilon_r = 56.9$ and $\sigma = 0.81$ S/m used for the hyperthermia treatment planning purposes withing this study. The reflection coefficient characteristics were measured for different encasing top thicknesses, ranging from 0.5 mm to 1.5 mm, using a liquid phantom and a FSH8 Rohde&Schwarz (Munich, Germany) vector network analyzer.

For the SAR measurements, we prepared a solid phantom following the procedure recommended for superficial hyperthermia quality assurance[197]. The phantom consisted of demineralized water, salt, agar powder, TX-151 and polyethylene powder and its dielectric properties ($\epsilon_r = 66$, $\sigma = 0.92$ S/m) were measured using DAK-12. The phantom was filled in eight 10 mm 3D printed frames which were placed on the top of another inside the 3D printed container. After heating period, the whole phantom was taken out from the container and two 2D profiles in depth of 12.8 mm and 24.5 mm depths measured by removing top phantom layers. These thicknesses correspond to the manually measured thicknesses of the first and second phantom layers after phantom creation. The SAR characteristics were measured using E60 FLIR (FLIR Systems, Wilsonville, USA) for the scenario without antenna encasing cover and for the scenario with a 1 mm thick cover. The 75 W harmonic signal at 434 MHz was excited using a PG 70.150.2 (SSB Electronics GmbH, Lippstadt, Germany) power generator and guided via a ZGBDC30-372HP+ (MiniCircuits, Brooklyn, USA) bi-directional coupler towards the DiPRA panel SMA type connector. Forward and reflected power were acquired using two PWR-6GHZ (MiniCircuits, Brooklyn, USA) power meters connected with 20 dB additional attenuation to the outputs of the bidirectional coupler. Its attenuation and coupling characteristics were measured at the beginning of the experiments with a FSH8 vector network analyzer. We calculated SAR using the specific heat capacity (c = 3640 J/kg/K) multiplied by the empirical rate of temperature rise. The latter is computed from the ratio of measured temperature increase (subtracted 2D infrared images after and before the heating) and the measurement time (four minutes). SAR was normalized to 1 W input power to enable comparison of predicted and measured SAR distributions. The predicted 2D SAR profiles were extracted at corresponding depths from homogenous phantom model.

5.2.3 MRcollar design

Figure 5.3a shows the simulation setup of the MRcollar model consisting of 12 antennas organized in two 2x3 DiPRA arrays applied from left and right side of the patient H&N model. Distances between individual DiPRA modules and the patient surface characterize the water bolus thickness. To provide more evenly distributed water bolus pressure to the patient and a more homogenous water circulation throughout the water bolus, it is desirable to keep the water bolus thickness constant for the whole MRcollar model. We approximated the surface of the representative patient with a radius of curvature of 150 mm, to which we added 30 mm of water bolus thickness. This resulted in the final 180 mm radius of the both 2x3 arrays parts of the MRcollar model shown in Figure 5.3b. A rounding with a radius of 180 mm was applied to the footprint of the antenna modules in order to provide better

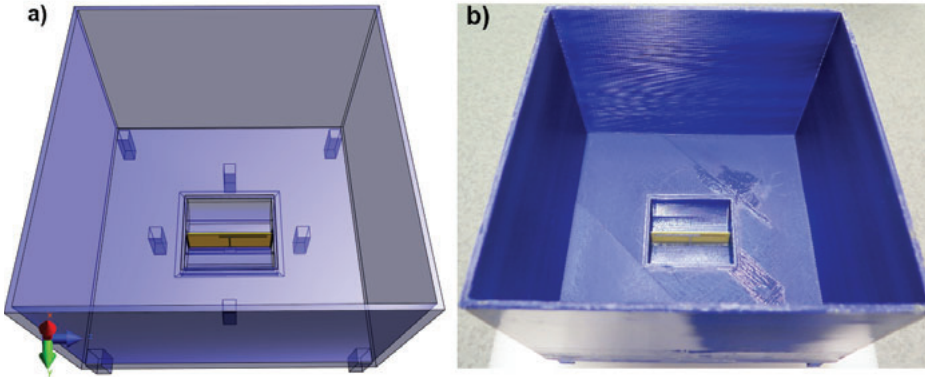

Figure 5.2: a) Model of DiPRA verification setup (note that the 3D printed part model is transparent and perspective view is used for better clarity), b) manufactured setup using 3D printer technology.

contact between water bolus and the modules.

5.2.4 MRcollar model heating capabilities

Heating capabilities of the clinically used HYPERcolar3D and the MRcollar model were evaluated on data from 28 H&N patients for which hyperthermia treatment planning (HTP) was previously done. The patient group consisted of 14 oropharynx, five neck node, three nasopharynx, three larynx, two oral cavity and one hypopharynx tumors, i.e., 19 males and

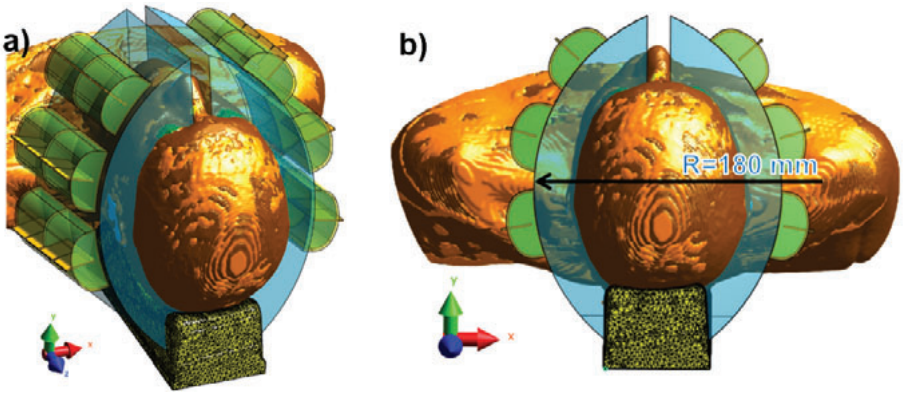

Figure 5.3: a) MRcollar model in Sim4Life, b) MRcollar model with highlighted radius R=180 mm.

nine females with a mean age of 63.1±11.2 years. Patient specific 3D H&N models were created from computed tomography (CT) images using an atlas based automatic segmentation routine followed, if necessary, by manual adjustments in iSeg (v. 3.8, Zürich MedTech AG, Zürich, Switzerland)[54]. Then the patient models were imported into Sim4Life (v. 4.4, Zürich MedTech AG, Zürich, Switzerland), together with the HYPERcollar3D or the MRcollar model, for EM field simulations. All dielectric properties were assigned from the ITIS database available in Sim4Life at 434 MHz[178]. For the HYPERcollar3D models, we used 1.5 mm global finite difference time domain (FDTD) grid step refined to 1.25 mm within the HYPERcollar3D model and to 0.75 mm for the patch antenna parts. For the MRcollar models, we used 1.5 mm global FDTD grid step refined to 1 mm for the antenna encasing, 0.75 mm for the metallic antenna parts and 0.5 mm at the discrete edge source feeding. Typical size of the whole FDTD calculation domain for both models was around 90 million cells. A 434 MHz excitation and 20 periods of harmonic signal were applied for each antenna. We used computed unified device architecture (CUDA) acceleration at nVidia GTX 1080 Ti graphical processor units resulting in a typical computation time for each simulation of 35 minutes for the MRcollar model and 15 minutes for the HYPERcollar3D model.

Afterwards, all simulations were exported to VEDO, our in-house developed visualization tool for electromagnetic dosimetry and optimization[52]. VEDO allows pre-treatment and online optimization of the amplitude and phase feeding signals of individual antennas in order to maximize the EM field energy focus in the target region. It uses the particle swarm optimization toolbox to optimize target-to-hotspot quotient (THQ) representing a ratio between the average SAR in the target and the average SAR in the hotspot (total volume with the highest 1% SAR outside the target)[198,199]. In addition to THQ, we also compared the target volume coverage of the 25% and 50% SAR iso-contour, TC25 and TC50.

5.2.5 MR assesment of antenna encasing - DiPRA module

We investigated the influence of the DiPRA module on MR quality following the tests recommended in Hoffmann et al.[200]. Three comparative tests were used to assess the absence of field distortions on B_0 and $B_1{}^+$ as well as SNR performance, respectively. Although DiPRA modules are not intended to be used as MR transmit or receive coils for which the guidelines in Hoffmann are designed, these tests are relevant to investigate possible MR distortions caused by the DiPRA modules. In that regard, both one and two DiPRA modules scenarios were tested. In the experimental setup, the DiPRA modules were placed on top of a static water bolus that was positioned in turn on top of a calibration phantom provided by the MR vendor (GE Medical Systems - MR Division, Waukesha, WI, CTL Lower TL, P/N U1150027: $T_1 = 108$ ms; $T_2 = 96$ ms). Both B_0 field and flip angle distortions were assessed by comparing the homogeneity in a single slice when the DiPRA modules are present to the homogeneity when they are absent. B_0 field homogeneity was measured with a dual echo gradient echo sequence[201] (slice thickness 2.9 mm, FOV 300x300 mm2, matrix 256x256, TR/TE1/TE2 243/4.6/9.2 ms, NEX 1, flip angle 15°). The flip angle field map was measured using the Bloch-Siegert method[148] (slice thickness 5 mm, FOV 300x300 mm^2, matrix

128x128, TR/TE 20/14 ms, NEX 1, flip angle 30°). SNR was measured using a spoiled gradient echo sequence (slice thickness 2 mm, single slice, FOV 300x300 mm^2, matrix 256x256, TR/TE 75/4.5 ms, NEX 1, flip angle 60°). In order to evaluate the homogeneity of the different fields and compare them, a central region of interest (ROI) was defined, 30 mm deep in the phantom.

5.3 Results

5.3.1 Antenna encasing - DiPRA module

Figure 5.4a shows the influence of the distance between the antenna and the encasing cover d_{a-e} (mm) on the antenna reflection coefficient, with the minimum S_{11} = -44.6 dB obtained for a distance of 5 mm. We selected d_{a-e} = 4.5 mm, to account for a larger distance in the curved antenna encasing, ensuring good matching (S_{11} = -32 dB). Figure 5.4b illustrates the linear relationship between the top encasing thickness d_{et} (mm) and antenna resonant frequency, calculated for d_{a-e} = 4.5 mm. Even though the optimum thickness for resonance at 434 MHz is d_{et} = 0.85 mm, we selected d_{et} = 1 mm to ensure mechanical and waterproof stability of the antenna encasing.

Figure 5.5a shows the normalized SAR depth profiles for the reflector backed dipole antenna placed in: 1) a flat (brick-shaped) volume of deionized water, 2) encasing without the cover and 3) in full encasing, i.e., the DiPRA. In Figure 5.5a, penetration depths equal to 20 mm are

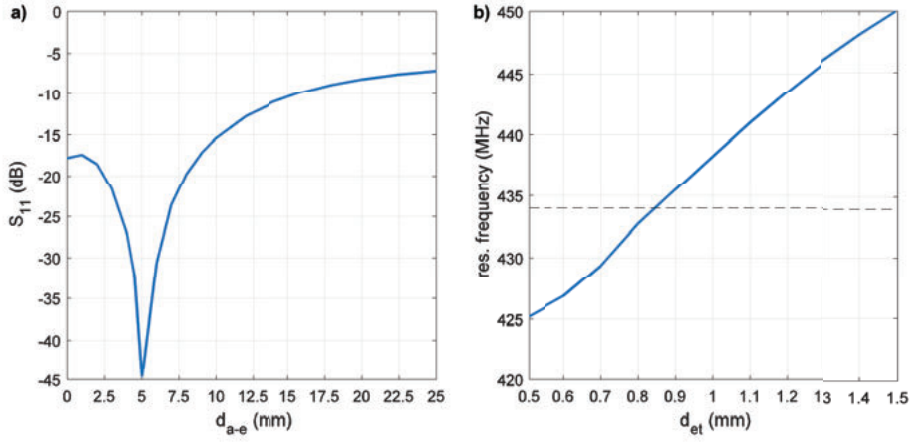

Figure 5.4: a) Reflection coefficient (S_{11}) as a function of antenna to antenna top encasing distance d_{a-e} (mm) for d_{et} = 1 mm, b) antenna resonant frequency change for various thicknesses of the top encasing d_{et} (mm) for d_{a-e} = 4.5 mm.

observed for the flat water model, as are penetration depths of 21 mm for both scenarios with encasing. These values were calculated following the single antenna guidelines of ESHO[197]. When introducing the encasing around the reflector backed dipole antenna, the maximum SAR increased by 47% in a muscle equivalent phantom, from 3.4 W/kg to 5 W/kg for 1 W input power. The normalized 2D SAR distribution at 10 mm depth for the DiPRA module in the phantom is shown in Figure 5.5b. Figure 5.5c and Figure 5.5d show the normalized SAR profiles at 10 mm depth for all three studied scenarios along Y axis and Z axis, respectively. The encasing without the aperture cover had the best SAR symmetry from all three studied scenarios at 10 mm depth of the phantom. A 6 mm maximum SAR shift in -Y direction was observed for the DiPRA module.

5.3.2 DiPRA module verification measurements

Figure 5.6a shows the reflection coefficient comparison for the prediction and two measurements of the DiPRA. For all cases, S_{11} is below -20 dB, which represents maximum reflection of 1% from the input power. Figure 5.6b shows measured DiPRA resonant frequency as a function of top encasing thickness d_{et} (mm).
Normalized 1g SAR predictions and verification measurements for the DiPRA module without and with the 1 mm top cover are shown in Figure 5.7a and Figure 5.7b (without) and Figure 5.7c and Figure 5.7d (with). The distributions were normalized to the maximum SAR in the 2D plane at 12.8 mm phantom depth, i.e., the height of the first 3D printed frame filled with the agar phantom. For the DiPRA scenario without the top cover, we obtained comparable predicted (2.04 W/kg) and measured (2.09 W/kg) maximum SAR. For the scenario including a 1 mm top cover, the measured maximum SAR (2.41 W/kg) was higher than predicted (2.01 W/kg). In this case, measurement (Figure 5.7d) confirmed the predicted SAR shift when adding 1 mm top cover. Figure 5.8 shows the corresponding normalized SAR figures at 24.5 mm depth in the agar phantom. At this depth, predicted SAR is higher than measured SAR for both studied DiPRA scenarios.

5.3.3 MRcollar design

For 28 simulation setups we obtained a mean water bolus volume for the HYPERcollar3D of 8.0±0.3 l and 5.5±0.3 l for the MRcollar design. For 22 adjacent DiPRA modules inside the array and all 28 HTP setups, we obtained a cross-coupling of -23.6±5.1 dB. The maximum cross-coupling of -14.9 dB was observed for the two adjacent modules in the top left corner of the 2x3 array.

5.3.4 MRcollar model heating capabilities

Figure 5.9 shows the THQ for the MRcollar against the HYPERcollar3D model for 28 H&N patients. For the HYPERcollar3D a mean THQ = 1.25±0.39 was obtained, and 1.23±0.3 was the mean THQ for the MRcollar model, demonstrating comparable heating capabilities

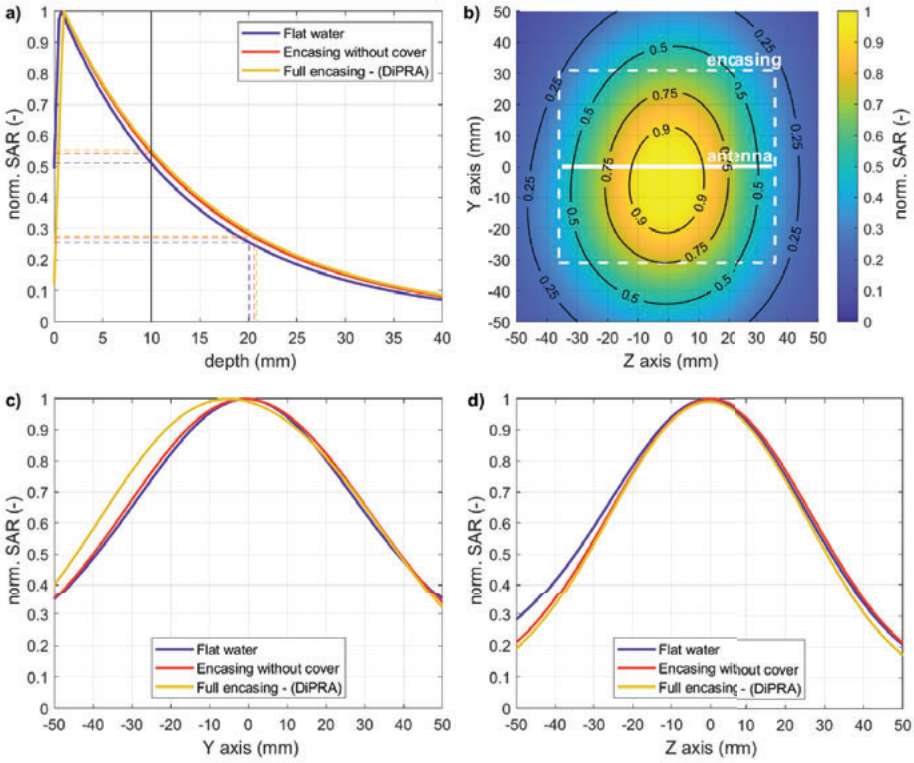

Figure 5.5: a) Normalized SAR depth profiles for reflector backed dipole antenna module in deionized water, in encasing without the cover part, and in full encasing, i.e., the DiPRA module, b) normalized 2D SAR profile at 10 mm depth of muscle equivalent phantom for the DiPRA module, highlighted in the figure using solid and dashed lines, c), d) normalized SAR profiles at 10 mm depth in the center along Y axis (Z=0 mm) and Z axis (Y=0 mm), respectively.

of both systems. Figure 5.10a and Figure 5.10b show the comparison of target coverage in terms of TC25 and TC50. Higher mean values for the MRcollar model of TC25 = 87.8±13% and TC50 = 55.5±23.8% in comparison to TC25 = 83.7±15.6% and TC50 = 47±22.1% obtained for the HYPERcollar3D demonstrate improved target coverage for the MRcollar design.

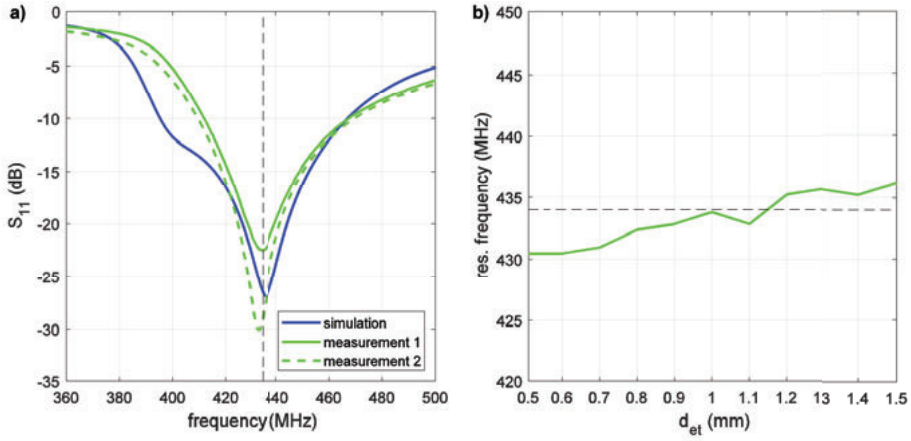

Figure 5.6: a) comparison of predicted and measured reflection coefficient for DiPRA with d_{et}=1 mm and d_{a-e}=4.5 mm, b) measured DiPRA resonant frequency change versus thickness of the top encasing d_{et} (mm)

5.3.5 MR assessment of antenna encasing - DiPRA module

Figure 5.11 shows the results for the magnitude images, the B_0 and flip angle (B_1^+) field maps in absence and presence of the DiPRA modules. The B_0 homogeneity in the absence of DiPRA modules had a standard deviation of 8.3 Hz within the ROI. The presence of two DiPRA modules improved B_0 field homogeneity (standard deviation = 7.9 Hz). The mean flip angle within the ROI was always 32.5±1.3° and hence independent of the presence of DiPRA modules. Finally, the image SNR in the ROI was 156 dB, when no DiPRA modules were present, while the image SNR was slightly higher when one or two DiPRAs were present (163 dB). Overall, a negligible impact on B_0 homogeneity, average flip angle and SNR were observed.

5.4 Discussion

The MRcollar design improves the predicted SAR target coverage (TC25 = +4.1% and TC50 = +8.5%) and achieves a comparable target-to-hotspot quotient (THQ = -1.6%) when comparing it to our clinically used HYPERcollar3D system. These improvements are present even though the MRcollar design has two antenna rings in comparison to three rings of HYPERcollar3D. The reflector backed dipole antenna shows an excellent predicted and measured matching, i.e., S_{11} < -20 dB, when placed in a specifically designed dielectric encasing. Cross-coupling between two adjacent antennas is predicted to be always better than -14.9 dB, ensuring independence of the individual channels. Encasing the DiPRA also improves

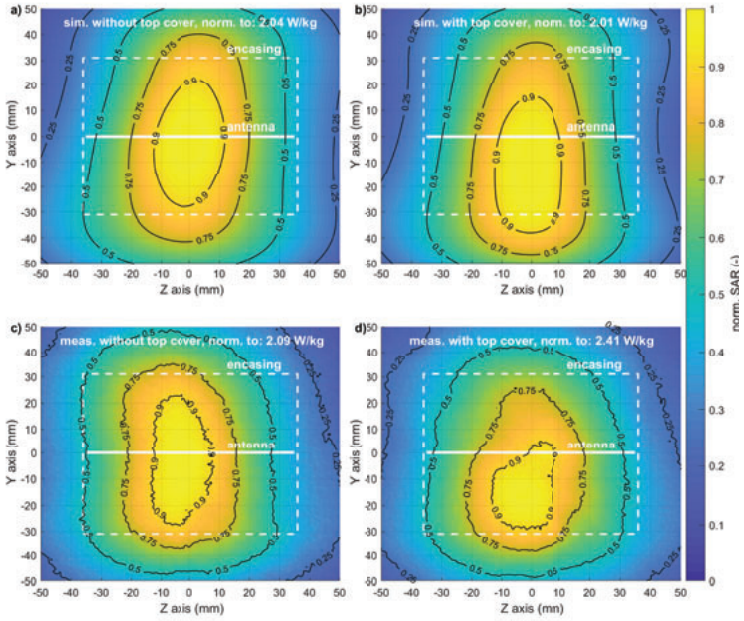

Figure 5.7: Normalized SAR predictions for DiPRA module a) with and b) without top cover, measurements c) with and d) without top cover at 12.8 mm phantom depth.

symmetry in the z-direction but adding the cover of the antenna encasing causes a 6 mm shift of the maximum SAR in 10 mm depth of muscle equivalent phantom. This predicted SAR shift when adding 1 mm top cover was verified using a dedicated measurement setup. It is caused by the y components of the electric field that are generated since the two dipole arms are on different sides of the PCB. This phenomenon is small but may impose a need to ensure a matching orientation of the antennas inside the Sim4Life model and the manufactured device. Unfortunately, the required technology to perform the ultimate experiment, i.e. microwave heating with the DiPRA modules while simultaneously measuring the temperature distribution using MR thermometry measurements, are presently not available. We are currently in the process of implementing additional 434MHz filtering in the MR signal readout pathway as well as obtaining sufficient 434 MHz amplifiers to enable the final proof of functionality and future clinical to apply hyperthermia using the MRcollar for patients with head and neck cancer. Nevertheless, the MR experiments reported here do illustrate that the DiPRA modules does not alter MR transmit/receive performance.

For the MRcollar design, we decided to replace the manually manufactured HYPERcollar3D patch antennas by reflector backed dipole antennas designed on a printed circuit board. A downside of this antenna is that very small FDTD grid steps, i.e., 0.75 mm and 0.5 mm, are

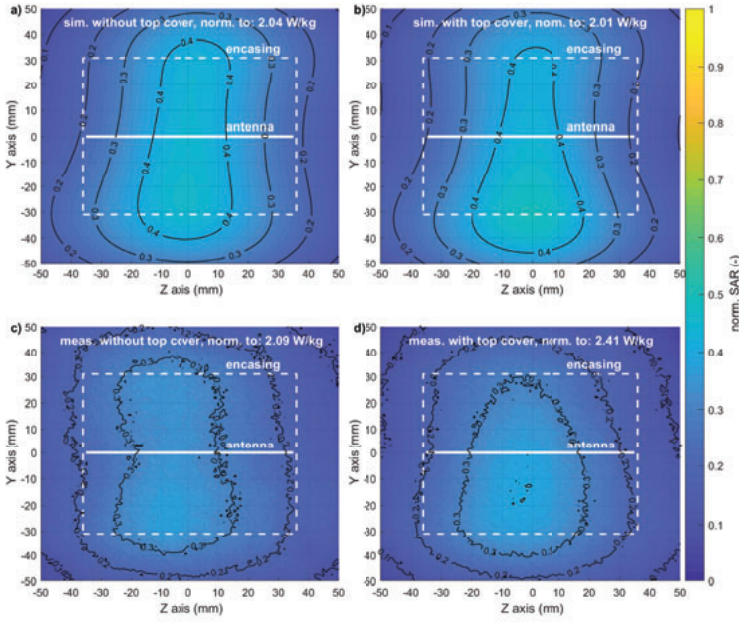

Figure 5.8: Normalized SAR predictions for DiPRA module a) with and b) without 1 mm top cover, measurements c) with and d) without top cover at 24.5 mm phantom depth.

necessary to correctly resolve the thin metallic antenna parts and the antenna feeding port. This increases the computation time for each simulation approximately two times in comparison to those for the HYPERcollar3D. However, we expect that ongoing improvements in graphical processor units will allow us to complete the whole treatment planning process in around two hours, which is sufficiently fast for clinical HTP modelling. Most importantly, the antenna orientation parallel to the radiated RF pulse of the MR birdcage coil indeed ensured a limited flip angle (B_1^+) distortion within the antenna encasing.

The maximum SAR of the single reflector backed dipole antenna module inside the muscle equivalent phantom was increased by 47% when introducing the encasing around the antenna, leading to higher power delivery at the target region. This will decrease the maximum power requirements for the microwave amplifiers, which is the most expensive sub-system in RF hyperthermia systems. The antenna encasings also reduce the amount of water needed in the system by 2.5 l (31%) in comparison to the HYPERcollar3D, making it lighter and thus easier to install. The DiPRA modules also enable an independent water circulation system for the antennas from the water bolus circulation system. In this way, the temperature inside the antenna cavities can be kept constant while the temperature in the water bolus

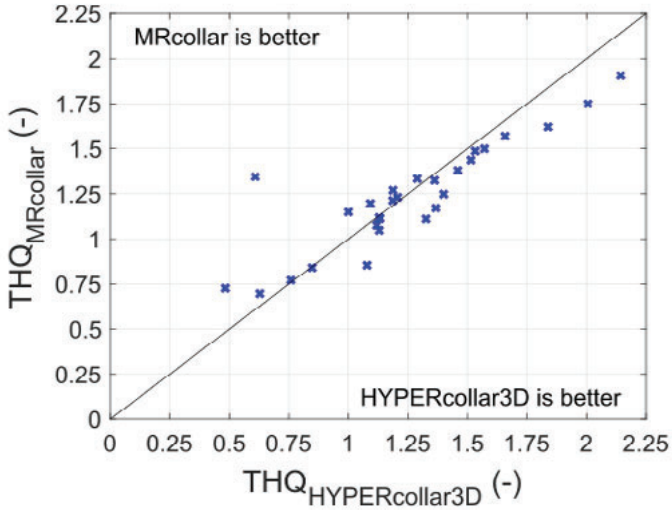

Figure 5.9: THQ comparison for the MRcollar and the HYPERcollar3D models for 28 H&N patients.

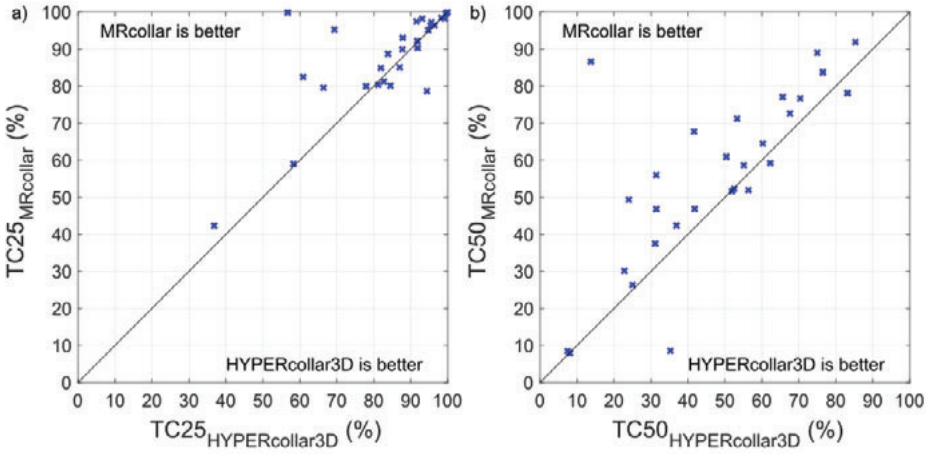

Figure 5.10: a) TC25 and b) TC50 comparisons of the MRcollar and the HYPERcollar3D models for 28 H&N patients.

can be tailored to the superficial cooling required. When changing the water temperature by 1 °C, the resonant frequencies for the patch and waveguide antennas shift by 1.1 MHz and

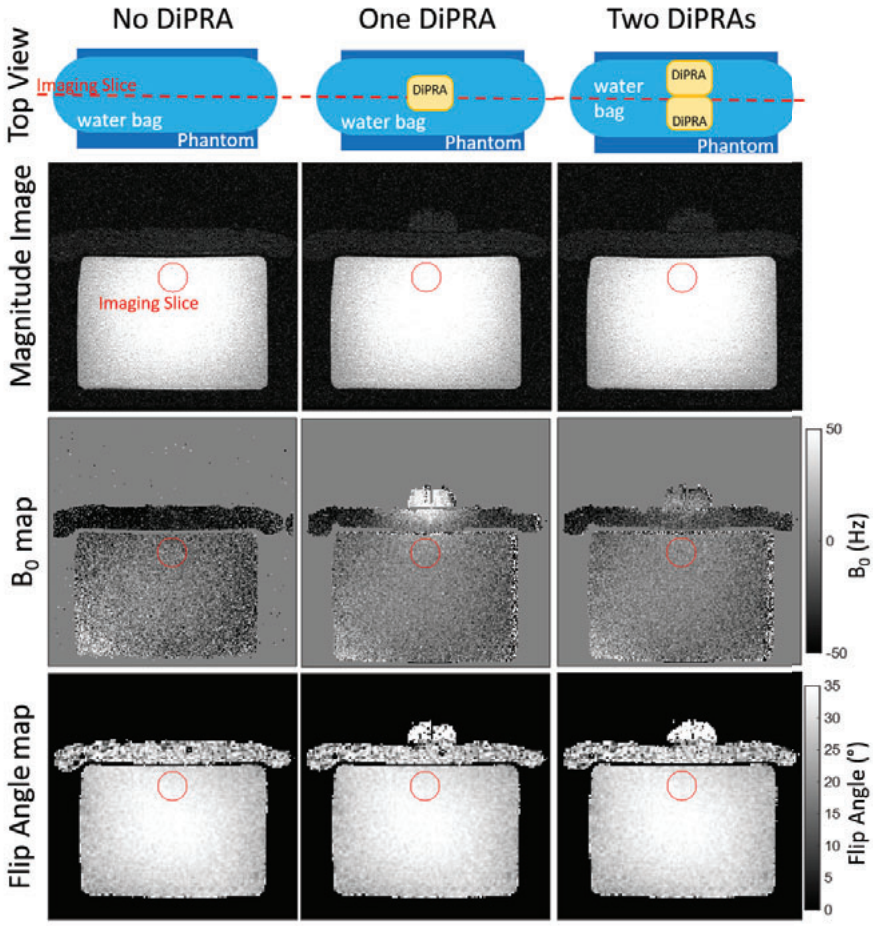

Figure 5.11: Results of the B_0, flip angle (mean value) and SNR measurements for the MR functionality assessment. The region of interest (ROI) is highlighted in red.

by 0.89 MHz respectively[202,203]. A lower water volume will also reduce water circulation-based MR distortions. In addition, the space between the DiPRA modules allows integration of an MR surface coil array close to the patient surface[204]. Such a surface coil array will increase imaging SNR and potentially enable multi-coil acceleration techniques to obtain MR thermometry maps with higher temporal resolution. With these combined approaches, the accuracy and motion-robustness of MR thermometry in RF hyperthermia treatments is

expected to improve.

5.5 Conclusion

Our results show that the novel MRcollar design enables achieving comparable heating capabilities as compared to the current clinical HYPERcollar3D. The DiPRA antenna module provides excellent predictive and measured matching characteristics and also predicted cross-coupling between adjacent antennas is predicted to be always better than -14.9 dB. The MRcollar design also reduces the amount of water needed by 31% (2.5 L), which will reduce applicator weight and water circulation-based MR distortion. The flip angle map distortions caused by the DiPRA module are found to be restricted to within the module itself. The H&N hyperthermia delivery quality with the MRcollar can be maintained, while facilitating simultaneous non-invasive MR thermometry for treatment monitoring and control.

CHAPTER 6

Experimental assessment of the MRcollar

This chapter is based on:
K Sumser, T Drizdal, GG Bellizzi, GC van Rhoon, JA Hernandez-Tamames, MM Paulides, Experimental Validation of an MR-Compatible Head and Neck Hyperthermia Applicator. *Int J Hyperthermia* in preparation.

Abstract

Clinical effectiveness of hyperthermia treatments can be hampered by lack of temperature monitoring and accurate temperature dosimetry. The desire for non-invasive temperature monitoring in head and neck region and the potential of MR thermometry prompt us designing an MR compatible hyperthermia applicator for head and neck region. In this work, we validate the design and numerical model of the MRcollar. Through reflection and cross coupling measurements, we showed that the MRcollar system has satisfactory and robust matching characteristics and low interaction between the individual antenna modules. Heating and focusing capabilities were measured in muscle equivalent phantom heating experiments. Heating requirements as required by the European Society for Hyperthermic Oncology were easily reached (6 °C increase in 2 minutes). The predicted and experimentally measured SAR patterns have a good match (≈95%). The MRcollar was shown to have minimal effect on the image quality in the clinical relevant part of the field of view. However, the water bolus reduces B_1 efficiency and consequently the SNR. Overall, the MRcollar design has been experimentally validated and the MRcollar has great potential to improve hyperthermia delivery in the head and neck region.

6.1 Introduction

Clinical studies have shown that hyperthermia increases the effectiveness of radiotherapy and chemotherapy for various anatomical sites, without inducing significant side effects[65–67]. Also for cancers of the head and neck (H&N), this adjuvant effect of hyperthermia on radiotherapy was shown[32,42,149]. To extend the application of hyperthermia from superficial regions also to deeply located target regions, we developed the HYPERcollar in 2007[205], which was succeeded by the HYPERcollar3D in 2014[43,44]. These devices were specifically developed for conformal heating of large target regions ranging from 4 to 15 cm of an advanced H&N disease[45]. Placement of invasive temperature catheters is challenging in the H&N region and provides temperature information from a limited number of discrete measurement points. Non-invasive temperature monitoring by Magnetic Resonance (MR) Thermometry (MRT) has shown clinical potential for obtaining detailed 3D temperature information from the region of interest[77]. Based on our extensive experience with model-based design from the development of the HYPERcollar and HYPERcollar3D, we designed the worlds-first MR compatible radio frequency (RF) hyperthermia applicator for the H&N: the MRcollar[206]. This novel design is based on a radically new antenna element and array concept. However it still requires validation of the heating characteristics and MR compatibility necessary for its introduction into clinical practice.

The HYPERcollar3D was designed in order to improve heating of the target region, and to reduce modeling errors, such as a more reproducible water bolus shape, for improving the translation of hyperthermia treatment planning (HTP) settings into the clinic. Based on these innovations, HTP has become a more reliable tool to ensure target conformal electromagnetic field energy delivery. However, even when energy delivery is homogeneous throughout the target region, the dramatic impact of patient, tissue and heating specific thermoregulation affects the true achieved temperature[154,207]. Therefore, this crucial but largely unquantified impact of thermoregulation, deteriorates the temperature prediction accuracy. Hence, detailed temperature measurements both in the target region and healthy tissues are required to assess the true temperatures achieved and to enable adapting the power distribution for maximizing the applied thermal dose. Non-invasive 3D temperature monitoring during H&N hyperthermia is therefore desperately needed for exploiting the focusing potential of the HYPERcollar3D and for achieving the full clinical potential of hyperthermia.

Literature indicates that the proton resonance frequency shift method, i.e., the most common MRT method, can provide 3D temperature maps with around 0.5 °C accuracy[208]. For H&N hyperthermia, several studies[107,130] have shown the feasibility of adopting MR compatible applicators; however, to date, none has been adopted in clinical practice. Recently, we proposed a novel MR compatible applicator for the H&N region: the MRcollar[206]. In this design, MR-transparent Yagi-Uda antennas[124] were combined with dielectric reflector modules (DiPRA) to minimize radiofrequency (RF) radiation towards adjacent antenna elements and towards the RF coil of the MR scanner. However, the applicator manufactured based on this design needs to be validated before its introduction in clinical practice.

The aim of this study was to experimentally validate the MRcollar design and the numerical model, as well as to validate the suitability of the DiPRA modules in a realistic MR-hyperthermia applicator environment. First, the electromagnetic design of the antennas and the array was validated by reflection and cross-coupling measurements. Second, the achievable heating rate of the device was measured using optical fiber temperature probes inserted into cylindrical and anthropomorphic phantoms. Third, focusing capabilities were measured in a muscle-equivalent cylindrical split-phantom by an infrared camera. Last, the impact of the MRcollar on MR imaging using the body coil of the MR scanner was studied by measuring the induced change in B_1^+ (flip angle maps) and Signal-to-noise Ratio (SNR). These steps allowed us to experimentally verify the feasibility of using the newly prototyped MRcollar for MR guided hyperthermia and assess the actual impact of the water bolus on imaging quality.

6.2 Materials and Methods

6.2.1 Mechanical Design

The MRcollar (shown in Figure 6.1) consists of two moon-shaped shells comprising of six antenna modules in a 2x3 arrangement placed around the H&N. Every module contains a printed Yagi-Uda antenna submerged in water and operating at 433.92 MHz. A water bolus, i.e. a bag of flexible foil filled with demineralized water, is placed between the antenna modules and the patient surface in order to improve coupling of electromagnetic waves and to prevent unwanted heating at the patient skin. The MRcollar position can freely adjusted in all three directions. Furthermore it can be rotated along z-axis (sagittal plane) for 15°, which is the preferred position for the tumors in larynx region. The base plate was designed to fit into the dedicated slot on the MR patient bed. Note that a water bolus design that is stable, comfortable, durable and flexible enough to conform to patients of different sizes is subject of ongoing study. For this experimental validation we therefore used a simple water bag as water bolus.

6.2.2 Phantoms

Two semi-cylindrical split phantoms (shown in Figure 6.2a) were made and filled with muscle-equivalent material consisting of deionized water, agar, sodium chloride, polyethylene powder and TX-151 (electrical conductivity 0.39 S/m, relative permittivity 59, thermal conductivity 0.6 W/m/°C, specific heat 3800 W/kg/°C). A patient-representative anthropomorphic H&N phantom (electrical conductivity 0.43 S/m, relative permittivity 60, thermal conductivity 0.6 W/m/°C, specific heat 3800 W/kg/°C; shown in Figure 6.2b) was made using the same mixture, but with the addition of $CuSO_4$ to modify the MR properties (T_1: 820 ms, T_2: 37 ms). Dielectric properties of the phantoms were measured using dielectric assessment kit (DAK-4, Speag, Zurich, Switzerland). Thermal properties of the phantoms

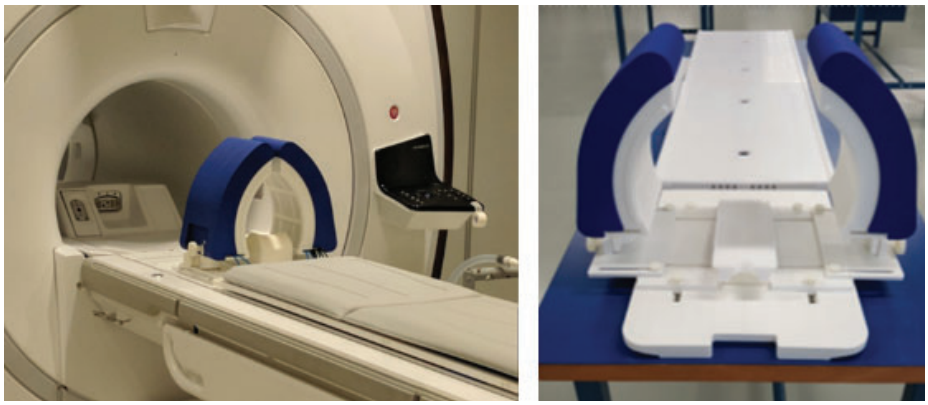

Figure 6.1: Picture of the MRcollar applicator prototype without the inner water bolus.

were measured using a thermal property analyzer (TEMPOS, METER Group, Inc., USA). The third phantom (T_1: 108 ms, T_2: 96 ms; shown in Figure 6.2c) was provided by the MR vendor.

6.2.3 Antenna Characterization Measurements, Heating and Focusing Steering Capabilities

We measured the complete S-matrix by attaching a network vector analyzer (ZNC 3, Rhode & Schwarz, Germany) to the antennas using the cylindrical split phantom as a load.

For the heating characterization measurements, the split phantom was used. MR images of the setup consisting of applicator, water bag and phantom were acquired before the heating experiment to correctly capture specifically the irregular shape of the water bag. Then the images of the phantom and the water bolus were manually segmented using iSeg. The

Figure 6.2: Phantoms (a) Cylindrical Split Phantom (b) Cylindrical MR phantom, (c) H&N phantom

segmented models were manually overlaid with the MRcollar numerical model. Electromagnetic field distributions were computed per antenna channel using Sim4Life (v.4.4.1.3808, Zurich MedTech, Zurich, Switzerland). A 433.92 MHz excitation harmonic signal was applied for 20 periods to each antenna. The size of the calculation domain was 43 million voxels, with a maximum voxels size of 1.5x1.5x1.5 mm^3. Three heat focus locations were selected, i.e. central focus (0,0,0) mm, x-steered (20,0,0) mm, z-steered (0,0,40) mm, and the corresponding amplitude and phase per channel were calculated using Time-reversal method[209]. The phantom was heated for 180 seconds with total input power of 180 W. Temperature was monitored during the heating process by 27 fiber optic temperature probes (FISO FOT-NS-577E, Fiso, Quebec, Canada). Specific absorption rate (SAR) was then calculated by the temperature increase in the first 60 seconds. The temperature distribution of the split phantom was imaged with an infrared camera before and, quickly (≈10 seconds) after opening both halves, after the heating session. Then the differential temperature distribution was calculated from these images and scaled to SAR distributions by multiplying the temperature difference with the specific heat ratio and dividing by heating duration. Heating focus-size was defined as the length and the width of the 50% iso-SAR contour. The measurements were repeated to test for reproducibility. Forwarded amplitude and phase, as well as reflected power, were continuously monitored using the clinical measurement setup[210].

We quantified the match between the measurements and the numerical model using the Gamma-method[211]. The tolerances were defined for dose difference as 10% and distance to agreement as 10 mm. The analysis was done using all voxels absorbing at least 30% of the maximum measured SAR in the phantom, to exclude the voxels heated due to thermal conduction.

6.2.4 MR compatibility Measurements

The H&N phantom and cylindrical phantom were used to evaluate the MR-compatibility in three different setups:

- Setup 1 - Phantom only: without the MRcollar present in the scanner but at an equal reference height, measured from the bottom of the MR bed.
- Setup 2 - MRcollar-WB: MRcollar present without a water bolus; to investigate the impact of the metallic structures (such as connectors and copper antenna parts).
- Setup 3 - MRcollar: MRcollar with the waterbag between the shells and the phantom; to investigate the additional impact of the water bolus.
- SNR scans: two spoiled gradient echo acquisitions (with and without excitation RF pulse) with the following parameters: slice thickness 2 mm, slice spacing 22 mm, 10 slices, FOV 500x500 mm^2, matrix 256x256, TR/TE 75/4.5 ms, NEX 1. Flip angles were chosen according to Ernst angle relation; 24° for Phantom 2 and 60° for Phantom 3.

- B_1^+ maps: Bloch-Siegert sequence with slice thickness 10 mm, slice spacing 22 mm, 10 slices, FOV 500x500 mm^2, matrix 128x128, TR/TE 19/13.4 ms, NEX 1, flip angle 30°. Transmit gain and shimming were kept constant across scans. A region of interest (ROI) was defined to calculate the mean SNR and flip angle values. The same ROI was used for both phantoms and the change in SNR for Setup 2 and 3 is given relative to Setup 1.

6.3 Results

6.3.1 Reflection and cross-coupling measurements

The complete S-matrix of the MRcollar system is shown in Figure 6.3. The primary reflection coefficient (S_{ii}) of all antennas was on average below the design goal of -15 dB (mean ± standard deviation = -17 ± 6 dB) and the cross-coupling between the antennas (S_{ij}) was less than -20 dB for all except four combinations (mean ± standard deviation = -32 ± 7dB).

6.3.2 Heating, Steering Capabilities and Focus-Size

Using 180 W total input power for 180 seconds, 10.3±0.19 °C temperature increase was achieved for all three optimization settings. The maximum measured SAR was 240 and 235 W/kg for central steering, 224 and 221 W/kg for x-steering, and 224 and 227 W/kg for z-steering. The heating patterns for these three different focus locations are shown in Figure

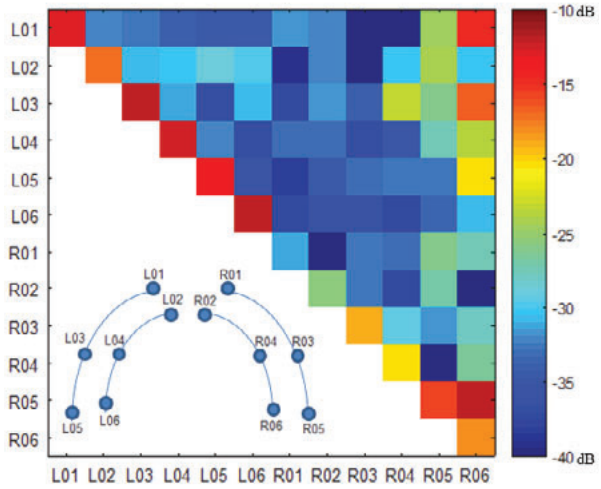

Figure 6.3: S-matrix and a schematic showing the antenna locations using fish-eye perspective for clarity

6.4. The length and width of the focus was 82 and 30 mm for central steering, 85 and 32 mm for z-steering, and 83 and 33 mm for x-steering. The gamma criteria was full-filled by 88% of the voxels for central steering, 98% for z-steering, and 99.0% for x-steering.

6.3.3 MR Compatibility Measurements

Figure 6.5 shows the example magnitude images from Setup 1 and 3 for both phantoms. There is no qualitative drop in image quality. Figure 6.6 show the normalized change in the SNR for Phantom 3 and Phantom 2, respectively. The presence of the MRcollar without the water bolus did not alter SNR for both setups. On the other hand, inclusion of water bolus

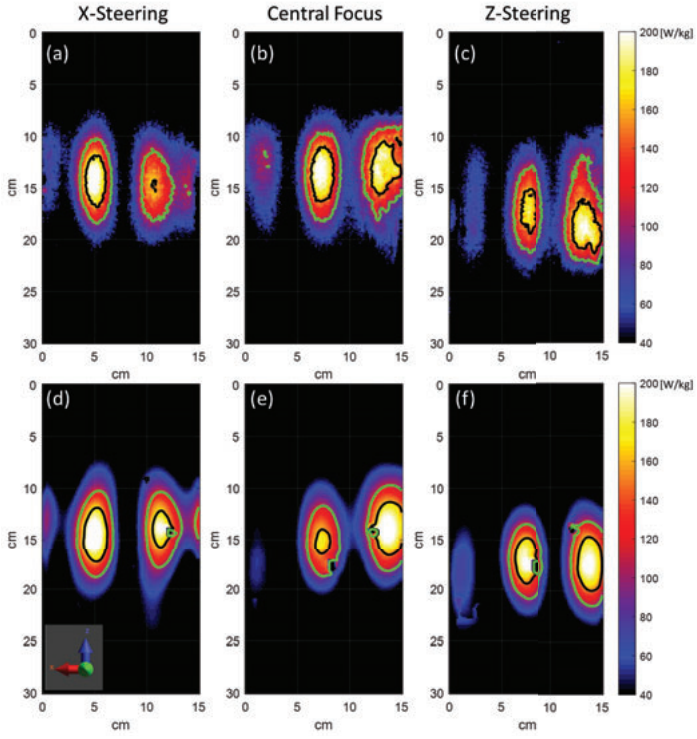

Figure 6.4: Simulated and measured temperature distribution. Measurements: (a) Heating Focus shifted 2 cm from the center in x-direction (b) Central Heating Focus (c) Heating Focus shifted 4 cm from the center in z-direction. Simulation Results: (d) Heating Focus shifted 2 cm from the center in x-direction (e) Simulated Central Heating Focus (f) Heating Focus shifted 4 cm from the center in z-direction

caused a reduction in SNR, especially in the first three slices.

Table 6.1 presents the mean flip angle values and the standard deviation in each setup. Inclusion of the MRcollar increased the flip angle values but homogeneity was unaffected. In Setup 3, a smaller flip angle than prescribed was received by the first three slices. In the isocenter, nominal flip angle was achieved in both cases.

6.4 Discussion

In this study, we experimentally validated the MRcollar prototype and its numerical model. In this regards, the antennas return loss and cross coupling were measured to fulfill the design requirements. Good heating performance predicted by the simulations was validated using Gamma-method in three distinct phantom experiments. The MRcollar MR scanner interaction tests confirmed that the MRcollar has minimal effect on image quality, SNR, and B_1 field homogeneity, thereby proving that the MRcollar is MR compatible.

6.4.1 EM compatibility

The DiPRA modules satisfied the original reflection characteristic requirements on average (S_{11} < -15dB) set for the original single Yagi-Uda antenna by Paulides et al.[124]. The measured cross coupling between the DiPRA modules showed overall good performance (S_{12} <-28 ± 8 dB) and matched the predicted performance by the simulations (S_{12} = -27 dB[206]).

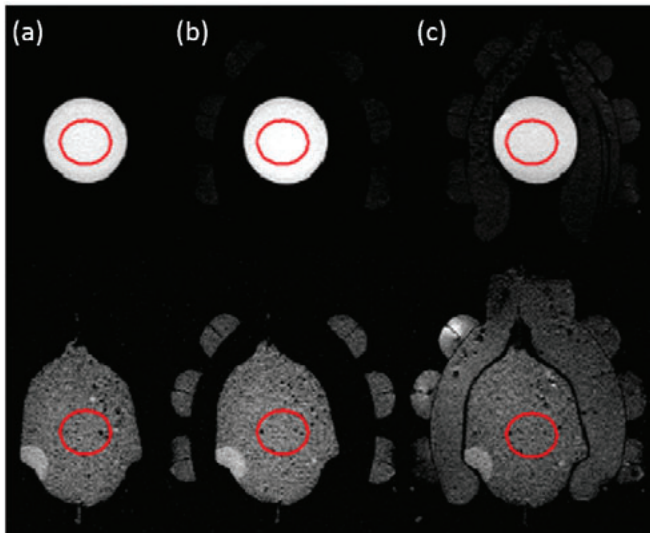

Figure 6.5: MR magnitude images (a) Phantom only (b) MRcollar-WB (c) MRcollar

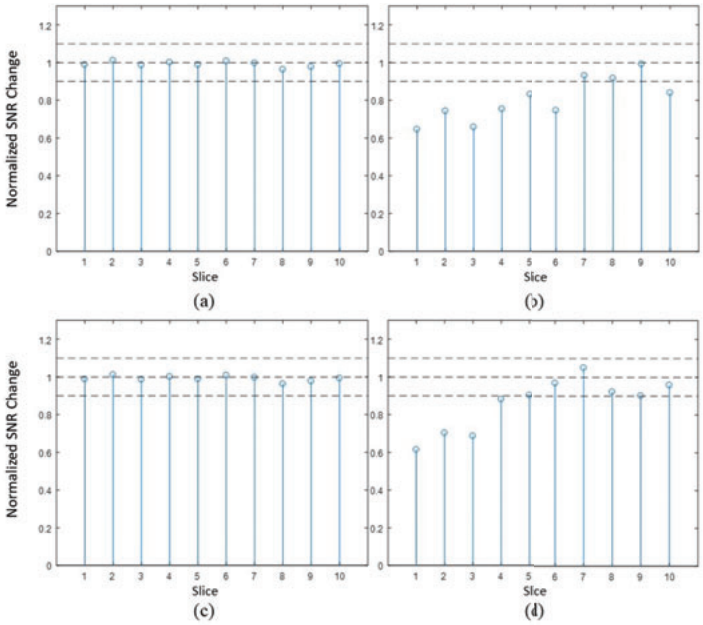

Figure 6.6: Relative change SNR compared to Phantom only for (a) Phantom 3 MRcollar-WB (b) Phantom 3 - MRcollar (c) Phantom 2 - Setup 2 (d) Phantom 2 - Setup 3. Dashed lines indicate +10% cutoffs.

6.4.2 Heating Capabilities

The capabilities of the MRcollar prototype to focus and steer the heating pattern were tested using the same tests as in Paulides et al.[108] for the HYPERcollar. However, because of the patient conformal shape of the MRcollar prototype, we used the time reversal focusing technique[209] to determine the phase and amplitude coefficients driving the applicator to achieve the desired steering. The measured focus size in the three different configurations (length 83 mm, width 31 mm), is in agreement with what was experimentally found (length 87-112 mm, width 35 mm in[108]) and what was described in literature[212,213]. The use of the time reversal technique indeed resulted in central and steered foci. Hence, we did not use a more sophisticated optimization approach[52,214–217], which would intrinsically require a target volume and constraints that would only blur the focusing ability in this first validation step.

In the absence of temperature rise criteria for deep hyperthermia applicators, we used those defined in the recent quality assurance document for superficial hyperthermia applicators: at least a 6 °C temperature increase in a maximum of 6 minutes[197]. The MRcollar fulfilled the above criteria in less than two minutes, i.e. around 70% less than prescribed. Moreover,

Table 6.1: Mean and standard deviation of flip angle in the ROI

	Flip angle (°) - phantom 1			Flip angle (°) - phantom 2		
Slice	Setup 1	Setup 2	Setup 3	Setup 1	Setup 2	Setup 3
1	27.4±0.5	30.3±0.3	20.6±0.8	27.5±3.0	28.0±2.6	20.1±5.0
2	29.6±0.4	32.6±0.4	23.7±0.4	28.0±2.9	29.9±2.9	21.4±5.0
3	30.9±0.4	34.0±0.4	26.4±0.9	28.7±5.1	31.6±2.1	21.5±5.9
4	31.2±0.4	34.8±0.4	29.0±0.4	31.1±2.6	33.5±2.8	24.9±4.1
5	31.6±0,4	34.5±0.5	30.6±0.6	32.0±2.5	34.6±2.4	28.7±3.1
6	31.6±0.5	33.9±0.5	31.1±0.5	32.2±2.5	34.4±2.2	30.7±2.4
7	31.0±0.4	33.1±0.6	30.6±0.5	32.0±2.1	33.5±2.3	31.1±2.8
8	30.2±0.4	31.6±0.5	29.6±0.5	30.3±2.4	30.7±2.6	29.9±3.3
9	28.7±0.4	29.4±0.5	27.9±0.5	28.3±2.6	27.0±2.6	28.8±3.6
10	26.3±0.4	26.4±0.5	25.6±0.6	25.2±2.8	27.3±7.4	25.8±3.7

the total input power used in this study was only 10% of the available power of the clinical amplifiers. Note, however, that the head and neck region is prone to a very high thermoregulation and that smaller heat foci require more energy[218]. Therefore the true heating capabilities of the MRcollar in patients is still required.

Gamma analysis resulted in a good match (95%) between the predicted and experimentally measured SAR patterns for all three different focus settings. In all three cases, the discrepancies where near the edges of the phantom but far from the focus region. The differences can be explained by changes in the shape of the water bag between the experimental setup and the simulated shape. Still, further research needs to be done to reduce the discrepancy.

6.4.3 MR compatibility

Our MR compatibility measurements of the MRcollar show that the metallic parts contained in the antenna structures have a minimal effect on the image quality in the phantoms, i.e. the clinically relevant part of the field of view. The susceptibility artefacts induced by the metallic parts were contained in the antenna cavities. SNR values remain in the same range before and after the MRcollar is inserted into the MR scanner bore. Only a small increase (≈1.5°) was measured in the flip angle maps. The low standard deviation in the flip angle maps confirms the homogeneity of the field. This result confirms the earlier experimental findings that neither the Yagi-Uda antenna[124] nor the DiPRA model used in this study affect MRI scans. The effect of the water bolus was found to be much stronger than that of the metallic parts of the device. After the addition of the water bolus, the flip angle level was measured to be lower than the one prescribed. Additionally, the signal level dropped due to less excitation of the magnetization vector, especially in the first three slices. This drop can be explained by energy losses in the water bolus. Even though the measured flip angle was lower than the prescribed flip angle, the homogeneity of the flip angle maps (std ≈0.45°)

was not affected. As a result, the loss in SNR can be counteracted by a proper B_1 shimming, an adjustment of the transmit gain, or both.

6.5 Conclusion

In this study, we introduce the MRcollar; worlds-first MR compatible RF hyperthermia applicator for the head and neck; and validated its design and operation. Antenna characteristics were measured satisfactory and the heating rate requirements set by ESHO were satisfied. The measurements and the predicted distributions had a good agreement; 95% of the voxels satisfied the agreement criteria. The MRcollar had minimal effect on MR image quality. ${B_1}^+$ field homogeneity were unaffected by the metallic structures contained in the antennas.

Part III: New hardware Avenues

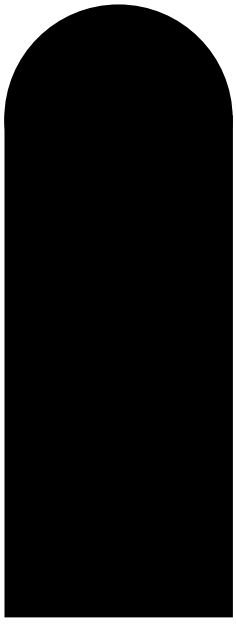

CHAPTER 7

Improving MR thermometry by optimizing waterbolus filling

This chapter is based on:
K Sumser, GG Bellizzi, GC van Rhoon, MM Paulides. The Potential of Adjusting Water Bolus Liquid Properties for Economic and Precise MR Thermometry Guided Radiofrequency Hyperthermia. Sensors. 2020 Jan;20(10):2946.

Abstract

The potential of MR thermometry (MRT) fostered the development of MRI compatible radiofrequency (RF) hyperthermia devices. Such device integration creates major technological challenges and a crucial point for image quality is the water bolus (WB). The WB is located between the patient body and external sources to both couple electromagnetic energy and to cool the patient skin. However, the WB causes MRT errors and unnecessarily large field of view. In this work, we studied making the WB MRI transparent by an optimal concentration of compounds capable of modifying T_2 relaxation without an impact on the efficiency of RF heating. Three different T_2* reducing compounds were investigated, namely $CuSO_4$, $MnCl_2$, and Fe_3O_4. First, electromagnetic properties and T_2* relaxation rates at 1.5 T were measured. Next, through multi-physics simulations, the predicted effect on the RF-power deposition pattern was evaluated and MRT precision was experimentally assessed. Our results identified 5 mM Fe_3O_4 solution as optimal since it does not alter the RF-power level needed and improved MRT precision from 0.39 °C to 0.09 °C. $MnCl_2$ showed a similar MRT improvement, but caused unacceptable RF-power losses. We conclude that adding Fe_3O_4 has significant potential to improve RF hyperthermia treatment monitoring under MR guidance.*

7.1 Introduction

Clinical trials have shown that the clinical outcome and local control of chemotherapy and radiotherapy treatments can be enhanced with the addition of hyperthermia treatments[18,65,72,73,150]. Clinically demonstrated thermal dose effect relationship indicate that the efficacy of the hyperthermia treatment improves when achieving higher temperatures in the 40–44 °C range in the entire target, while preventing unacceptable temperature increases in healthy tissues, i.e., "hotspots". Advances in hyperthermia technologies improved the delivery of the treatment[43,215,219]. Electromagnetic radiofrequency systems consists of multiple antennas organized in an annular array configuration and using constructive interference provides focused energy deposition at depth, whereby the location of the focus can be dynamical adapted using phase and amplitude control per antenna[15,39]. For deep pelvic heating, the frequency range is 70–120 MHz, for deep heating of head and neck tumors the frequency range is 400–600 MHz. A multi-functional water bolus is used to reduce the antenna size, cool the skin and obtain a preferential energy transfer to the tissue. These advanced heating systems are clinical applied in combination with hyperthermia treatment planning guided focus steering. However, the inhomogeneous, variable and subject dependent thermoregulation mechanisms make that real-time temperature monitoring is required for optimal guidance of the heating adaptations. Magnetic resonance thermometry (MRT) provides a non-invasive way to map relative temperature change pattern in the regions of interest[78,220]. The need for non-invasive temperature monitoring and the potential of MRT fostered the development of novel magnetic resonance imaging (MRI) compatible hyperthermia applicators[192]. Such integration of a hyperthermia device into an MR scanner is not a trivial task and is accompanied by additional requirements and needs for these hybrid devices[61,103,129]. One of the issues that arise is caused by the hyperthermia devices water bolus (WB). While the WB is a trivial component in non-MRI compatible hyperthermia applicators, it causes an unnecessary increase in the imaging field of view, creates flow artifacts and skews pre-scan calibrations, resulting in temperature errors and a longer scan time[15]. Solving these WB induced issues may form a large step towards reaching the full potential of MRI guided hyperthermia treatments, but our knowledge on the optimum WB filling is incomplete.

The WB is a fluid filled flexible "bag" that can conform to the skin and covers the space between antennas and patient. De-ionized, i.e., demineralized, water is usually used as filling material due to its large availability, high biocompatibility, and low losses. The WB has a pivotal role in a radiofrequency (RF) hyperthermia applicator. The water matches the dielectric properties of the patient better and thus enables efficient transfer of the radiofrequency waves from the devices antennas into the patient. The water is circulated to cool so called "hotspots", i.e., locations with high power absorption that often occur near the patients skin. Water as a fluid also easily follows the body contour which is essential for impedance matching and surface cooling. It can also be used to cool the antennas. The water is also applied to reduce the effective dielectric value of the medium surrounding the antennas, which decreases the resonant antenna size considerably and enables including more

antennas in the applicator[202]. Unfortunately, the water also comes at a cost when used for MR guided hyperthermia. Hydrogen in water is the main source of MRI signal in the patient and the imaging field of view needs to cover also the WB to prevent aliasing in the MR image. Also, pre-MRI-scan calibrations and MRI RF (B_1) field shaping are distorted since also the signal in the large WB is optimized by these automatic routines. Moreover, water circulation results in flow artifacts in the differential MRT images. It would be ideal if these problems could be avoided by a WB that is (nearly) invisible to MRI while preserving its benefits for hyperthermia, i.e., keeping the desired matching and cooling characteristics.

WB MRI invisibility can be reached by several methods. A simple solution can be achieved by using heavy water (deuterium oxide, $D_2O = {}^2H_2O$) instead of demineralized water (H_2O). Heavy water is invisible in ^{1}H MRI while having the same electromagnetic properties 18. However, the required volume to fill a typical WB is large and heavy water is very expensive. Another method is by altering the MRI method by inversion recovery (IR) techniques, which are widely used in MRI applications to suppress water or fat signal. Using an IR sequence to suppress the signal from the WB, however, this will also suppress the water signal in the body that is used to measure the proton resonance shift in MRT. Another way to selectively suppress the WB signal is by selective excitation of the region of interest using two dimensional RF pulses[221]. Grissom et al. recently showed that two dimensional RF pulses can be used to reduce temperature errors related to the water bath and water bath motion for transcranial MRguided focused ultrasound (MRgFUS) ablation. They reported on average 43% improvement in temperature precision[222]. While this technique shows promise, it is spatially limited to a single dimension.

While the previous methods (D_2O, IR and spatial selective pulses) utilized modification of the longitudinal relaxation (T_1), we hypothesized that modification of the transverse relaxation (T_2 or T_2* for gradient echo sequences) of water signal can be an easier, cheaper and more feasible solution. Several studies have exploited contrast agents to reduce the WB T_2* relaxation time. Manganese chloride ($MnCl_2$) was used by Delannoy et al.[103] for hyperthermia and Chopra et al.[223] for MR guided high intensity focused ultrasound (HIFU). Allen et al. have proposed the use of suspending iron oxide nanoparticles (SPIO) to suppress water bath signal for MRgFUS surgery and reported that SPIO doped water weakly attenuates acoustic waves[224]. Although these studies showed promising results, no data are available on their effect on electromagnetic material properties, which are pivotal for efficient MR guided RF hyperthermia. Also, the effect of additives to the water on therapy and the optimal concentration or compound has never been researched.

In this study, we investigated the benefit of T_2* reducing additives in terms of MRI signal reduction while maintaining RF properties for different solutions aimed at their application in the WB during MRI guided RF hyperthermia treatments. Water solutions were prepared with compounds that are known for their T_2* reducing properties; $CuSO_4$, $MnCl_2$, and Fe_3O_4. We measured electromagnetic properties 50–600 MHz range and T_2* relaxation rates at 1.5 T. Through multi-physics simulations, we evaluated the predicted effect on the power deposition pattern when the WB filling electromagnetic properties changed to the measured ones for two MR compatible hyperthermia applicators. Further, we identified the compounds

and concentrations that fulfill the criteria for power efficiency, power deposition patterns and MR images. Finally, the suitable solutions were experimentally tested in a clinical setup of the prototype MRcollar[110] and their effect on MRT precision were assessed.

7.2 Materials and Methods

7.2.1 Requirements for the Water Bolus Fluid

An ideal WB for MRI guided hyperthermia treatments should have similar electromagnetic properties as deionized water while producing no or limited MRI signal and artifacts. Demineralized water filled WB are generally used because of its low losses at the working frequency of hyperthermia applicators, e.g., at 434 MHz the electrical conductivity is equal to 0.04 S/m. Increase in conductivity results in an increase of the power needed to achieve a therapeutic specific absorption rate (SAR) level within the tumor. At Erasmus MC, available amplifiers can provide maximum of 1800 W of RF power. Hence total required power should be below the maximum available power. However, the ideal WB solution should be energy efficient and should not cause a drastic power requirements. The requirements for MRI invisible WB can be achieved when the signal-to-noise ratio (SNR) level of the WB signal drops to 1. Currently in our clinic, dual echo gradient echo sequence with the body coil utilized for receiver has been used for MRT with echo times 4.8 ms and 19.1 ms[99]. Hence, for our setup, we desire SNR of the WB signal should be 1 at the echo time 4.8 ms. Since this will ensure the SNR at echo times longer than 4.8 ms to be 1 as well.

7.2.2 Preparation of the Samples

Three different compounds were selected[103,223,224] that are used to modify T_2; $CuSO_4$ (Stock# 102791, Merck KGaA, Darmstadt, Germany), $MnCl_2$ (Stock# 244589, Merck KGaA, Darmstadt, Germany), and Fe_3O_4 (Stock# US7568, US-Nano-Research, Houston, TX, USA). Six different concentrations for each compound were selected: [50, 100, 250, 500, 1000, 1250 mM] for $CuSO_4$, [0.5, 1, 2.5, 5, 12.5, 25 mM] for $MnCl_2$, and [0.25, 0.5, 1, 2.5, 5, 10 mM] for Fe_3O_4. The temperature of the water bolus during treatment range from 20 to 30 °C. The EM and MRI properties in this range is relatively stable and changes less than 1%[225,226]. Therefore, all the measurements were made at 21 °C, at the room temperature. The solutions were prepared by diluting the compounds with demineralized water. The samples were stored in 200 mL measurement cups (diameter 60 mm, height 85 mm).

7.2.3 MR Relaxometry Measurements

T_2* relaxation times of $CuSO_4$, $MnCl_2$, and Fe_3O_4 solutions for 1.5 T were measured using a 450w MR scanner (GE Healthcare, Waukesha, WI, USA) at 21 °C. Data acquisition was made with a multi echo gradient echo sequence with the following sequence parameters: TR = 300 ms, TE = [1.3, 2.8, 4.3, 5.8, 7.3, 8.8, 10.3, 11.8, 13.3, 14.8, 16.3 ms], FOV = 360

mm, NEX = 2, Slice Thickness = 10 mm, Flip Angle = 40°. The T_2* relaxation rates were calculated by fitting a mono-exponential signal decay model[227] using the nonlinear curve fitting function lsqcurvefit of Matlab (R2018b, The MathWorks Inc., Natick, MA, USA). For each sample, a region of interest was chosen manually.

7.2.4 Electromagnetic Property Measurements

The electrical conductivity (σ [S/m]) and relative permittivity (ϵ) were measured with open-ended coaxial probe DAK-12 (v2.4; SPEAG, Zurich, Switzerland) with a ZNC3 vector network analyzer (Rhode & Schwarz, Munich, Germany). The system calibration was performed using the open and short, and demineralized water at room temperature as load. The samples were placed in 200 mL measurement caps (diameter 60 mm, height 85 mm) and measured 8 times in the frequency range of 50–600 MHz with 1 MHz steps at 21 °C. The VNA was recalibrated before each measurement.

7.2.5 Effects on Power Deposition Pattern

The effect of the change in the electromagnetic properties of the WB were evaluated for two MR compatible hyperthermia applicators: the Sigma Eye applicator of the BSD2000-3D-MRI system (PYREXAR Medical, West Valley City, Utah) 28 and our in-house developed MR-compatible head and neck hyperthermia applicator (MRcollar)[110]. The Sigma Eye consists of 12 dipole antenna pairs operating at 100 MHz and this device is used for deep loco-regional hyperthermia treatments in pelvis region. The WB of this applicator encloses the abdominal region of the patient in treatment configuration. The MRcollar is a twelve-channel applicator and consists of two moon-shaped halves. Modified Yagi-Uda antennas operating at 434 MHz are employed in this applicator[124]. Hyperthermia treatment planning was performed for these applicators for models of two patients that were treated with pelvis or head and neck hyperthermia, respectively. In our simulations, the electromagnetic properties of the WB were changed to those measured for the different solutions. Electromagnetic field distributions were computed per antenna using Sim4Life (v.5.0.1, Zurich MedTech, Zurich, Switzerland) and normalized to 1W radiated power. Then, the field was optimized using Matlab-based in-house developed adaptive hyperthermia tool VEDO[52]. The effect on the power deposition patterns were evaluated using hyperthermia treatment planning (HTP) parameters target-to-hotspot quotient (THQ) and the target coverage of the 50% iso-SAR volume (TC50)[228,229]. To calculate the effect on power efficiency, total input power was increased until the maximum predicted temperature in the healthy tissue reached 44 °C. This power was then used to compare the effect of the change in measured dielectric property for each solution on power efficiency, i.e., heat loss in the WB.

7.2.6 Effects on MRT Precision

The samples that satisfied the requirements were tested in a representative treatment setup using the MRcollar. The other MR compatible applicator available in Erasmus MC the Sigma

Eye applicator is in clinical use and the WB cannot be instantly changed, whereas the MR-collar is an experimental prototype and has exchangeable WB. The WB of the right MRcollar shell was used to test the effect of these samples. For all cases, the WB of the left MRcollar shell was filled with demineralized water and the water was not circulated. The in-house developed ADAM phantom (T_1: 820 ms; T_2: 37 ms), representing the morphology of an average head and neck patient, was scanned with the clinically used MRT sequence for deep hyperthermia treatments (SNR 85 dB) 24: dual echo gradient echo sequence, 620/4.8/19.1 ms, flip angle 40 °, slice thickness 10 mm, slice spacing 22 mm, 5 slices, FOV 360 × 360 mm^2, matrix size 256 × 256, NEX 1. Images were acquired continuously under three different conditions for a total of 15 min: without water circulation between 0–5 min, during the water circulation between 5–10 min (maximum flow rate 1.5 L/min), and after water circulation was stopped between 10–15 min. Furthermore, a reduced FOV (360 × 270 mm^2) scan was also tested to show the potential effects of WB signal aliasing. MRT maps were calculated using the proton resonance frequency shift method and applying background drift correction using four regions of interest at the edges of the phantom. Since no heating pulses were applied during the experiment, the expected measured temperature change both temporally and spatially was 0 °C. Using this assumption, MRT precision per voxel was calculated by calculating the standard deviation over all PRFS temperature measurements.

7.3 Results

In Table 7.1, a summary of all results is presented. In the following sections, each measurement will be investigated in detail.

7.3.1 MR Relaxometry Measurements

In Figure 7.1, example magnitude images acquired with multi echo gradient echo sequence at echo time 1.3 ms for different solutions are shown. Qualitative analysis on MRI images show it is possible to reach signal void for every compound. The calculated T_2* times at 1.5 T are given in Table 7.1. The values for 1250 mM $CuSO_4$, 25 mM $MnCl_2$ and 10 mM Fe_3O_4 solutions were omitted because the fitting failed due to low SNR. In order to reduce the WB signal to the noise level, at least 5 mM Fe_3O_4, 12.5 mM $MnCl_2$, or 1000 mM $CuSO_4$ was required.

7.3.2 Electromagnetic Property Measurements

In Figure 7.2, the change in electrical conductivity in the frequency range of 50–600 MHz is illustrated. All three compounds show a linear increase in conductivity with concentration. Addition of Fe_3O_4 didnt change the conductivity of demineralized water. However, $MnCl_2$ and $CuSO_4$ had a larger effect. In the case of highest concentration solutions as compared to the demineralized water, conductivity was increased 133 times for $CuSO_4$, and 13 times for

Table 7.1: T_2* at 1.5 T, conductivity and relative permittivity of demineralized water and different water solutions at 100 and 434 MHz, and their effect on hyperthermia treatment planning parameters target-to-hotspot quotient (THQ), the target coverage of the 50% iso-SAR volume (TC50 [%]) and required power to reach 44 °C in the healthy tissue (Power [W]) for two different MR compatible RF hyperthermia devices. T_2* values donated with ≈ are not fitted due to low SNR.

		MRcollar					Sigma Eye				
	T2* (ms) at 1.5 T	σ (S/m) at 434 MHz	ϵ at 434 MHz	THQ	TC50 (%)	Power (W)	σ (S/m) at 100 MHz	ϵ at 100 MHz	THQ	TC50 (%)	Power (W)
Demineralized Water	120	0.04	79.2	0.43	23	180	0.001	79.1	0.57	11	1201
50 mM $CuSO_4$ Solution	10.8	0.59	82.1	0.39	22	570	0.495	83.5	0.57	2	9564
100 mM $CuSO_4$ Solution	6	0.95	84.2	0.32	14	1110	0.831	86.0	0.47	2	23948
250 mM $CuSO_4$ Solution	3.47	1.85	87.5	0.18	0	4761	1.683	89.7	0.16	0	N/A
500 mM $CuSO_4$ Solution	1.94	3.03	88.1	0.10	0	N/A	2.849	91.1	0.04	0	N/A
1000 mM $CuSO_4$ Solution	1.09	4.76	83.5	0.05	0	N/A	4.583	88.7	N/A	N/A	N/A
1250 mM $CuSO_4$ Solution	≈	5.34	79.9	0.04	0	N/A	5.171	85.4	N/A	N/A	N/A
0.5 mM $MnCl_2$ Solution	11.47	0.03	78.9	0.42	23	177	0.005	78.1	0.57	12	1185
1 mM $MnCl_2$ Solution	6.27	0.05	78.9	0.43	22	187	0.017	78.2	0.57	10	1337
2.5 mM $MnCl_2$ Solution	3.77	0.08	79.0	0.43	22	203	0.051	78.2	0.57	5	1656
5 mM $MnCl_2$ Solution	2.35	0.14	79.0	0.44	22	230	0.105	78.3	0.58	5	2181
12.5 mM $MnCl_2$ Solution	1.13	0.29	78.9	0.42	21	325	0.256	78.6	0.57	4	4144
25 mM $MnCl_2$ Solution	≈	0.53	79.0	0.40	22	503	0.488	78.8	0.57	2	9734
0.25 mM Fe_3O_4 Solution	6.42	0.04	79.2	0.42	22	181	0.001	78.9	0.56	10	1236
0.5 mM Fe_3O_4 Solution	4.1	0.04	79.2	0.42	22	179	0.001	78.9	0.57	7	1105
1 mM Fe_3O_4 Solution	2.71	0.04	79.2	0.42	23	181	0.001	78.9	0.57	6	1132
2.5 mM Fe_3O_4 Solution	1.44	0.04	79.2	0.43	22	183	0.002	78.9	0.57	9	1159
5 mM Fe_3O_4 Solution	1.07	0.04	79.2	0.43	22	191	0.003	78.9	0.56	10	1163
10 mM Fe_3O_4 Solution	≈	0.05	79.2	0.43	22	186	0.006	78.9	0.57	7	1158

$MnCl_2$ at 434 MHz. Permittivity of all solutions were stable and was equal to water relative permittivity in the frequency range (79 ± 0.2 at 434 MHz).

7.3.3 Effects on SAR Patterns and Applicator Efficiency

In Figure 7.3, example predicted SAR patterns achieved for the solutions satisfying the MRI requirements are shown. In the Figure 7.3a, the clinical standard demineralized water is visualized. Using that setup (σ: 0.001 S/m at 100 MHz, σ: 0.04 S/m at 434 MHz), THQ

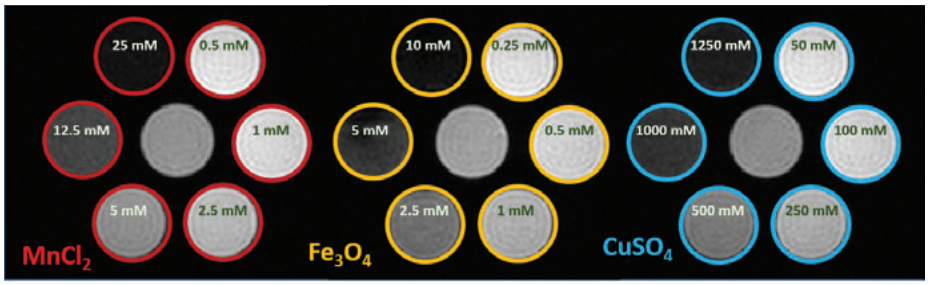

Figure 7.1: Grayscale MR magnitude images acquired with multi echo gradient echo sequence for different $MnCl_2$, Fe_3O_4, and $CuSO_4$ concentrations at echo time of 1.3 ms. Complete signal suppression were achieved for each compound for the sample with the highest concentration.

of 0.46 and TC50 of 23% for the head and neck patient, and THQ of 0.57 and TC50 of 11% for the deep pelvis patient was achieved. The required power levels to reach maximum efficacy in the treatment were 180 W and 1200 W for MRcollar and Sigma Eye applicators, respectively. As illustrated in the Figure 7.3 and reported in Table 7.1, although 1000 mM $CuSO_4$ solution (σ: 4.5 S/m at 100 MHz, σ: 4.8 S/m at 434 MHz) is able to nullify the MRI WB signal, it appears not suitable for hyperthermia purposes due to the high losses. On the other hand, 5 mM Fe_3O_4 solution (σ: 0.003 S/m at 100 MHz, σ: 0.04 S/m at 434 MHz) had no effect on the SAR pattern and required only a small change in power (ΔW: −37 W for Sigma Eye and ΔW: 11 W for MRcollar) to achieve maximum effectiveness. Finally, it is possible to reach similar predicted SAR patterns with a 12.5 mM $MnCl_2$ solution (σ: 0.001 S/m at 100 MHz, σ: 0.04 S/m at 434 MHz). However, this goes at the cost of additional

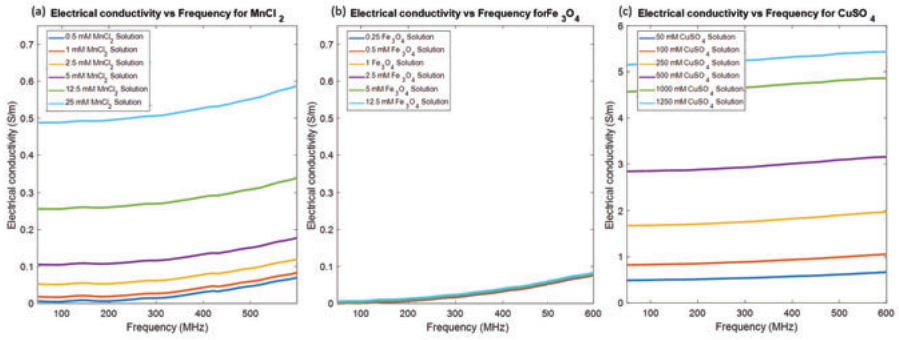

Figure 7.2: Electrical conductivity over the investigated frequency band for different (a) $MnCl_2$, (b) Fe_3O_4, and (c) $CuSO_4$ concentrations. Note that the scale in figure (**c**) is different.

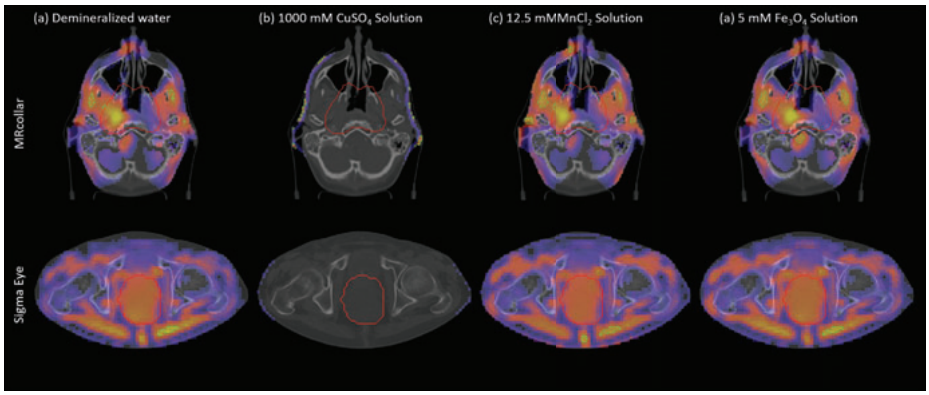

Figure 7.3: Predicted SAR distributions for models of patients treated with head and neck (MRcollar) and deep pelvis (Sigma Eye) hyperthermia when the WB is filled with (**a**) demineralized water, (**b**) 1000 mM $CuSO_4$ solution, (**c**) 12.5 mM $MnCl_2$ solution, and (**d**) 5mM Fe_3O_4.

hot-spots at the skin and total RF-input power needs to be increased by 3000W for Sigma Eye and 145W for MRcollar to achieve the same treatment efficacy.

Our investigations reported in the previous three sections show that $CuSO_4$ is not a suitable compound for our aim. On the other hand, both 12.5 mM $MnCl_2$ and 5 mM Fe_3O_4 solutions appeared suitable for hyperthermia purposes. As such, these have been experimentally tested in the treatment setup.

7.3.4 Effect on MRT Precision

In Figure 7.4, the MRT and the temperature standard deviation (σ) maps acquired during water circulation are shown for demineralized water, 12.5 mM $MnCl_2$ solution, and 5 mM Fe_3O_4 solution. Note that flow was applied between the 5–10 min. In Table 7.2, the mean, standard deviation and maximum temperature errors are given for all three cases before, during and after applying (doped) water circulation. The temperature precision on average in the phantom when demineralized water was used in the WB was 0.17 °C, 0.70 °C, 0.29 °C without water circulation, during water circulation, after water circulation respectively. Hence, the flow severely affects MRT precision. Precision improved to 0.15 °C, 0.16 °C, and 0.26 °C when the demineralized water was doped with 12.5 mM $MnCl_2$. The reduction in the FOV made possible by reduction of the signal from the WB further improved precision to 0.11 °C when circulation was on. Figure 7.4c shows the signal aliasing from the antenna modules that are filled with demineralized WB, while there is no aliasing from the right WB (left in the image), which contained $MnCl_2$-doped water. MRT precision was the highest when the 5 mM Fe_3O_4 solution was used, i.e., 0.09 °C, 0.11 °C, and 0.11 °C (full FOV: without, during and after circulation), and 0.09 °C (reduced FOV: during circulation). Figure

Table 7.2: Mean, standard deviation and maximum temperature errors before water circulation, during water circulation, after water circulation when demineralized water, 12.5 mM $MnCl_2$ solution, and 5mM Fe_3O_4 solution is used in the WB.

		Demineralized Water	12.5 mM $MnCl_2$ Solution		5 mM Fe_3O_4 Solution	
		Full FOV	Full FOV	Reduced FOV	Full FOV	Reduced FOV
Before Circulation	Mean error (°C)	−0.06	−0.06		−0.06	
	Std (°C)	0.17	0.15		0.09	
	Max error (°C)	1.28	1.89		−1.36	
During Circulation	Mean error (°C)	0.04	−0.03	−0.05	−0.13	−0.03
	Std (°C)	0.70	0.16	0.11	0.11	0.09
	Max error (°C)	41.8	−2.00	−2.05	−1.57	1.32
After Circulation	Mean error (°C)	0.20	−0.16		−0.05	
	Std (°C)	0.29	0.26		0.11	
	Max error (°C)	28.1	5.40		−2.60	

7.4e clearly shows that, while the signal aliasing from the antenna modules are visible, the signal from the WB is absent. A similar improvement in the maximum error values was seen when 5 mM Fe_3O_4 solution were used instead of demineralized water and $MnCl_2$ solution. The maximum error values were always found for single voxels at the phantom air interfaces, near the right side of the phantom. This error is mainly caused by the steep phase changes in these interfaces and the partial volume effect. In the clinical scenario, such values are masked by using maximum temperature difference thresholding.

7.4 Discussion

In this study, we determined that doping the water in the WB by (5 mM) Fe_3O_4 satisfies the needs for MRI signal suppressing while having no effect on the SAR pattern and applicator efficiency. The concentrations of Fe_3O_4 used in this study do not change the electromagnetic properties of the demineralized water, hence the predicted RF-power deposition patterns and efficiency is the same as in the currently used clinical setup. Local magnetic field inhomogeneity created by Fe_3O_4 particles causes rapid MR signal decay, therefore it is ideal for MRI signal suppression. In our MRI experiments, this effect resulted in on average 75% improvement in MRT precision. Hence, (1) the substantial improvements in the MRT precision, (2) the absence of an effect on both the predicted SAR and power efficiency and (3) its simple use makes adding Fe_3O_4 the water in the WB a very elegant solution that can considerably improve MR guided hyperthermia.

Our results show that $MnCl_2$ and $CuSO_4$ can be used for WB signal suppression. However, this comes at the expense of heating efficiency reduction (at least 80% increase in the total input power is required). A WB solution including $MnCl_2$ and reducing the FOV improved the MRT precision by 70% compared to the demineralized water setup. Although this re-

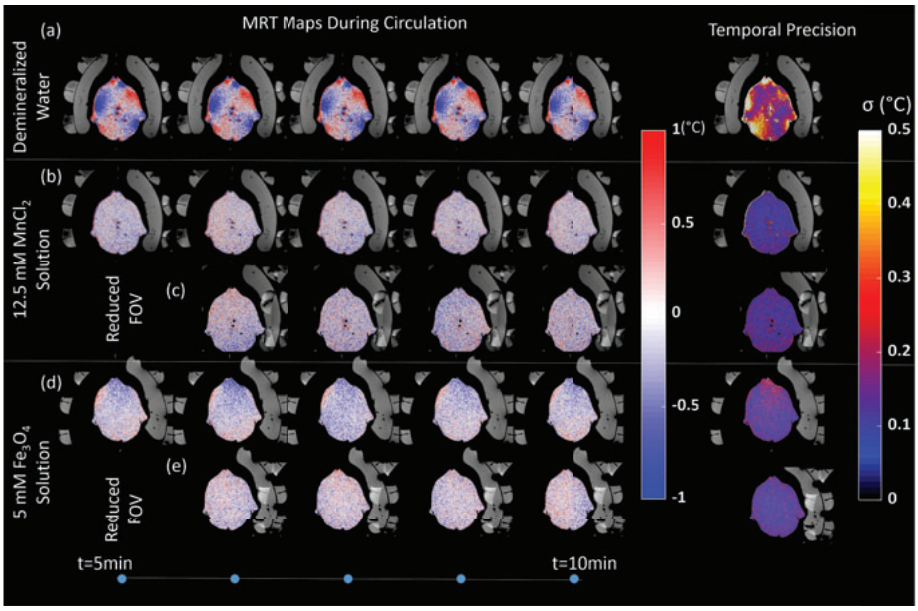

Figure 7.4: MRT maps and temporal precision map during the water circulation when the applicator right side WB (left in the image) was filled with (first row (a)) demineralized water; (second (b) & third row (c)) 12.5 mM $MnCl_2$ solution full and reduced Field of View, respectively; (fourth (d) &fifth (e) row) 5 mM Fe_3O_4 solution full and reduced Field of View, respectively. In the last column, MRT precision per voxel during the water circulation is shown. The expected measured temperature change both temporally and spatially was 0 °C. Using this assumption, MRT precision was calculated by calculating the standard deviation over all PRFS temperature measurements. Note that the applicator left side WB (right in the image) was always filled with demineralized water for reference.

markable improvement, energy losses in the WB are high due to the increase in the conductivity. For the head and neck hyperthermia setup, the power demands can be supplied by the power amplifiers available in our clinic. However, the power demands for the deep pelvis hyperthermia applicator is above the total amount that power amplifiers can provide, and hence, unfeasible. In addition, the increased power loss in the WB put additional constraints on the cooling of the water in order to keep the patient comfortable. Additional heat stress caused by the WB is highly unwanted. Lastly, $CuSO_4$ solutions that can nullify MRI signal create a very lossy medium which leads to unacceptable losses in the WB of the RF hyperthermia applicators.

This paper presents the first comprehensive analysis on the T_2 shortening agents to be used in the WB for MR RF guided hyperthermia treatments. The results of our work demonstrate

the ability of these agents to improve different aspects of the treatment. First, they can reduce temperature measurement errors caused by the water motion. As it has been demonstrated by our results when the demineralized water circulated, the flow severely affects the MRT precision. This effect was largely eliminated with the addition of T_2 shortening agents. The reported MRT accuracy of RF hyperthermia devices are in the range of 1 °C[192]. However, there is a clear thermal dose effect relation[47,230–232] and hotspots in normal tissues still hamper current treatments. Any gain in temperature monitoring will allow to adapt heating settings to improve treatment. These studies also suggest that even small increases in temperature of 0.5 °C can lead to improved treatment outcome. Hence, the improvement by the proposed approach will lead to a clinically relevant improvement in treatment monitoring, which will improve treatment reporting and can be used for adapting the treatment. Second, the FOV reduction improves resolution and reduces partial volume effects as well as the scan time, both of crucial importance. This last point, indeed, may result in a shortening of the scan times, increase in data sampling rate, or higher temperature precision by altering the sequence parameters (e.g., by increasing repetition time). At the same time, Fe_3O_4 solutions have the same electromagnetic properties of the demineralized water hence the utilization of these solutions have no direct trade offs for the RF hyperthermia treatments. In addition to these technical improvements, there is another very important benefit due to the possibility to continue water flow: continuity in the cooling of superficial tissues of the patient during heating. This will help to reduce superficial hotspots to improve patient comfort, and consequently will help to reduce patient movements. Moreover, continuous cooling and improved comfort increase the patients tolerance to the hyperthermia treatment and therefore provides the clinical condition required to maximize thermal dose to each patient.

In this study, we have shown the potential of the T_2 shortening agents using numerical modelling and experimentally in clinically representative setup. However, the actual clinical setup includes components that is not addressed here; mainly the heating RF signal and involuntary patient motion. It is known that for example artefacts from introduction of additional frequencies can occur and image noise increases with increasing power[233]. Although, heating RF signal causes artifacts, its affect will be equal in all cases. Similarly, involuntary motion such as breathing, bowel movement etc. will affect all setups equally. Therefore, while our results can be optimistic for real clinical usage, the potential relative improvement compared to the demineralized water in the WB cannot be underestimated.

The main advantage of the use of demineralized water is its biocompatibility and biodegradability. Fe_3O_4 nanoparticles are also biocompatible and used for magnetic hyperthermia treatments[234]. An unstudied potential issue is long term degradation of the device due to the additive. If this turns out to be a problem, all the parts of the device in contact with the circulated fluid (antennas, tubing, connectors etc.) might need corrosion inhibition, for instance coating.

In our investigation, we focused on MR guided RF hyperthermia treatments but our findings can also be applied for MR guided HIFU applications. In this case, a WB is used for coupling of acoustic waves and cooling. Removal of WB signal will result in similar improvements in MRT precision as we have shown in this study as shown in[224]. Still, the effect of these

compounds on acoustic properties and their effect on losses in the WB should investigated.

7.5 Conclusions

In this work, we have shown that using Fe_3O_4 nanoparticles doped water instead of the demineralized water in WB can be used to improve MR guided RF hyperthermia treatments. First, MRT precision on average was shown to improve from 0.39 °C to 0.09 °C using a clinical setup and a patient representative head and neck phantom. Second, the Fe_3O_4 concentrations required for MR signal suppression of the WB do not alter the electromagnetic properties of the water in the working frequencies of the RF hyperthermia applicators. Besides the possibility of long term impact on the device, there is no tradeoff in terms of heating and imaging when replacing demineralized water by a Fe_3O_4 solution. Last, doping the water with $MnCl_2$ can also provide similar improvements in MRT precision but it comes with cost of increasing the losses in the WB. In summary, Fe_3O_4 nanoparticles doped water bolus improves the MRT precision with no performance tradeoffs and has great potential to improve RF hyperthermia treatment monitoring under MR guidance.

CHAPTER 8

Potential of multi-coil MRcollar

This chapter is based on:
K Sumser*, GG Bellizzi*, R Forner, T Drizdal, JA Hernandez-Tamames, GC Van Rhoon, MM Paulides. Dual-Function MR-guided Hyperthermia: An Innovative Integrated Approach and Experimental Demonstration of Proof of Principle. *IEEE Transactions on Biomedical Engineering*. 2020 Jul 29. *Joint first author.

Abstract

Temperature monitoring plays a central role in improving clinical effectiveness of adjuvant hyperthermia. The potential of magnetic resonance thermometry for treatment monitoring purposes led to several MR-guided hyperthermia approaches. However, the proposed solutions were sub-optimal due to technological and intrinsic limitations. These hamper achieving target conformal heating possibilities (applicator limitations) and accurate thermometry (inadequate signal-to-noise-ratio (SNR)). In this work, we studied proof of principle of a dual-function hyperthermia approach based on a coil array (64 MHz, 1.5 T) that is integrated in-between a phased array for heating (434 MHz) for maximum signal receive in order to improve thermometry accuracy. Hereto, we designed and fabricated a superficial hyperthermia mimicking planar array setup to study the most challenging interactions of generic phased-array setups in order to validate the integrated approach. Experiments demonstrated that the setup complies with the superficial hyperthermia guidelines for heating and is able to improve SNR at 2-4 cm depth by 17%, as compared to imaging using the body coil. Hence, the results showed the feasibility of our dual-function MR-guided hyperthermia approach as basis for the development of application specific setups.

8.1 Introduction

Typically, radiofrequency (RF) hyperthermia for cancer treatment consists of increasing the temperature of the tumor up to 40-44 °C , commonly using external electromagnetic field sources[51]. Given the demonstrated thermal dose-effect relations[46,47], clinical effectiveness would benefit from achieving higher temperatures. Homogeneous and target conformal heating in the range of 41-43 °C for 30-60 minutes is currently considered optimal[235]. 3-Dimensional temperature monitoring is beneficial to enable real-time dosimetry and treatment guidance. Conventional dosimetry is currently pursued by invasive interstitial thermometry probes, providing limited spatial resolution[45]. Moreover, they are uncomfortable for the patient, time-consuming to set up and often unfeasible[57,236]. Magnetic resonance (MR) thermometry has shown potential for 3D non-invasive temperature monitoring during hyperthermia[77,237]. However, maximum signal-to-noise-ratio (SNR) in MR imaging is critically dependent on the distance of the receiver coils to the region of interest (ROI)[97,238]. Also heating antennas need to be close to the ROI to minimize lengthy and energy absorbing paths of the RF waves through the tissues[197]. This motivated us to envision the next generation of a dual-function integrated approach to MR-guided hyperthermia enabling simultaneous close-to-ROI administration and monitoring of the thermal treatment. In this work, we aim to validate the feasibility of this novel approach.

A number of groups have proposed devices enabling MR thermometry guided hyperthermia treatment[97,102,128,129,192]. However, many intrinsic pitfalls either limited the way to the clinic or their widespread adoption[120]. The first approach used a phased array of twelve dipole pairs working at 100 MHz for heating and relied on the scanner's body coil for MR imaging. Relying on the body coil as receiver yields to low SNR values and hence results in unpredictable MR thermometry accuracy levels[97,120]. A more recent approach by Yeo et al., proposed the use of fast electronic switching to open or short-circuit capacitors[128]. In this way fast switching between C-type heating dipole antenna and MR coil mode was achieved for heating and imaging at 128 MHz (3 T). Another similar approach by Winter et al. used one single 298 MHz RF array for sequentially applying both heating and imaging at 7 T[129]. These latter two approaches allow to install receiver coils and heating antennas close to the patient skin, for achieving an improved imaging SNR level and good heating possibilities. However, these solutions not only require to switch between heating and imaging and imply using MRI scanners >3 T, they also restrict the heating frequency to the MR scanner's Larmor frequency. This limitation hampers to obtain optimal treatments as target conformal heating is only achieved within specific ranges of frequencies that are different for each anatomical region[229]. As an example, the range of 400-600 MHz showed to enable optimal heating in the head and neck region[131,196,239]. Recently, Eigentler et al.[240] proposed a wideband antenna operating in the range of 400-600 MHz, while allowing imaging at 7 T. While this approach solves the problem of choosing the optimal heating frequency, it requires a complex and inefficient switching at high power when going from imaging to heating and ultrahigh field MR imaging, which limits the wide adaptation of MR-guided hyperthermia. In conclusion, a novel approach enabling an independent choice of the heating and imaging

frequency is realistically needed for wide-scale adoption of MR-guided hyperthermia.

A possible solution would be an applicator integrating the two different functions, hence integrating two RF arrays: one for heating at 434 MHz and one for imaging at the MR scanner's Larmor frequency. Through integration, firstly, operating frequencies can be independently chosen allowing to use commercially available MR scanner without compromising on heating quality. Secondly, higher SNR levels needed for accurate MR thermometry would be achieved as the integrated system would stand in the skin proximity. Ideally an integrated system will consist of a heating device leaving sufficient space to integrate local imaging coils where both devices are non- or minimally interfering each other's proper operation. In a first attempt, Paulides et al showed feasibility of applying hyperthermia with 12 patch antennas operating at 434 MHz in a 1.5 T GE 450w MR scanner using the body coil for imaging[61]. However, the patch antennas caused shadowing in the MR-image resulting in poor SNR. This motivated us to design of an innovative Yagi-Uda antenna concept to minimize influence of the hyperthermia antennas on MR compatibility[120].

Therefore, the purpose of this study was to experimentally investigate the feasibility of heating at 434 MHz and imaging at 64 MHz (1.5 T) using an integrated dual-function RF array 1) to identify the needs for clinical systems and 2) to pave the way for application specific phased-array systems design (such as head and neck, breast, etc). A dedicated experimental setup has been manufactured integrating a 2-channel receiver-only coil array for MR imaging at 64 MHz (1.5 T, proton) into a 4-channel heating array at 434 MHz. The scattering parameters of the integrated systems has been characterized by means of a vector network analyzer (VNA). Our aim is to show proof of principle for phased array systems, however this experimental setup resembles a superficial hyperthermia setup. Therefore, we investigated heating performance using the guidelines for superficial hyperthermia[197]. Imaging performances have been investigated in a setup mimicking the final application setup and using the integrated body coil of the 1.5 T MRI-scanner for comparison.

8.2 Materials and Methods

8.2.1 Dual-Function Integrated Experimental System

MR Receiver Coil Array: Design and Compliance Tests

The dedicated coil array is a two-channel receive-only array and consists of two identical rectangular shaped loops (15×8 cm) fabricated as a combination of etched copper wire (0.3 cm diameter) and of copper printed circuit boards (PCBs) with capacitor breaks (trace width of 0.4cm produced by Eurocircuits Gmbh, Belgium). Coils have been tuned and matched when placed on a 2 cm thick deionized water bolus, which was placed on top of a muscle-equivalent phantom having an electrical conductivity of 0.91 S/m and a relative permittivity of 63 at 64 MHz.

The loops were tuned to 63.89 MHz using four tuning capacitors (3×68 pF and 1×56 pF, ATC multi-layer ceramic 100B/TN series) with an additional matching network (2×51 pF, ATC multi-layer ceramic 100B/TN series) at the feed port to achieve 50 Ohm. The loops are connected to a 10 cm (Habia RG174 (50 Ohm, silver-plated copper & copper) coaxial cable at the feed port. The distance between the segmenting capacitors was determined by optimizing the tradeoff between coil load sensitivity and high resistive losses. Further, to minimize coupling between elements in the array, geometric overlap was used to achieve next-neighbor decoupling.

Receive loops were decoupled from the transmit MR body coil by means of both an active and a passive diode detuning circuit. Both circuits were implemented by placing the diode (Macom MA4P7461F-1072T and Microsemi UMX9989AP) in parallel with tuning capacitor to achieve adequate decoupling level. When loaded with the phantom, the detuning performance of the tuned and matched was quantified by switching the diode on and off by means of an external power supply and measuring the S_{21} between the two states.

The noise correlation matrix has been measured to investigate the decoupling level between the two resonant loops. Local static magnetic field artifacts have been investigated by measuring the B_0 map in presence and absence of the coil using the body coil with a spoiled RF Gradient Echo (TR = 50 ms, Flip Angle = 15°, Image Matrix = 256×256, Read out Bandwidth = 31.25 kHz, FOV = 25.6 cm, Slice thickness = 0.1 cm). Finally, the proper functioning of the detuning circuits has been investigated by measuring the B_1 map in presence and absence of the coil using the body coil applying a Bloch-Siegert Shift (TR = 28 ms, TE = 12.4 ms, Flip Angle = 15°, Image Matrix = 128×128, Read out Bandwidth = 31.25 kHz, FOV = 25.6 cm, Slice thickness = 0.1 cm)[240].

Hyperthermia Heating Phased Array

The heating array is made up by two dielectric parabolic reflector antenna modules filed with deionized water for reduction of the antenna geometrical dimensions as proposed in[236]. These modules are tailored antenna encasings with a parabolic back shape and they were designed to reduce the amount of water needed, minimize the cross-coupling, regain focusing and to allow integration of MR surface receive coil. Sizing of each module was engineered to optimize the antenna's reflection and cross-coupling characteristics. The two modules were positioned at 2 cm distance. Each of these modules contains two Yagi-Uda antennas for which heating performance and MR compatibility were verified in a previous study[110]. The two modules were filled with deionized water.

8.2.2 Experimental Setup

A tailored experimental setup was built to demonstrate both heating and imaging capabilities of the dual function hyperthermia applicator in combination with a 1.5 T MRI.

Characterization of the Integrated RF System

Characterization of the integrated system is needed to investigate feasibility of simultaneous operation of the devised approach. To this end, the scattering matrix of both the heating array (434 MHz) and the coil array (63.89 MHz) for MR imaging was measured. Finally, the transmission coefficient (S_{21}) between the two RF systems has been measured to assess feasibility of simultaneous operation[97]. A calibrated (Rohde&Schwarz, ZNC3) VNA was used to perform all measurements.

Heating Experiments

Figures 8.1 and 8.2 show a picture and a schematic representation of the setup used for evaluating the heating performances. It aims at mimicking the clinical application setup in which a water bolus is placed between the patient skin and the dual function applicator. This is used to enhance the electromagnetic coupling and to remove skin heating. The dual function applicator has a surface area of 15×15 cm^2. As illustrated in Figure 8.2a, the coil array was centered on top of a 2 cm thick sealed back representing the water bolus (30×30×2 cm^3) containing deionized water and a plastic sponge for structural support. According to superficial hyperthermia guidelines[197], a 7 cm thick muscle-equivalent phantom (dimensions: (47×47×7 cm^3)) was prepared with a mix of deionized water, agar, sodium chloride, polyethylene powder and TX-151, having electrical conductivity 0.98 S/m and relative permittivity 68 at 434 MHz, thermal conductivity 0.6 W/m/C, specific heat 3800 W/kg/C. The dielectric properties were measured with an open-ended coaxial probe DAK-12 (v2.4 SPEAG) connected to a Rohde & Schwarz ZNC3 vector network analyzer and the thermal properties were measured with a TEMPOS thermal property analyzer, equipped with SH-3 sensor (METER Group AG, Munchen, Germany).

The water boluses were designed according to ESHO guidelines[197] ensuring both an optimal contact area with the phantom and extension beyond the radiating aperture. According to the guidelines, water bags were fabricated to have a planar dimension larger than the heating area (15×15 cm^2). In this work, we kept the water bolus at room temperature of approximately 25 °C. Although water temperature plays a central role, in this work we aimed at demonstrating the dual-functioning of our approach more than optimizing the clinical application of a superficial applicator.

Heating performance have been assessed according to[197]. However, in this work we do not aim at demonstrating the feasibility of a superficial applicator. The temperature rise (TR) and the thermal effective field size (TEFS) have been measured using 180 W total forward power for 4 minutes. The TEFS is defined as the area within the 50% of maximum TR contour in the 1 cm deep plane under the aperture. To this end, we used the described layered muscle-equivalent phantom and an infrared (IR) camera to measure the temperature distribution on the 1 cm deep layer.

Finally, we modelled the experimental setup in Sim4Life (v.5.2.0, Zurich MedTech, Zurich, Switzerland). A 433.92 MHz harmonic excitation signal was applied to each antenna. 20

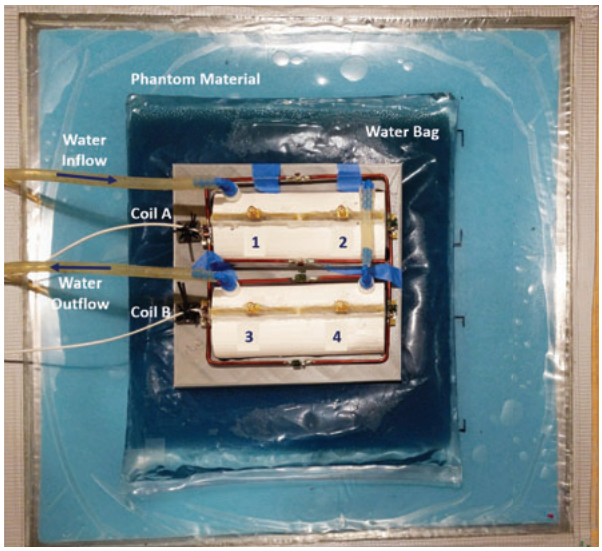

Figure 8.1: Picture of the dual-function integrated RF system.

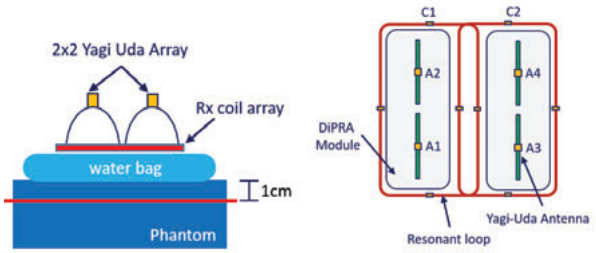

(a) (b)

Figure 8.2: Schematic cross section (a) and top view (b) of the dual-function integrated RF system.

periods were simulated to ensure steady state of all signals. The size of the calculation domain was 11.6 million voxels, with a maximum voxels size of 2×2×2 mm^3). Transient 3D temperature distributions were calculated using the thermal solver in Sim4Life (1 mm uniform grid). The measured dielectric and thermal properties of the phantom were used in the simulations. The initial temperature in the phantom was set to 25 °C and mixed boundary conditions were applied to the phantom background interface (heat transfer coefficients h = 8 W/m^2/°C, and outside temperature T = 25 °C).

MR Imaging Experiments

The experimental setup used for MR imaging experiments is similar to the one described in the section on heating experiments. However, receiver coils are placed on top of the water bolus which is positioned on top of a calibration phantom (CTL Lower TL, P/N U1-150027, GE Medical Systems - MR Division, Waukesha, WI) provided by the MR vendor with T1 of 108 ms and T2 of 96 ms. The SNR was measured using three region of interest (ROI) centered at 3, 6 and 9 cm in this phantom. This investigation has been carried out using water boluses having 2, 4 and 6 cm thicknesses mimicking the clinical scenarios, to assess its effect on image quality. Performances have been benchmarked to the body coil of a GE (General Electric Healthcare, Milwaukee, WI) 450W 1.5 T scanner. A Spoiled Gradient Echo sequence has been used with the following parameters: Flip angle = 21°, FOV = 50 cm, TE = 4.5 ms, TR = 100 ms, and 0.2 cm voxel size.

8.3 Results

8.3.1 Characterization of the Integrated System

Measurement of the scattering matrix for the heating 4-element phased array, operating at 434 MHz, shown a reflection coefficient equal to -20±2 dB and a cross-coupling equal to -31±2 dB. The decoupling between the two RF arrays has been measured at the heating frequency, i.e., 434 MHz, and it is equal to -56±4 dB. The measured reflection coefficient of the Rx-only coil array was -21±1 dB whereas a decoupling of -12 dB has been achieved through geometric overlap of 1.1 cm. The loops have on average an unloaded quality factor of ≈250 and a loaded of ≈30 giving an adequate ratio according to[200]. The noise correlation matrix identified a decoupling level <0.1 between the two resonant loops. Absence of local static magnetic field artifacts has been assessed. The comparison of the two B_1 maps, visualized in Figure 8.3, performed in the presence and absence of the receive array show a deviation of less than 4% proving the proper functioning of the coil array.

Table 8.1: Measured coupling between the heating antenna elements and the receiver coils at 434 MHz.

	A1	**A2**	**A3**	**A4**	**C1**	**C2**
A1	-18.0	-37.4	-30.7	-30.9	-48.5	-59.1
A2	-37.4	-19.6	-29.8	-29.9	-57.0	-58.0
A3	-30.7	-29.8	-19.4	-26.3	-57.5	-52.7
A4	-30.9	-29.9	-26.3	-22.9	-63.4	-54.9

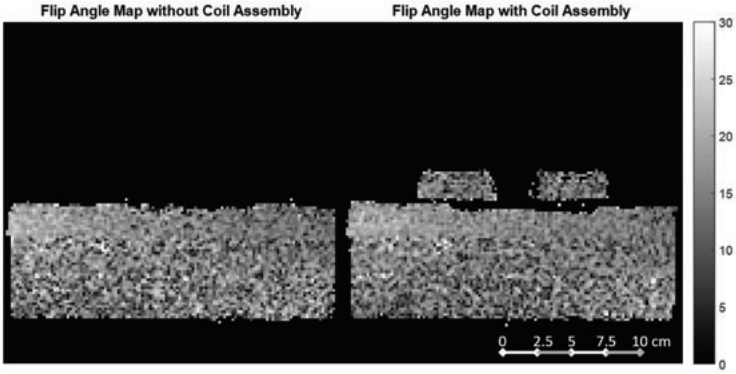

Figure 8.3: Flip angle maps acquired in absence and presence of the dual function applicator

8.3.2 Heating Experiments

Figure 8.4 depicts the simulated and experimental temperature rise map and the corresponding TEFS map achieved when using 180 W forward power for 4 minutes. The numerical model predicted two heat focuses below the antenna modules with the left one smaller than the right one. The measured temperature increase maps shown in the middle figure of Figure 8.4 show qualitative agreement. The measurements appear to be in agreement with the simulations ($R^2 = 0.68$) except for the higher predicted temperature increases at the edges of the phantom. We allocate this mismatch to a mismatch in antenna phases and boundary conditions set for the numerical model. The maximum temperature achieved is +8.6 °C which fulfills the ESHO requirements of 6 °C temperature increase in six minutes[197]. The TEFS map has been drawn according to[197] with the reference temperature TR at 4.3 °C. Results indicate no imprints nor preferential heating caused by the coil that surrounds the antenna cavities.

8.3.3 MR Imaging Experiments

Figure 8.5 depicts the magnitude images acquired when using either the integrated 2-channel coil or the body coil as receiver. The case of a 2, 4 and 6 cm thick water bolus was investigated and images for each case are reported. Figure 8.6 reports the SNR values achieved using three ROI centered at increasing depth from the phantom surface. Results show that the SNR levels achieved using the integrated 2-channel coil are always better than the one achieved using the body coil for any studied thickness of the water bolus. However, as expected, SNR worsens with increasing thickness of the water boluses. At an average depth of 3 cm from the phantom surface, i.e., within ROI 1, a 6 cm thick water bolus wor-

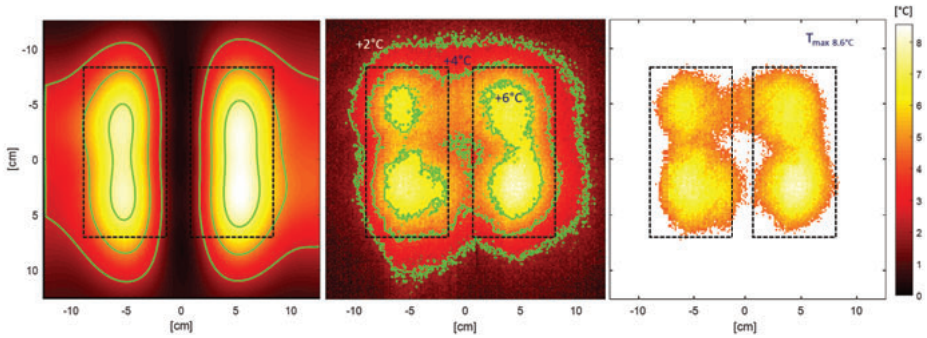

Figure 8.4: (left) Simulated temperature rise map achieved when using 180 W forward power for 4 minutes. (middle) Measured temperature rise map achieved when using 180 W forward power for 4 minutes. (right) Corresponding TEFS map using Tmax equal to 8.6 °C. Antenna cavities shape prediction is overlapped in dashed black lines.

sens the SNR by -8% when compared to a 2 cm thick one. Hence, our results show 2 cm thick water bolus is preferable for the application. In this case, the integrated 2-channel coil achieves an average SNR increase of +17% within ROI 1 (2-4 cm in tissue), when compared to the body coil.

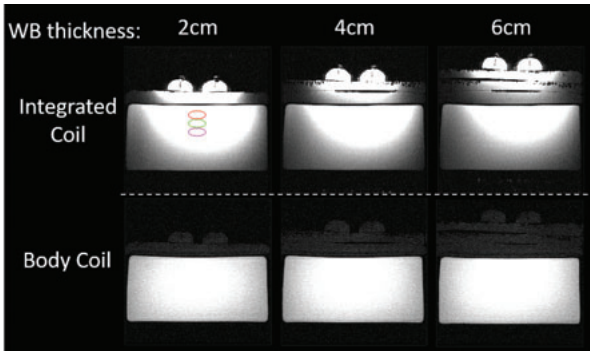

Figure 8.5: Comparison of magnitude images acquired using either the integrated 2-channel coil or the body coil as receiver, when using a 2, 4, and 6 cm thick water boluses. Three ROIs are centered at 3, 6 and 9 cm within the phantom surface and are marked in red, green and magenta, respectively.

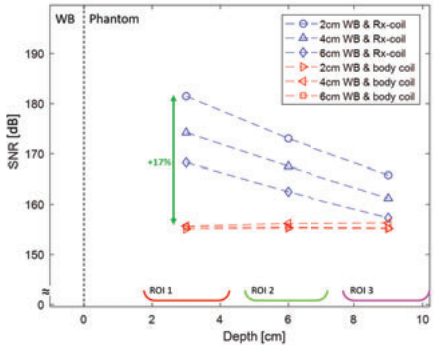

Figure 8.6: Comparison of the SNR levels achieved when using the proposed integrated system or the body coil for increasing depth in the phantom, respectively, ROI 1, 2 and 3.

8.4 Discussion

The results of our investigation experimentally validate the feasibility of our innovative approach to MR-guided hyperthermia, which enables truly simultaneous dual-function operation. The reduced scale setup indicates a minimal system's interaction (-56 dB) between the two RF arrays and suitability for proper functioning both in heating and imaging modality. Our results demonstrate a SNR improvement (+17%) when using close-to-skin receiver MR coils instead of the body coils and heating performances compliant with the superficial hyperthermia guidelines[197]. The results of this paper pave the way of the development of the next generation dual-function integrated approach to MR-guided head and neck hyperthermia systems.

In their pioneering work[97], Gellermann et al. identified that one of the main issues related to MR-guided hyperthermia is the electromagnetic compatibility problem of interference between the MR scanner and the hyperthermia RF applicator. The first is generally able to receive and analyze low-power signals of ţW at its operating frequency, whereas the second aims at transmitting power signals at therapeutic levels of kW (∼2 kW) at a different frequency. They identified the heating signal must be attenuated by -125 dB in the receiving path of the MR scanner. In this framework, the low coupling level between the two RF systems is a crucial feature yielding to simultaneous dual-function operation. The sensibly low coupling (-56 dB) achieved by our approach results from a properly engineering design where geometrical (orthogonal) decoupling of the heating antennas from the imaging coils is pursued[124]. Furthermore, for head and neck hyperthermia, power signals at therapeutic levels do not exceed 300 W. Therefore, in case of more strict requirements, a dedicated RF filter with -60 dB has to be embedded in the MR scanner instead of -105 dB one as proposed in[97].

With this work, we aimed to experimentally validate the feasibility of heating and imaging via an integrated RF array. Investigating both imaging and heating capabilities, we evaluated whether any undesired interaction occurs between the two systems[97]. Also in HIFU devices coils have been integrated for signal receive closer to the target to improve MRT[241,242]. This showed to greatly improve image quality. However, please note that HIFU systems are by definition much better decoupled since these do not exploit electromagnetic waves that interfere with those of the MR scanner. Accordingly, the measured SNR increase when coils are closer to the skin is consistent with the predictions and it suggests the need for a thin waterbolus (<2 cm) towards achieving such SNR levels. When assuming that the temperaturetonoise ratio is proportional to SNR[89], we expect a reduction in the temperature standard deviation of 180% at 2 cm depth from the surface and 31% at 6 cm depth from the surface. Note that these values are theoretical, the actual improvement depends on factors such like motion in and near the region of interest, scanner field drift etc. Besides, the measured heating pattern achieved using the fabricated experimental setup resembles the one achieved in the simulation-guided design phase[110], and there is no interference (e.g., preferred heating paths or distortions) due to the presence of the coil array. Finally, it is noteworthy to stress that such a heating pattern is achieved with an integrated system that was not properly designed and engineered for superficial heating. Although our study shows the proof of principle of coils integrated in an RF hyperthermia device, the setup currently is not optimized with superficial hyperthermia in mind. Since the setup did resemble this application, we used the clear and concise guidelines that exist for this application in our validation[197]. Simultaneously, this setup also covers the most challenging interactions, i.e. those between neighboring elements, of a phased array setup[243]. Hence, for both applications, this study provides a very solid proof of principle.

8.5 Conclusion

In this work, we proposed and experimentally demonstrated the feasibility of an innovative dual-function approach to MR-guided hyperthermia. Our approach is based on a close-to-body integrated system which includes a phased array for optimal heating and a coil array for accurate thermometry. This allows to optimally and independently pick the operating frequencies for heating and imaging without any compromise. Our results show the feasibility of the dual-function MR-guided hyperthermia approach and will pave the way for its development and clinical implementation.

CHAPTER 9

General discussion and perspectives

9.1 Status quo and standardization in MR guided hyperthermia

Among different noninvasive temperature monitoring techniques, MR thermometry is the most promising and so far the only non-invasive 3D temperature monitoring technique that has found its way into the clinical application of hyperthermia. The clinical value of MR thermometry integrated in the BSD2000-3D-MRI RF deep hyperthermia device only, is investigated at five Medical University Centers. Wider research is performed with regard towards the optimal integration of MRT and RF heating using a decoupled or dual-function approach. Given the developments in MR guided RF hyperthermia and the absence of standardization, there was an urgent need for a comprehensive analysis of all devices and validation approaches in this field. The compatibility of these devices with the MRI scanner, and the validation of MRT are often not quantified nor reported in standardized way. Our analysis reviews and proposes validation metrics for the development of MR guided devices.

As a benchmark for the new guidelines, we applied our new approach to the only hybrid MR RF-hyperthermia device in clinical use (BSD2000-3D-MRI). Our quantitative analysis also identified the impact of individual parts of a device. With careful design and choice of materials, the effects of metallic parts and heating signal on MRI image quality are minimized. However, we have demonstrated that the water bolus of the device has the largest impact on the MR image quality due to its effect on B_1^+ efficiency and homogeneity.

9.2 MR guided hyperthermia in the head and neck

As expected, a relevant impact when major vessels transverse the target volume was found. Our results are the first reported results on the use of a clinical workflow to implement patient specific vasculature data in HTP, but in vivo validation of the vasculature effect is lacking. Moreover, in view of this thesis, our results show that MR thermometry is mandatory for accurate thermal dosimetry in head and neck hyperthermia. Alternatives, based on the combination of probe measurements and simulations fail near large vessels so dosimetry will never be complete. A non-invasive temperature monitoring technique like MR thermometry can make this possible given that high enough spatial resolution and spatial temperature accuracy has been achieved.

After identifying the need for temperature monitoring, we started our journey to integrate MRT guidance for heating head and neck tumors. In our approach, we designed a new antenna module that has a small MR footprint. Based on this module, a new phased array applicator, called the MRcollar, was designed. The size and shape of the applicator were optimized using an average patient shape. Integrating a hyperthermia system into the MR imposes design constraints, such as minimization of electrically conductive surfaces. Still, the 12 antenna MRcollar even improved the predicted SAR coverage compared to its predecessor applicator, i.e. the 20 antenna Hypercollar3D. Following our novel procedure, we experimentally validated our design and showed excellent heating performance and minimal interaction with the MR scanner. These results show that virtual prototyping is a valid and powerful tool in device development.

9.3 New hardware-avenues for MRT

After the development of the MRcollar, we aimed towards improving the accuracy of MR thermometry. In our approach, we focused on hardware improvements, namely water bolus improvements and integration of close to skin receiver coils.

The water bolus of a hyperthermia applicator is one of the major sources of temperature errors. In the current clinical practice, way to prevent these errors is to switch off water bolus circulation 1 minute in advance of the measurement. However, as this affect the cooling of the skin and therefore may limit heating quality or increase patient discomfort, we aimed for a solution in which water bolus flow needs not to be interrupted, i.e. by suppressing the water bolus MRI signal. It is important to keep the water bolus economically affordable and not alter the electromagnetic properties. Iron oxide nanoparticles proved to be a perfect solution for this problem. Iron oxide nanoparticles are cheap and easy to apply. We have shown in phantom studies the accuracy of MRT improved without a loss of applicator efficiency. This is an excellent prospect that can potentially improve MRT significantly. Faster and higher resolution scans will facilitate in vivo thermometry.

MRI receiver coils pick up more signal the closer they are to the skin. Therefore, it is highly desirable to use surface or near surface coils during MR guided hyperthermia. However,

integrating two complicated RF systems is challenging. The two systems needs to be decoupled from each other and not alter their operation. To prove feasibility of such device integration, we have built a dual function hyperthermia applicator with the antenna modules designed for the MRcollar and the 1.5 T MR two channel receiver coil combined. Our investigations showed this approach is feasible. Coils do not alter the heating pattern and there is a minimal interaction (-55 dB) between the two systems.

9.4 Future outlook

In this work, the essential hardware tools for precise application of MRT guided head and neck hyperthermia are presented, however, there are still steps that needs to be taken for further improvements. Firstly, the surface coils presented in Chapter 8, needs to be integrated in the MRcollar for maximum SNR. Following the similar design choices, the MRcollar prototype can house a 6-channel coil (3 channels in each half). Also, it is possible to integrate another coil in the cushion supporting the head and neck of the patient. Next, the RF heating signal has to be filtered out from MR receiver channels. While it has been shown that the two systems have low interaction, the MRcollar operates in kW ranges and MRI operates in μW ranges. Hence, a filter is still needed. Based on literature[97] and our interaction measurements, a minus 65 dB bandstop filter at 433 MHz will suffice. Finally, integration of MR-coils, 433 MHz RF-filter and water bolus doping according the new EU Medical Device Regulation will complete all hardware improvements and providing the conditions to start the next phase of preclinical and clinical testing of MRT guided head and neck hyperthermia.

We focused our research on hardware improvements for precise MRT however this may also facilitate software improvements that can provide substantial benefits as well. In recent years, the MRT field advanced mainly through the research in focused ultrasound surgery (FUS). This is due to higher SNR associated with the high temperature increase during FUS and integration of coils in FUS devices compared to the single channel body coil that is used in the MR compatible BSD2000-3D-MRI RF hyperthermia device. In this thesis, we have demonstrated that integration of multi-channel receiver coils is possible in a RF hyperthermia device. This opens the field to introduce several new software based improvements. The current state of the art clinical MR thermometry sequence is not optimized for H&N, it is long (1 minute 32 seconds) and has a FOV which is 50x50 cm^2 with 1 cm slice thickness and slice gap, capturing 25 slices, covering 50 cm of patient abdomen. This is unnecessarily large for H&N area. For an average patient, the region of interest in H&N is 20x20x10 cm^3, based on patient axial H&N area and the length of the focused heating signal ($\approx$8 cm) as shown in Chapter 6. A single slice with 2.5x2.5 mm^2 in plane resolution can be acquired in 8 seconds using a spoiled gradient echo sequence with 100 ms repetition time, echo time 19 ms and flip angle 20°. For treatment monitoring purposes, the volume of interest can be scanned under a minute by 7 slices with a slice thickness of 5mm and slice gap 1 cm. Still, it is possible to reduce the total scan duration. Firstly, the scan times can be shortened by parallel imaging methods[244]. Secondly, scan time reduction can be achieved by simultaneous multi slice ima-

ging (SMS)[245]. In addition to reduction in scan time, the multi-channel receiver coils can improve field drift correction of PRFS thermometry[246]. All this measures combined provide ample opportunities to further improve MRT after the integration of multi-channel coils by new faster and more accurate pulse sequences and post processing techniques.

Introduction of the MRcollar to the clinic will open several possibilities that were not possible so far or not yet accomplished to its full potential. Firstly, MRI can help us better understand the beneficial effects of hyperthermia. Temperature increase maps can be used to calculate thermal dose in the whole treatment volume and to better understand the effects of hyperthermia on disease progression[59]. For diffusion weighted MRI, it has been shown that it also can be used for treatment monitoring in radiotherapy and chemotherapy studies[247]. Hence, it can be used to monitor disease progression and can lead the way for targeted treatments. Secondly, MRI can improve patient modeling. In Chapter 3, we have shown that MRI can be used to acquire information on vessel networks. Additionally, MRI can provide the actual patient anatomy during treatment i.e. including the treatment setup. It has been shown that water bolus pressure induced changes in the patients anatomy from the planning CT and treatment day position affect the treatment accuracy of HTP and subsequently HT treatment quality[248]. Also, it is known that organ motion or deformation can change from day to day. A plan of the day approach may improve the treatment efficacy by accurately model the patient anatomy on the spot[249]. MRI can be used to overcome the confounders in numerical modeling. In the current clinical practice, EM properties of the tissues are assumed to be homogeneous and assigned using literature values[54]. MR electrical property tomography is a technique that can measure in vivo the EM property distribution for the various tissues[250,251]. Adding this information in the hyperthermia treatment planning system will provide a more realistic and representative predicted energy distribution. Finally, MRI can be used to improve the accuracy of thermal models. The main confounder in thermal modeling, the blood perfusion, and the vasculature can be imaged using MRI techniques[157,252]. Output of these techniques can be used directly as more realistic input into the thermal model to calculate the resulting temperature distribution. Combined with MRT, hyperthermia treatment modeling validation can be made during an MR guided hyperthermia treatment. MR guided hyperthermia has a great untapped potential to uncover the clinical benefits of hyperthermia, provide more accurate treatment delivery and bridge the gap between modeling and validation.

While hardware and software improvements are crucial for a successful treatment, patient comfort is often forgotten as being a very important aspect in maximizing treatment quality. One of the main sources of MRT error is inter and intra scan motion. A comfortable patient is less likely to move than an uncomfortable one. Hence, it is important to provide a comfortable experience to the patient. Our work in Chapter 7 shows that it is possible to have a continuous water flow without interrupting MR imaging. Continuous water circulation will reduce superficial hotspots which in turn will help to improve patient comfort and tolerance, therefore a higher thermal dose in a shorter time might be achieved. Additional work, such as development of an ergonomic water bolus, needs to be performed for providing optimal comfort to the patient.

The ultimate goal of MRT guided hyperthermia is to control power deposition using online thermometry. Still, we are yet to tap the potential of MR guided hyperthermia. So far this has not been achieved due to inaccuracy in vivo thermometry data that is strongly hampered by low SNR, motion, heterogeneities, physiological changes, and applicator limitations. In this thesis, we proposed solutions to reduce systematic temperature errors, improve SNR. Further improvements can be achieved by using better pulse sequences, advanced post processing techniques. While pursuing the ultimate goal, MR thermometry information should be integrated in several clinical decision making process. When successful, MRT monitoring shows where the RF-energy is targeted, i.e. maximum in the tumor and hot-spots. As such, it provides the radiation oncologist with crucial information whether we apply the maximum tolerable thermal tumor dose with a minimum probability of toxicity in organs at risk. Further, the accurate knowledge of the temperature distribution might be exploited to adapt the RT-distribution in order to calculate a personalized optimal BED distribution to achieve the highest probability for a cure and minimal probability of toxicity.

Summary

The beneficial effect of hyperthermia as adjuvant to radiotherapy in head and neck cancers are well established with clinical trials. In general, the benefits of hyperthermia are found to be depend on thermal dose. To improve the delivery of thermal dose, a great deal of work has been and still is conducted on device development, treatment planning, patient modeling, and treatment monitoring. Treatment monitoring is an important aspect to ensure correct assessment of treatment quality and dose delivery, as well as validation of modeling and planning. However, in clinic, target temperature increase information is seldom available and clinicians rely on pretreatment SAR calculations. MR thermometry during head and neck hyperthermia is a potential solution to improve 3D information of the applied temperature distribution, but it at present is not yet clinically available and the required temperature measurement accuracy demands technology beyond the current available state of the art.

This thesis starts with first presenting current state of the art MR compatible RF hyperthermia devices. From it, it follows that the field lacks standardization in validation and needs a MRI compatibility benchmark. Secondly it shows that MRT guidance during hyperthermia treatment is required due to the effect of the large vessel network in head and neck region on the temperature distribution. Thirdly, it describes the design and validation of a MR compatible head and neck hyperthermia applicator that can heat at equal quality as the non-MR compatible HYPERcollar3D. Fourthly, the apparent MRT errors due to the water bolus can be effectively and economically solved by doping the water bolus with contrast agents. Lastly, it shows that integration of multi-channel receiver coils in a phased array of RF-antennas is feasible and improves the SNR. These results validate our hypothesis that a suitable combination of hardware technologies enables precise monitoring of the temperature distribution which on its turn will provide the important information to exploit optimal SAR steering during MRT guided H&N HT.

Part 1: State of the art of MR guided RF Hyperthermia and the need of MRT in H&N hyperthermia

In Chapter 2, we present the state of the art in MR guided RF hyperthermia devices, identify the common characteristics of devices and provide the groundwork for improved device validation. Magnetic resonance temperature imaging has been developed for noninvasive 3D temperature imaging and it has been integrated with RF hyperthermia devices. Fifteen different devices were developed, each with distinct characteristics such as frequency of choice, capacitive or radiative heating, hyperthermia only inserts or integrated dual function devices. Only two applicators were actively used in clinical applications and only one of them has become a commercial product. Comparison of these devices is not possible since the validation and reporting of the results were not standardized for heating, MR compatibility or MR thermometry performances. We recommended quantification metrics for standardization of the validation. Chapter 3 continues to explore the needs for standardization and describes a new MR compatibility assessment procedure for MR guided RF hyperthermia devices. We employed this procedure for the assessment of MR compatibility of the commercially available MR compatible RF hyperthermia applicator, Sigma Eye. Our results showed that the device decrease B_1^+ transmit efficiency by 30% and decrease the SNR by 20%, mainly due to the effects of water bolus. Our new procedure is aimed towards quantification of the impact and identifying the parts with the highest impact to be able to reduce their effect.

Part 2: Design and experimental validation of the MRcollar

Due to low availability of in vivo temperature information, clinicians need to rely on electromagnetic or thermal models. While the electromagnetic models are well established and extensively used for treatment planning, actual thermal dose depends on temperature increase. Current clinically used thermal models lack the final important and advanced step of personalization. In Chapter 4, we demonstrated necessary steps to integrate large arteries in head and neck region in the hyperthermia treatment planning work flow and their effect on treatment planning parameters. We have shown that the effect is highly dependent on the individual arterial structure. Three patients out of twelve showed a large drop in treatment quality (0.92 °C on average) while the rest had insignificant change (0.09 °C on average). We conclude that advanced thermal modeling is necessary when the target region includes major vasculature structures. Our conclusions arise from extensive numerical modeling. They still require in vivo validation with 3D thermometry techniques. Since not all patients benefit from these advanced modeling and validation requires in vivo monitoring, integration of in vivo 3D thermometry would be a preferred solution.

Any device intended to be used in MR scanner must be MR compatible. In addition, integration of a hyperthermia device with an MR scanner requires design principles that minimize the system induced image artifact. Hence, an existing hyperthermia device cannot be used

in combination with an MR scanner in its regular form, therefore modifications or redesign of the device is mandatory. Chapter 5 introduces a new MR-friendly antenna concept, and describes the simulation guided design of the MRcollar. In silico results showed that the MRcollar improves the SAR target coverage (TC50) by 8.5% over HYPERcollar3D system. The antenna modules have excellent matching characteristics (S_{11} = -41 dB) and minimal interaction with neighboring elements (S_{12} = -23.1 dB). Additionally, the minimal metallic surfaces ensures limited B_1 and B_0 distortions during MR imaging. MR experiments showed the antenna modules of the MRcollar do not affect MR transmit/receive performance.

The purpose of the work described in Chapter 6 was to experimentally validate the MRcollar design and MRI compatibility as is reported in Chapter 5. The MRcollar system has satisfactory and robust matching characteristics and low interaction between the individual antenna modules. Heating and focusing capabilities were tested by using three different focus settings. The predicted and experimentally measured SAR patterns have a good match (≈95%). Heating requirements as demanded by the European Society for Hyperthermic Oncology (6 °C increase in 6 minutes) were easily reached (6 °C increase in 2 minutes). The MRcollar was shown to have minimal effect on the image quality in the clinical relevant part of the field of view. However, the water bolus reduces B_1 efficiency and consequently the SNR. Overall, the MRcollar has great potential to improve hyperthermia delivery in the head and neck region.

Part 3: New hardware avenues for MRT

We have shown that considerable efforts have been made for integration of MR thermometry with RF hyperthermia. However, in vivo accuracy is still not accurate enough. Efforts were focused on hardware improvements to improve the accuracy of MR thermometry. The water bolus is one of the main apparent temperature error sources in the hyperthermia device. In Chapter 7, we report on the potential of adjusting water bolus filling properties to improve MR thermometry by making the water bolus MRI transparent. In this study, we used three different compounds ($CuSO_4$, $MnCl_2$, Fe_3O_4) known for T_2^* reducing capabilities to modify water bolus properties. We have found that it is possible to make the water in the water bolus MRI transparent with the tested compounds. However, only Fe_3O_4 had no effect on electromagnetic properties, thus making it the only possible solution. Furthermore, we showed that a Fe_3O_4 doped water bolus compared to a demineralized water doped water bolus resulted in an improved MR thermometry precision during water circulation from 0.70 °C to 0.09 °C with a reduced FOV scan. This new solution provides two important technical advancements. Firstly, in the current state-of-the-art, water circulation stops when the MR imaging takes place. As a consequence cooling of skin hotspots is interrupted with subsequent reduction of patient comfort. Continuous cooling will maintain patient comfort and help to increase the patients tolerance to hyperthermia. Secondly, the reduction of FOV reduces scan time, partial volume effects and improve resolution. Each effect is crucial for improving the MR thermometry accuracy. Therefore we conclude that Fe_3O_4 doped water

bolus has significant potential to improve RF hyperthermia treatment monitoring under MR guidance.

Significant improvements can be made in SNR by using MR coils close to skin. Chapter 8 shows the investigations done towards the integration of the coils in the MRcollar. Prior to integrating the coils in the MRcollar, we designed a reduced scale planar array setup and integrated a two channel MR receive coil with two RF-hyperthermia applicator modules. In this setup the most challenging interactions between two RF systems are realized. With this experiment we have shown that the integrated MR receive coils do not affect the heating patterns of the antenna modules designed in Chapter 4. The surface coils improved SNR by 17% compared to the body coil. The interaction between the two systems is very low (-56 dB). Of course for protection of the MRI hardware, it still remains necessary to filter out high power heating RF signal from the MRI scanners low power receivers.

Over the past decades, substantial progress has been made in head and neck hyperthermia and MRT guided hyperthermia treatment. Here, we developed essential tools for MRT guided head and neck hyperthermia treatments: the MRcollar, a new water bolus solution and integrated MR coils. We foresee with the tools provided in this thesis that accurate thermal dosimetry will be possible during the head and neck hyperthermia treatments, leading to better understanding of the effects of hyperthermia and accurate thermal models. Furthermore, our investigations on optimal water bolus properties and integration of surface coils can be implemented for other hyperthermia devices intended to be used in body sites other than head and neck.

Samenvatting

Het positieve effect van het toevoegen van hyperthermie aan radiotherapie is in meerdere klinische studies aangetoond. In het algemeen is gevonden dat het klinische effect van hyperthermie afhankelijk is van de toegediende thermische dosis. Hoewel al veel onderzoek is verricht is onderzoek gericht op verbetering van de hyperthermie apparatuur nog steeds actueel. De continue toename in computer technologie is een grote stimulans voor het ontwikkelen van steeds betere en snellere mathematische modellen om de energie en temperatuur verdeling tijdens de hyperthermie behandeling te berekenen. Tevens is er ook een constante verbetering in de monitoring van de behandelkwaliteit en de temperatuurverdeling. Beide zijn onmisbaar bij de validatie van de modelberekeningen. Zowel de arts als de patient zijn echter niet enthousiast over het plaatsen van invasieve katheters. Als gevolg daarvan is tijdens de klinische uitvoering van de hyperthermie behandeling van hoofd-hals tumoren invasief gemeten tumor temperatuur zeer beperkt beschikbaar. De toediening van de hyperthermie behandeling gebeurt dan geheel op geleide van de berekende energie verdeling en het gevoel van de patiënt. Het niet invasieve meten van de weefsel temperatuur met behulp van een MRI biedt hier een mogelijke oplossing om de behandeling toch op basis van de gemeten weefsel temperatuur uit te voeren. De techniek om met de huidige state of Art MRI technologie de temperatuur te meten is echter onvoldoende nauwkeurig en robust.

Het proefschrift start met een overzicht van bestaande systemen waarmee binnen de MR omgeving de radiofrequente elektromagnetische velden gebruikt kunnen worden voor de hyperthermie behandeling. Uit het overzicht volgt het gebrek aan standaardisatie, en in response hierop wordt een benchmark gepresenteerd voor het kwantitatief vaststellen van de MR-compatibiliteit van een hybride systeem. Vervolgens wordt het belang van sturing van de hyperthermie behandeling op geleide van MR-thermometrie ter vermindering van de invloed van grote bloedvaten op de temperatuurverdeling in het hoofd-hals gebied getoond. Aansluitend wordt de ontwikkeling en validatie van een nieuwe MR compatibele applicator voor hyperthermie van hoofd-hals tumoren beschreven, waaruit volgt dat de kwaliteit van de hyperthermie behandeling met de nieuwe applicator gelijk is aan de niet MR-compatibele

HYPERcollar3D. Tevens wordt aangetoond dat toevoeging van een contrast middel aan het water in de bolus een effectieve en economische oplossing is om fouten in de MR-thermometrie te verminderen. Tot slot laat het proefschrift zien dat het mogelijk is om meerdere ontvangst spoelen dichtbij de RF-antennes van een phased-array applicator te plaatsen. Samengevat laat het onderzoek zien dat door het combineren van MR-meettechnieken en RF-verwarmingstechnieken het mogelijk wordt om met behulp van MR-thermometrie de temperatuurverdeling in het hoofd-hals gebied tijdens de hyperthermie behandeling nauwkeurig te meten en gelijktijdig RF-energieverdeling optimaal te sturen voor een maximale effectiviteit van de behandeling.

Deel 1: State of art van MR-geleide RF hyperthermie en de noodzaak van MRT tijdens H&N hyperthermie

In hoofdstuk 2 presenteren we de huidige stand van de techniek in MR-geleide RF hyperthermietoestellen, identificeren we de gemeenschappelijke technische kenmerken van toestellen en leggen we de basis voor een betere validatie van de toestellen. Magnetic Resonance Temperature Imaging is ontwikkeld voor niet-invasieve 3D-temperatuurbeeldvorming en is geïntegreerd in vijftien verschillende RF-hyperthermietoestellen. Elk apparaat heeft zijn eigen kenmerken zoals frequentie, capacitieve of radiatieve verwarming, alleen als toevoeging voor hyperthermie of als geïntegreerde apparaat met een dubbele functie. Slechts twee apparaten worden actief gebruikt in klinische toepassingen en slechts één ervan is een commercieel product geworden. Het vergelijken van de prestatie van deze apparaten is helaas niet mogelijk omdat de validatie en rapportage van de resultaten niet gestandaardiseerd zijn voor verwarming, MR-compatibiliteit of MR-thermometrie. Om in deze apparatuur in de toekomst wel te kunnen vergelijken, bevelen wij aan de prestaties kwantitatief volgens gestandaardiseerde metingen te valideren. Hoofdstuk 3 vervolgt met onderzoek naar mogelijke standaardisatie en beschrijft een nieuwe evaluatie procedure voor het meten van de MR-compatibiliteit voor MR-geleide RF-hyperthermietoestellen. De procedure is gebruikt voor de beoordeling van MR-compatibiliteit van de Sigma Eye, de enige commercieel verkrijgbare MR-compatibele RF-hyperthermie-toestellen. Onze resultaten laten zien dat de applicator de $B_1{}^+$ transmissie-efficiëntie met 30% vermindert en de SNR met 20%, waarbij de waterbolus de belangrijkste oorzaak van deze effecten is. Onze nieuwe validatie procedure richt zich op het kwantificeren van de impact en het identificeren van de onderdelen met de grootste impact. Hierdoor kunnen gerichte maatregelen ontwikkeld worden om het effect te verminderen.

Deel 2: Ontwikkeling en experimentele validatie van de MR-collar

Gedwongen door de zeer beperkte beschikbaarheid van de momentane weefseltemperatuur moet de clinicus vertrouwen op elektromagnetische of thermische modellen en de terugkoppelring van de patiënt. Hoewel elektromagnetische modellen steeds betrouwbaarder worden en breed worden toegepast voor de planning van de behandeling, wordt de uiteindelijk toegediende thermische dosis bepaald door de werkelijke temperatuurstijging die afhankelijk is van de lokale doorbloeding. De lokale doorbloeding is patiënt en tumor specifiek. Alle huidige klinisch gebruikte thermische modellen missen deze laatste, essentiële personalisatie stap. In hoofdstuk 4 wordt dit personalisatie proces gedemonstreerd voor de grote slagaders in het hoofd- en nekgebied en wordt hun effect op de voorspelde temperatuurverdeling tijdens de hyperthermieplanning berekend. We laten zien dat het effect sterk afhankelijk is van de individuele arteriële structuur. Drie van de twaalf patiënten vertonen een grote daling in de kwaliteit van de behandeling (gemiddeld 0,92 °C), terwijl de rest geen of een minimale verandering laat zien (gemiddeld 0,09 °C). Volgend op de uitgebreide numerieke modelering, concluderen we dat geavanceerde thermische modellering noodzakelijk is wanneer het doelgebied grote bloedvaten bevat. Daarbij moet worden opgemerkt dat de verrichte berekeningen nog wel in vivo validatie vereisen. Omdat niet alle patiënten baat hebben bij geavanceerde temperatuur modellering en validatie uitgebreide in vivo temperatuur monitoring vereist, is er een duidelijke behoefte aan integratie van niet invasieve, in vivo 3D thermometrie, bijvoorbeeld MR-thermometrie.

Elk apparaat dat bedoeld is om in een MR-scanner te worden gebruikt, moet MR-compatibel zijn. Bovendien vereist de integratie van een hyperthermieapparaat met een MR-scanner ontwerpprincipes die door het hyperthermieapparaat geïnduceerde beeldartefacten tot een minimum beperken. Daarom kan een bestaand hyperthermieapparaat niet zonder aanpassingen worden gebruikt in combinatie met een MR-scanner. Ontwerpwijzigingen of zelfs een volledig herontwerp van het hyperthermie apparaat is noodzakelijk. Hoofdstuk 5 introduceert een nieuw antenne concept, en beschrijft het proces om te komen tot een simulatie geleid ontwerp van de MRcollar. De berekende, in silico resultaten tonen aan dat de MR-collar de energie (SAR) in het doelgebied (TC50) met 8,5% verbetert ten opzichte van het huidige, klinisch toegepaste HYPERcollar3D-systeem. Dankzij een nieuw ontwerp van de antennemodule, heeft de MRcollar ook 31% minder water nodig,. De antennemodules hebben daarnaast uitstekende elektromagnetische eigenschappen (S_{11} = -41 dB) en vertonen minimale interactie met naburige elementen (S_{12} = -23.1 dB). Bovendien zorgen de geminimaliseerde metaaloppervlakken voor zeer beperkte B_1 and B_0 vervormingen tijdens de MR-beeldvorming. Uit de verrichte MR-experimenten volgt dat de antennemodules van de MRcollar inderdaad geen invloed hebben op de prestaties van de MR-zender/ontvanger.

Het doel van het onderzoek, beschreven in hoofdstuk 6, is de experimentele validatie van het totale MRcollar-ontwerp en de MRI-compatibiliteit, zoals die in hoofdstuk 5 voor de onderdelen wordt gerapporteerd. Het totale MRcollar-systeem functioneert zoals verwacht

met goede en robuuste eletromagnetische matchingskarakteristieken per antennemodule en een lage interactie tussen de afzonderlijke antennemodules. De verwarmings- en SAR-stuur mogelijkheden werden getest met behulp van drie verschillende focus instellingen. De voorspelde en experimenteel gemeten SAR-patronen hebben een goede overeenkomst (≈95%). Verwarmingsvereisten zoals opgesteld door de European Society for Hyperthermic Oncology (6 °C verhoging in 6 minuten) werden gemakkelijk bereikt (6 °C verhoging in 2 minuten). De MRcollar bleek een minimaal effect te hebben op de beeldkwaliteit in het klinisch relevante deel van het MRT-meetgebied. De waterbolus vermindert echter wel de B_1-efficiëntie en daarmee de SNR. Alles tezamen biedt de MRcollar een enorm potentieel om toediening van - en niet-invasieve temperatuurmeting tijdens - hyperthermie in het hoofd- en nekgebied te verbeteren.

Deel 3: Nieuwe technologie voor verbetering MR-thermometrie

Ondanks dat er veel energie is gestoken in de integratie van MR-thermometrie met RF-hyperthermie, is de in vivo meetnauwkeurigheid van de temperatuur nog onvoldoende. Tot op heden waren de inspanningen om de nauwkeurigheid van MR-thermometrie te verbeteren vooral gericht op aanpassingen van de hardware. Uit ons onderzoek volgt dat de waterbolus in het hyperthermieapparaat één van de belangrijkste bronnen is voor de temperatuur meetfout. In hoofdstuk 7 rapporteren we over de mogelijkheden tot het verbeteren van de eigenschappen van de waterbolus om de waterbolus MRI-transparant te maken en daarmee de nauwkeurigheid van de MR-thermometrie te verbeteren. In deze studie hebben we drie verschillende verbindingen ($CuSO_4$, $MnCl_2$, Fe_3O_4) gebruikt, die alle bekend zijn om hun $T_2{}^*$-reducerend effect om daarmee de waterboluseigenschappen aan te passen. De uitkomst was dat het met alle drie de materialen mogelijk is om het water in de waterbolus MRI transparanter te maken. Alleen Fe_3O_4 had echter geen effect op de elektromagnetische eigenschappen van het water. Hierdoor is Fe_3O_4 de enig bruikbare oplossing. Daarnaast hebben we aangetoond dat een Fe_3O_4 gedoteerde waterbolus in vergelijking met een gedemineraliseerde waterbolus inderdaad resulteert in een verbeterde MR-thermometrieprecisie tijdens actieve watercirculatie van 0,70 °C tot 0,09 °C bij een gereduceerd FOV. Deze nieuwe oplossing biedt hierdoor twee zeer belangrijke technische verbeteringen. Ten eerste, in de huidige state-of-the-art, stopt de watercirculatie tijdens de MR-beeldvorming. Hierdoor wordt de huidkoeling tijdens de hyperthermiebehandeling onderbroken, met als gevolg een lager comfort van de patiënt. Bij continue koeling blijft het comfort van de patiënt behouden en wordt de tolerantie van de patiënt voor hyperthermiebehandeling verhoogd. Ten tweede vermindert de reductie van FOV de MRI scantijd, alsook signaaldegradatie als gevolg van gedeeltelijke volume-effecten waardoor de resolutie verbetert. Elk afzonderlijk effect is cruciaal voor het vergrote van de nauwkeurigheid van de MR-thermometrie. Daarom concluderen we dat Fe_3O_4 gedoteerde waterbolus een aanzienlijk potentieel heeft om de monitoring van de RF-hyperthermiebehandeling te verbeteren onder sturing van MRT.

Significante verbeteringen kunnen worden aangebracht in SNR door het gebruik van MR-spoelen dicht op de huid. Hoofdstuk 8 laat het onderzoek zien dat is gedaan naar de integratie van de spoelen in de MRcollar. Voorafgaand aan de integratie van de spoelen in de MRcollar hebben we een vlakke opstelling van beperkte omvang ontworpen: een twee kanaals MR-ontvangstspoel geïntegreerd met twee RF-hyperthermia applicatoren. In deze beperkte opstelling worden alle relevante interacties tussen de twee RF-systemen (MRI en hyperthermie) gerealiseerd. Met dit experiment wordt aangetoond dat de geïntegreerde MR-ontvangstspoelen geen invloed hebben op de verwarmingspatronen van de in hoofdstuk 4 ontworpen antennemodules. Het MR-thermomerie signaal gemeten met de oppervlakte spoelen heeft een SNR dat 17% hoger is dan gemeten met de lichaamsspoel (body-coil) van de MR. De interactie tussen de hyperthermie applicatoren en de geïntegreerde MR-ontvangstspoelen is zeer laag (-56 dB). Uiteraard, blijft het voor de bescherming van de MRI-elektronica noodzakelijk om het hoog RF-vermogen voor de weefselverwarming goed te scheiden van de ontvangers van de MRI-scanner, die slechts een laag vermogen aan kunnen.

In de afgelopen decennia is aanzienlijke vooruitgang geboekt in de behandeling van hoofd-hals tumoren met hyperthermie en voor andere gebieden hyperthermie onder MRT-geleide. In het hier gepresenteerde onderzoek hebben we essentiële hulpmiddelen ontwikkeld om MRT geleide hyperthermie ook mogelijk te maken tijdens hyperthermie van hoofd-hals tumoren met de MRcollar, een nieuwe waterbolusoplossing en geïntegreerde MR-coils. We verwachten dat de nieuwe verbeteringen zoals ontwikkeld in dit proefschrift nauwkeurige thermische dosimetrie tijdens de MR-geleide hyperthermiebehandeling van hoofd-hals tumoren mogelijk maakt en uiteindelijk leidt tot een betere behandeling met nauwkeurige thermische modellen. Daarnaast kunnen de gevonden resultaten, zoals bijvoorbeeld naar de optimale waterboluseigenschappen en de integratie van oppervlaktespoelen, ook worden uitgevoerd bij andere hyperthermie-apparaten die bedoeld zijn voor gebruik op andere plaatsen in het lichaam dan hoofd en nek.

References

1. World Health Organization, "Cancer," *World Health Organization*, 2018.

2. Global Cancer Observatory, "Cancer today, estimated number of new cases in 2018, worldwide, both sexes, all ages," *Global Cancer Observatory*, 2020.

3. J. D. Cramer, B. Burtness, Q. T. Le, and R. L. Ferris, "The changing therapeutic landscape of head and neck cancer," *Nature Reviews Clinical Oncology*, vol. 16, no. 11, pp. 669–683, 2019.

4. A. Wyss, M. Hashibe, S.-C. Chuang, Y.-C. A. Lee, Z.-F. Zhang, G.-P. Yu, D. M. Winn, Q. Wei, R. Talamini, and N. Szeszenia-Dabrowska, "Cigarette, cigar, and pipe smoking and the risk of head and neck cancers: pooled analysis in the international head and neck cancer epidemiology consortium," *American journal of epidemiology*, vol. 178, no. 5, pp. 679–690, 2013.

5. H. Maier, A. Dietz, U. Gewelke, W. D. Heller, and H. Weidauer, "Tobacco and alcohol and the risk of head and neck cancer," *The clinical investigator*, vol. 70, no. 3-4, pp. 320–327, 1992.

6. L. Q. M. Chow, "Head and neck cancer," *New England Journal of Medicine*, vol. 382, no. 1, pp. 60–72, 2020.

7. M. C. Ward, N. Riaz, J. J. Caudell, N. E. Dunlap, D. Isrow, S. J. Zakem, J. Dault, M. J. Awan, J. A. Vargo, and D. E. Heron, "Refining patient selection for reirradiation of head and neck squamous carcinoma in the imrt era: a multi-institution cohort study by the miri collaborative," *International Journal of Radiation Oncology* Biology* Physics*, vol. 100, no. 3, pp. 586–594, 2018.

8. J. K. Kim, J. E. Leeman, N. Riaz, S. McBride, C. J. Tsai, and N. Y. Lee, "Proton therapy for head and neck cancer," *Current treatment options in oncology*, vol. 19, no. 6, p. 28, 2018.

9. S. B. Chinn and J. N. Myers, "Oral cavity carcinoma: current management, controversies, and future directions," *Journal of clinical oncology*, vol. 33, no. 29, p. 3269, 2015.

10. Y. S. Kim, "Reirradiation of head and neck cancer in the era of intensity-modulated radiotherapy: patient selection, practical aspects, and current evidence," *Radiation oncology journal*, vol. 35, no. 1, p. 1, 2017.

11. M. Franckena, L. J. A. Stalpers, P. C. M. Koper, R. G. J. Wiggenraad, W. J. Hoogenraad, J. D. P. van Dijk, C. C. Wárlám-Rodenhuis, J. J. Jobsen, G. C. van Rhoon, and J. van der Zee, "Long-term improvement in treatment outcome after radiotherapy and hyperthermia in locoregionally advanced cervix cancer: an update of the dutch deep hyperthermia trial," *International Journal of Radiation Oncology* Biology* Physics*, vol. 70, no. 4, pp. 1176–1182, 2008.

12. E. L. Jones, J. R. Oleson, L. R. Prosnitz, T. V. Samulski, Z. Vujaskovic, D. Yu, L. L. Sanders, and M. W. Dewhirst, "Randomized trial of hyperthermia and radiation for superficial tumors," *Journal of Clinical Oncology*, vol. 23, no. 13, pp. 3079–3085, 2005.

13. J. van der Zee, D. González González, G. C. van Rhoon, J. D. van Dijk, W. L. van Putten, and A. A. Hart, "Dutch deep hyperthermia group. comparison of radiotherapy alone with radiotherapy plus hyperthermia in locally advanced pelvic tumours: a prospective, randomised, multicentre trial," *Lancet*, vol. 355, no. 9210, pp. 1119–1125, 2000.

14. J. Overgaard, "The heat is (still) onthe past and future of hyperthermic radiation oncology," *Radiotherapy and Oncology*, vol. 109, no. 2, pp. 185–187, 2013.

15. P. Wust, B. Hildebrandt, G. Sreenivasa, B. Rau, J. Gellermann, H. Riess, R. Felix, and P. M. Schlag, "Hyperthermia in combined treatment of cancer," *The lancet oncology*, vol. 3, no. 8, pp. 487–497, 2002.

16. N. R. Datta, H. P. Kok, H. Crezee, U. S. Gaipl, and S. Bodis, "Integrating loco-regional hyperthermia into the current oncology practice: Swot and tows analyses," *Frontiers in Oncology*, vol. 10, 2020.

17. R. Issels, E. Kampmann, R. Kanaar, and L. H. Lindner, "Hallmarks of hyperthermia in driving the future of clinical hyperthermia as targeted therapy: translation into clinical application," *International Journal of Hyperthermia*, vol. 32, no. 1, pp. 89–95, 2016.

18. J. C. Peeken, P. Vaupel, and S. E. Combs, "Integrating hyperthermia into modern radiation oncology: what evidence is necessary?," *Frontiers in oncology*, vol. 7, p. 132, 2017.

19. M. B. Schaaf, A. D. Garg, and P. Agostinis, "Defining the role of the tumor vasculature in antitumor immunity and immunotherapy," *Cell death & disease*, vol. 9, no. 2, pp. 1–14, 2018.

20. P. B. Elming, B. S. Sørensen, A. L. Oei, N. A. P. Franken, J. Crezee, J. Overgaard, and M. R. Horsman, "Hyperthermia: the optimal treatment to overcome radiation resistant hypoxia," *Cancers*, vol. 11, no. 1, p. 60, 2019.

21. P. Vaupel, F. Kallinowski, and P. Okunieff, "Blood flow, oxygen and nutrient supply, and metabolic microenvironment of human tumors: a review," *Cancer research*, vol. 49, no. 23, pp. 6449–6465, 1989.

22. M. R. Horsman, "Angiogenesis and vascular targeting: relevance for hyperthermia," *International journal of hyperthermia*, vol. 24, no. 1, pp. 57–65, 2008.

23. C. W. Song, A. Lokshina, J. G. Rhee, M. Patten, and S. H. Levitt, "Implication of blood flow in hyperthermic treatment of tumors," *IEEE Transactions on Biomedical Engineering*, no. 1, pp. 9–16, 1984.

24. Z. Vujaskovic and C. W. Song, "Physiological mechanisms underlying heat-induced radiosensitization," *International Journal of Hyperthermia*, vol. 20, no. 2, pp. 163–174, 2004.

25. M. W. Dewhirst, C.-T. Lee, and K. A. Ashcraft, "The future of biology in driving the field of hyperthermia," *International Journal of Hyperthermia*, vol. 32, no. 1, pp. 4–13, 2016.

26. R. D. Issels, "Hyperthermia adds to chemotherapy," *European journal of cancer*, vol. 44, no. 17, pp. 2546–2554, 2008.

27. H. H. Kampinga and E. Dikomey, "Hyperthermic radiosensitization: mode of action and clinical relevance," *International journal of radiation biology*, vol. 77, no. 4, pp. 399–408, 2001.

28. J. M. C. Bull, "A review of immune therapy in cancer and a question: can thermal therapy increase tumor response?," *International Journal of Hyperthermia*, vol. 34, no. 6, pp. 840–852, 2018.

29. P. Bichel and J. Overgaard, "Hyperthermic effect on exponential and plateau ascites tumor cells in vitro dependent on environmental ph," *Radiation research*, vol. 70, no. 2, pp. 449–454, 1977.

30. P. M. Krawczyk, B. Eppink, J. Essers, J. Stap, H. Rodermond, H. Odijk, A. Zelensky, C. van Bree, L. J. Stalpers, and M. R. Buist, "Mild hyperthermia inhibits homologous recombination, induces brca2 degradation, and sensitizes cancer cells to poly (adp-ribose) polymerase-1 inhibition," *Proceedings of the National Academy of Sciences*, vol. 108, no. 24, pp. 9851–9856, 2011.

31. C. Zhao, J. Chen, B. Yu, and X. Chen, "Improvement in quality of life in patients with nasopharyngeal carcinoma treated with non-invasive extracorporeal radiofrequency

in combination with chemoradiotherapy," *International Journal of Radiation Biology*, vol. 90, no. 10, pp. 853–858, 2014.

32. Y. Hua, S. Ma, Z. Fu, Q. Hu, L. E. I. Wang, and Y. Piao, "Intracavity hyperthermia in nasopharyngeal cancer: a phase iii clinical study," *International Journal of Hyperthermia*, vol. 27, no. 2, pp. 180–186, 2011.

33. N. G. Huilgol, S. Gupta, and C. R. Sridhar, "Hyperthermia with radiation in the treatment of locally advanced head and neck cancer: a report of randomized trial," *Journal of cancer research and therapeutics*, vol. 6, no. 4, p. 492, 2010.

34. R. Valdagni and M. Amichetti, "Report of long-term follow-up in a randomized trial comparing radiation therapy and radiation therapy plus hyperthermia to metastatic lymphnodes in stage iv head and neck patients," *International Journal of Radiation Oncology* Biology* Physics*, vol. 28, no. 1, pp. 163–169, 1994.

35. R. Valdagni, M. Amichetti, and G. Pani, "Radical radiation alone versus radical radiation plus microwave hyperthermia for n3 (tnm-uicc) neck nodes: a prospective randomized clinical trial," *International Journal of Radiation Oncology* Biology* Physics*, vol. 15, no. 1, pp. 13–24, 1988.

36. N. R. Datta, A. K. Bose, H. K. Kapoor, and S. Gupta, "Head and neck cancers: results of thermoradiotherapy versus radiotherapy," *International Journal of Hyperthermia*, vol. 6, no. 3, pp. 479–486, 1990.

37. M. Kang, W.-Q. Liu, Y.-T. Qin, Z.-X. Wei, and R.-S. Wang, "Long-term efficacy of microwave hyperthermia combined with chemoradiotherapy in treatment of nasopharyngeal carcinoma with cervical lymph node metastases," *Asian Pac J Cancer Prev*, vol. 14, no. 12, pp. 7395–400, 2013.

38. N. R. Datta, S. Rogers, S. G. Ordóñez, E. Puric, and S. Bodis, "Hyperthermia and radiotherapy in the management of head and neck cancers: A systematic review and meta-analysis," *International Journal of Hyperthermia*, vol. 32, no. 1, pp. 31–40, 2016.

39. M. M. Paulides, H. D. Trefna, S. Curto, and D. B. Rodrigues, "Recent technological advancements in radiofrequency-and microwave-mediated hyperthermia for enhancing drug delivery," *Advanced Drug Delivery Reviews*, 2020.

40. H. P. Kok, E. N. K. Cressman, W. Ceelen, C. L. Brace, R. Ivkov, H. Grüll, G. Ter Haar, P. Wust, and J. Crezee, "Heating technology for malignant tumors: a review," *International Journal of Hyperthermia*, vol. 37, no. 1, pp. 711–741, 2020.

41. M. M. Paulides, J. F. Bakker, E. Neufeld, J. v. d. Zee, P. P. Jansen, P. C. Levendag, and G. C. Van Rhoon, "The hypercollar: a novel applicator for hyperthermia in the head and neck," *International Journal of Hyperthermia*, vol. 23, no. 7, pp. 567–576, 2007.

42. G. M. Verduijn, E. M. de Wee, Z. Rijnen, P. Togni, J. A. U. Hardillo, I. Ten Hove, M. Franckena, G. C. van Rhoon, and M. M. Paulides, "Deep hyperthermia with the hypercollar system combined with irradiation for advanced head and neck carcinomaa feasibility study," *International Journal of Hyperthermia*, vol. 34, no. 7, pp. 994–1001, 2018.

43. P. Togni, Z. Rijnen, W. C. M. Numan, R. F. Verhaart, J. F. Bakker, G. C. Van Rhoon, and M. M. Paulides, "Electromagnetic redesign of the hypercollar applicator: toward improved deep local head-and-neck hyperthermia," *Physics in Medicine and Biology*, vol. 58, no. 17, p. 5997, 2013.

44. Z. Rijnen, P. Togni, R. Roskam, S. G. Van De Geer, R. H. M. Goossens, and M. M. Paulides, "Quality and comfort in head and neck hyperthermia: a redesign according to clinical experience and simulation studies," *International Journal of Hyperthermia*, vol. 31, no. 8, pp. 823–830, 2015.

45. M. M. Paulides, G. M. Verduijn, and N. Van Holthe, "Status quo and directions in deep head and neck hyperthermia," *Radiation Oncology*, vol. 11, no. 1, p. 21, 2016.

46. M. Sherar, F.-F. Liu, M. Pintilie, W. Levin, J. Hunt, R. Hill, J. Hand, C. Vernon, G. van Rhoon, and J. van der Zee, "Relationship between thermal dose and outcome in thermoradiotherapy treatments for superficial recurrences of breast cancer: data from a phase iii trial," *International Journal of Radiation Oncology* Biology* Physics*, vol. 39, no. 2, pp. 371–380, 1997.

47. M. Franckena, D. Fatehi, M. de Bruijne, R. A. M. Canters, Y. van Norden, J. W. Mens, G. C. van Rhoon, and J. Van Der Zee, "Hyperthermia dose-effect relationship in 420 patients with cervical cancer treated with combined radiotherapy and hyperthermia," *European Journal of Cancer*, vol. 45, no. 11, pp. 1969–1978, 2009.

48. M. Kroesen, H. T. Mulder, J. M. L. van Holthe, A. A. Aangeenbrug, J. W. M. Mens, H. C. van Doorn, M. M. Paulides, E. Oomen-de Hoop, R. M. Vernhout, and L. C. Lutgens, "Confirmation of thermal dose as a predictor of local control in cervical carcinoma patients treated with state-of-the-art radiation therapy and hyperthermia," *Radiotherapy and Oncology*, vol. 140, pp. 150–158, 2019.

49. A. Bakker, J. van der Zee, G. van Tienhoven, H. P. Kok, C. R. N. Rasch, and H. Crezee, "Temperature and thermal dose during radiotherapy and hyperthermia for recurrent breast cancer are related to clinical outcome and thermal toxicity: a systematic review," *International Journal of Hyperthermia*, vol. 36, no. 1, pp. 1023–1038, 2019.

50. S. A. Sapareto and W. C. Dewey, "Thermal dose determination in cancer therapy," *International Journal of Radiation Oncology Biology Physics*, vol. 10, no. 6, pp. 787–800, 1984.

51. P. R. Stauffer, "Evolving technology for thermal therapy of cancer," *International Journal of Hyperthermia*, vol. 21, no. 8, pp. 731–744, 2005.

52. Z. Rijnen, J. F. Bakker, R. A. M. Canters, P. Togni, G. M. Verduijn, P. C. Levendag, G. C. Van Rhoon, and M. M. Paulides, "Clinical integration of software tool vedo for adaptive and quantitative application of phased array hyperthermia in the head and neck," *International journal of Hyperthermia*, vol. 29, no. 3, pp. 181–193, 2013.

53. V. Fortunati, R. F. Verhaart, W. J. Niessen, J. F. Veenland, M. M. Paulides, and T. van Walsum, "Automatic tissue segmentation of head and neck mr images for hyperthermia treatment planning," *Physics in Medicine and Biology*, vol. 60, no. 16, p. 6547, 2015.

54. R. F. Verhaart, V. Fortunati, G. M. Verduijn, T. van Walsum, J. F. Veenland, and M. M. Paulides, "Ct-based patient modeling for head and neck hyperthermia treatment planning: Manual versus automatic normal-tissue-segmentation," *Radiotherapy and Oncology*, vol. 111, no. 1, pp. 158–163, 2014.

55. M. M. Paulides, P. R. Stauffer, E. Neufeld, P. F. Maccarini, A. Kyriakou, R. A. M. Canters, C. J. Diederich, J. F. Bakker, and G. C. Van Rhoon, "Simulation techniques in hyperthermia treatment planning," *International Journal of Hyperthermia*, vol. 29, no. 4, pp. 346–357, 2013.

56. R. A. M. Canters, M. Franckena, J. van der Zee, and G. C. Van Rhoon, "Complaint-adaptive power density optimization as a tool for htp-guided steering in deep hyperthermia treatment of pelvic tumors," *Physics in Medicine and Biology*, vol. 53, no. 23, p. 6799, 2008.

57. J. van der Zee, J. N. Peer-Valstar, P. J. M. Rietveld, L. de Graaf-Strukowska, and G. C. van Rhoon, "Practical limitations of interstitial thermometry during deep hyperthermia," *International Journal of Radiation Oncology* Biology* Physics*, vol. 40, no. 5, pp. 1205–1212, 1998.

58. G. C. Van Rhoon and P. Wust, "Introduction: non-invasive thermometry for thermotherapy," *International Journal of Hyperthermia*, vol. 21, no. 6, pp. 489–495, 2005.

59. G. C. van Rhoon, "Is cem43 still a relevant thermal dose parameter for hyperthermia treatment monitoring?," *International Journal of Hyperthermia*, vol. 32, no. 1, pp. 50–62, 2016.

60. H. P. Kok, J. Crezee, N. A. P. Franken, L. J. A. Stalpers, G. W. Barendsen, and A. Bel, "Quantifying the combined effect of radiation therapy and hyperthermia in terms of equivalent dose distributions," *International Journal of Radiation Oncology* Biology* Physics*, vol. 88, no. 3, pp. 739–745, 2014.

61. M. M. Paulides, J. F. Bakker, L. W. Hofstetter, W. C. M. Numan, R. Pellicer, E. W. Fiveland, M. Tarasek, G. C. Houston, G. C. Van Rhoon, D. T. B. Yeo, and G. Kotek, "Laboratory

prototype for experimental validation of mr-guided radiofrequency head and neck hyperthermia," *Physics in Medicine and Biology*, vol. 59, no. 9, pp. 2139–2154, 2014.

62. M. W. Dewhirst, Z. Vujaskovic, E. Jones, and D. Thrall, "Re-setting the biologic rationale for thermal therapy," *International Journal of Hyperthermia*, vol. 21, no. 8, pp. 779–790, 2005.

63. L. ER, *Electromagnetic Superficial Heating Technology*, p. 193217. Berlin, Heidelberg: Springer Verlag, 1995.

64. P. Wust, M. Seebass, J. Nadobny, and R. Felix, *Electromagnetic deep heating technology*, p. 219251. Berlin: Springer Verlag, 1995.

65. N. R. Datta, E. Puric, D. Klingbiel, S. Gomez, and S. Bodis, "Hyperthermia and radiation therapy in locoregional recurrent breast cancers: A systematic review and meta-analysis," *International Journal of Radiation Oncology Biology Physics*, vol. 94, no. 5, pp. 1073–1087, 2016.

66. N. R. Datta, S. Rogers, D. Klingbiel, S. Gómez, E. Puric, and S. Bodis, "Hyperthermia and radiotherapy with or without chemotherapy in locally advanced cervical cancer: a systematic review with conventional and network meta-analyses," *International Journal of Hyperthermia*, vol. 32, no. 7, pp. 809–821, 2016.

67. N. R. Datta, S. Rogers, S. G. Ordóñez, E. Puric, and S. Bodis, "Hyperthermia and radiotherapy in the management of head and neck cancers: A systematic review and meta-analysis," *International Journal of Hyperthermia*, vol. 32, no. 1, pp. 31–40, 2016.

68. J. R. Oleson, M. W. Dewhirst, J. M. Harrelson, K. A. Leopold, T. V. Samulski, and C. Y. Tso, "Tumor temperature distributions predict hyperthermia effect," *International Journal of Radiation Oncology, Biology, Physics*, vol. 16, no. 3, pp. 559–570, 1989.

69. R. D. Issels, S. W. Prenninger, A. Nagele, E. Boehm, H. Sauer, K. W. Jauch, H. Denecke, H. Berger, K. Peter, and W. Wilmanns, "Ifosfamide plus etoposide combined with regional hyperthermia in patients with locally advanced sarcomas: A phase ii study," *Journal of Clinical Oncology*, vol. 8, no. 11, pp. 1818–1829, 1990.

70. K. A. Leopold, M. W. Dewhirst, T. V. Samulski, R. K. Dodge, S. L. George, J. L. Blivin, L. R. Prosnitz, and J. R. Oleson, "Cumulative minutes with t90 greater than tempindex is predictive of response of superficial malignancies to hyperthermia and radiation," *International Journal of Radiation Oncology, Biology, Physics*, vol. 25, no. 5, pp. 841–847, 1993.

71. B. Hildebrandt, P. Wust, O. Ahlers, A. Dieing, G. Sreenivasa, T. Kerner, R. Felix, and H. Riess, "The cellular and molecular basis of hyperthermia," *Critical Reviews in Oncology/Hematology*, vol. 43, no. 1, pp. 33–56, 2002.

72. N. Cihoric, A. Tsikkinis, G. van Rhoon, H. Crezee, D. M. Aebersold, S. Bodis, M. Beck, J. Nadobny, V. Budach, and P. Wust, "Hyperthermia-related clinical trials on cancer treatment within the clinicaltrials. gov registry," *International journal of hyperthermia*, vol. 31, no. 6, pp. 609–614, 2015.

73. R. D. Issels, L. H. Lindner, J. Verweij, R. Wessalowski, P. Reichardt, P. Wust, P. Ghadjar, P. Hohenberger, M. Angele, and C. Salat, "Effect of neoadjuvant chemotherapy plus regional hyperthermia on long-term outcomes among patients with localized high-risk soft tissue sarcoma: the eortc 62961-esho 95 randomized clinical trial," *JAMA oncology*, vol. 4, no. 4, pp. 483–492, 2018.

74. R. D. Issels, L. H. Lindner, J. Verweij, R. Wessalowski, P. Reichardt, P. Wust, P. Ghadjar, P. Hohenberger, M. Angele, C. Salat, *et al.*, "Effect of neoadjuvant chemotherapy plus regional hyperthermia on long-term outcomes among patients with localized high-risk soft tissue sarcoma: the eortc 62961-esho 95 randomized clinical trial," *JAMA oncology*, vol. 4, no. 4, pp. 483–492, 2018.

75. M. Murbach, E. Neufeld, M. Capstick, W. Kainz, D. O. Brunner, T. Samaras, K. P. Pruessmann, and N. Kuster, "Thermal tissue damage model analyzed for different whole-body sar and scan durations for standard mr body coils," *Magnetic Resonance in Medicine*, vol. 71, no. 1, pp. 421–431, 2014.

76. P. W. Vaupel and D. K. Kelleher, "Pathophysiological and vascular characteristics of tumours and their importance for hyperthermia: Heterogeneity is the key issue," *International Journal of Hyperthermia*, vol. 26, no. 3, pp. 211–223, 2010.

77. L. Winter, E. Oberacker, K. Paul, Y. Ji, C. Oezerdem, P. Ghadjar, A. Thieme, V. Budach, P. Wust, and T. Niendorf, "Magnetic resonance thermometry: methodology, pitfalls and practical solutions," *International Journal of Hyperthermia*, vol. 32, no. 1, pp. 63–75, 2016.

78. H. Odéen and D. L. Parker, "Magnetic resonance thermometry and its biological applications-physical principles and practical considerations," *Progress in nuclear magnetic resonance spectroscopy*, 2019.

79. R. R. Bowman, "A probe for measuring temperature in radio-frequency-heated material," *IEEE Transactions on Microwave Theory and Techniques*, vol. 24, no. 1, pp. 43–45, 1976.

80. D. A. Christensen, "A new nonperturbing temperature probe using semiconductor band edge shift," *Journal of bioengineering*, vol. 1, no. 5, pp. 541–545, 1977.

81. K. A. Wickersheim and R. B. Alves, "Recent advances in optical-temperature measurement," *Industrial Research and Development*, vol. 21, no. 12, pp. 82–89, 1979.

82. P. Wust, J. Gellermann, C. Harder, W. Tilly, B. Rau, S. Dinges, P. Schlag, V. Budach, and R. Felix, "Rationale for using invasive thermometry for regional hyperthermia of pelvic tumors," *International Journal of Radiation Oncology* Biology* Physics*, vol. 41, no. 5, pp. 1129–1137, 1998.

83. D. L. Parker, V. Smith, P. Sheldon, L. E. Crooks, and L. Fussell, "Temperature distribution measurements in two-dimensional nmr imaging," *Medical physics*, vol. 10, no. 3, pp. 321–325, 1983.

84. J. De Poorter, C. De Wagter, Y. De Deene, C. Thomsen, F. Ståhlberg, and E. Achten, "The proton-resonance-frequency-shift method compared with molecular diffusion for quantitative measurement of two-dimensional time-dependent temperature distribution in a phantom," *Journal of Magnetic Resonance, Series B*, vol. 103, no. 3, pp. 234–241, 1994.

85. Y. Ishihara, A. Calderon, H. Watanabe, K. Okamoto, Y. Suzuki, K. Kuroda, and Y. Suzuki, "A precise and fast temperature mapping using water proton chemical shift," *Magnetic Resonance in Medicine*, vol. 34, no. 6, pp. 814–823, 1995.

86. J. De Poorter, "Noninvasive mri thermometry with the proton-resonance frequency method - study of susceptibility effects," *Magnetic Resonance in Medicine*, vol. 34, no. 3, pp. 359–367, 1995.

87. D. Le Bihan, J. Delannoy, and R. L. Levin, "Temperature mapping with mr imaging of molecular diffusion: application to hyperthermia," *Radiology*, vol. 171, no. 3, pp. 853–857, 1989.

88. L. Lüdemann, W. Wlodarczyk, J. Nadobny, M. Weihrauch, J. Gellermann, and P. Wust, "Non-invasive magnetic resonance thermography during regional hyperthermia," *International Journal of Hyperthermia*, vol. 26, no. 3, pp. 273–282, 2010.

89. V. Rieke and K. B. Pauly, "Mr thermometry," *Journal of Magnetic Resonance Imaging*, vol. 27, no. 2, pp. 376–390, 2008.

90. P. Baron, M. Ries, R. Deckers, M. de Greef, J. Tanttu, M. Köhler, M. A. Viergever, C. T. Moonen, and L. W. Bartels, "In vivo t2-based mr thermometry in adipose tissue layers for high-intensity focused ultrasound near-field monitoring," *Magnetic resonance in medicine*, vol. 72, no. 4, pp. 1057–1064, 2014.

91. N. McDannold, "Quantitative mri-based temperature mapping based on the proton resonant frequency shift: review of validation studies," *International journal of hyperthermia*, vol. 21, no. 6, pp. 533–546, 2005.

92. J. C. Hindman, "Proton resonance shift of water in the gas and liquid states," *The Journal of Chemical Physics*, vol. 44, no. 12, pp. 4582–4592, 1966.

93. K. K. Vigen, B. L. Daniel, J. M. Pauly, and K. Butts, "Triggered, navigated, multi-baseline method for proton resonance frequency temperature mapping with respiratory motion," *Magnetic Resonance in Medicine*, vol. 50, no. 5, pp. 1003–1010, 2003.

94. V. Rieke, K. K. Vigen, G. Sommer, B. L. Daniel, J. M. Pauly, and K. Butts, "Referenceless prf shift thermometry," *Magnetic Resonance in Medicine*, vol. 51, no. 6, pp. 1223–1231, 2004.

95. J. Gellermann, W. Wlodarczyk, A. Feussner, H. Fähling, J. Nadobny, B. Hildebrandt, R. Felix, and P. Wust, "Methods and potentials of magnetic resonance imaging for monitoring radiofrequency hyperthermia in a hybrid system," *International Journal of Hyperthermia*, vol. 21, no. 6, pp. 497–513, 2005.

96. W. A. Grissom, V. Rieke, A. B. Holbrook, Y. Medan, M. Lustig, J. Santos, M. V. McConnell, and K. B. Pauly, "Hybrid referenceless and multibaseline subtraction mr thermometry for monitoring thermal therapies in moving organs," *Medical Physics*, vol. 37, no. 9, pp. 5014–5026, 2010.

97. J. Gellermann, W. Wlodarczyk, H. Ganter, J. Nadobny, H. Fähling, M. Seebass, R. Felix, and P. Wust, "A practical approach to thermography in a hyperthermia/magnetic resonance hybrid system: Validation in a heterogeneous phantom," *International Journal of Radiation Oncology* Biology* Physics*, vol. 61, no. 1, pp. 267–277, 2005.

98. J. Gellermann, M. Weihrauch, C. Cho, W. Wlodarczyk, H. Fähling, R. Felix, V. Budach, M. Weiser, J. Nadobny, and P. Wust, "Comparison of mr-thermography and planning calculations in phantoms," *Medical physics*, vol. 33, no. 10, pp. 3912–3920, 2006.

99. H. T. Mulder, S. Curto, M. M. Paulides, M. Franckena, and G. C. van Rhoon, "Systematic quality assurance of the bsd2000-3d mr-compatible hyperthermia applicator performance using mr temperature imaging," *International Journal of Hyperthermia*, 2018.

100. J. Gellermann, B. Hildebrandt, R. Issels, H. Ganter, W. Wlodarczyk, V. Budach, R. Felix, P. U. Tunn, P. Reichardt, and P. Wust, "Noninvasive magnetic resonance thermography of soft tissue sarcomas during regional hyperthermia: Correlation with response and direct thermometry," *Cancer*, vol. 107, no. 6, pp. 1373–1382, 2006.

101. J. Gellermann, W. Wlodarczyk, B. Hildebrandt, H. Ganter, A. Nicolau, B. Rau, W. Tilly, H. Fähling, J. Nadobny, R. Felix, and P. Wust, "Noninvasive magnetic resonance thermography of recurrent rectal carcinoma in a 1.5 tesla hybrid system," *Cancer Research*, vol. 65, no. 13, pp. 5872–5880, 2005.

102. M. Weihrauch, P. Wust, M. Weiser, J. Nadobny, S. Eisenhardt, V. Budach, and J. Gellermann, "Adaptation of antenna profiles for control of mr guided hyperthermia (ht) in a hybrid mrht system," *Medical physics*, vol. 34, no. 12, pp. 4717–4725, 2007.

103. J. Delannoy, D. LeBihan, D. I. Hoult, and R. L. Levin, "Hyperthermia system combined with a magnetic resonance imaging unit," *Medical Physics*, vol. 17, no. 5, pp. 855–860, 1990.

104. J. Delannoy, C. N. Chen, R. Turner, R. L. Levin, and D. Le Bihan, "Noninvasive temperature imaging using diffusion mri," *Magnetic Resonance in Medicine*, vol. 19, no. 2, pp. 333–339, 1991.

105. D. L. Carter, J. R. MacFall, S. T. Clegg, X. Wan, D. M. Prescott, H. C. Charles, and T. V. Samulski, "Magnetic resonance thermometry during hyperthermia for human high-grade sarcoma," *International Journal of Radiation Oncology Biology Physics*, vol. 40, no. 4, pp. 815–822, 1998.

106. O. I. Craciunescua, P. R. Stauffer, B. J. Soher, C. R. Wyatt, O. Arabe, P. Maccarini, S. K. Das, K. S. Cheng, T. Z. Wong, E. L. Jones, M. W. Dewhirst, Z. Vujaskovic, and J. R. MacFall, "Accuracy of real time noninvasive temperature measurements using magnetic resonance thermal imaging in patients treated for high grade extremity soft tissue sarcomas," *Medical Physics*, vol. 36, no. 11, pp. 4848–4858, 2009.

107. W. C. M. Numan, L. W. Hofstetter, G. Kotek, J. F. Bakker, E. W. Fiveland, G. C. Houston, G. Kudielka, D. T. B. Yeo, and M. M. Paulides, "Exploration of mr-guided head and neck hyperthermia by phantom testing of a modified prototype applicator for use with proton resonance frequency shift thermometry," *International Journal of Hyperthermia*, vol. 30, no. 3, pp. 184–191, 2014.

108. M. M. Paulides, J. F. Bakker, and G. C. van Rhoon, "Electromagnetic head-and-neck hyperthermia applicator: Experimental phantom verification and fdtd model," *International Journal of Radiation Oncology Biology Physics*, vol. 68, no. 2, pp. 612–620, 2007.

109. M. R. Tarasek, R. Pellicer, L. W. Hofstetter, W. C. M. Numan, J. F. Bakker, G. Kotek, P. Togni, R. F. Verhaart, E. W. Fiveland, G. C. Houston, G. C. Van Rhoon, M. M. Paulides, and D. T. B. Yeo, "Validation of mr thermometry: Method for temperature probe sensor registration accuracy in head and neck phantoms," *International Journal of Hyperthermia*, vol. 30, no. 2, pp. 142–149, 2014.

110. M. Paulides, T. Drizdal, G. Van Rhoon, and D. Yeo, "Novel applicator design for mr guided rf hyperthermia in head and neck cancers: heating performance and rf coupling," *Paris(France): International Society for Magnetic Resonance in Medicine (ISMRM)*, 2018.

111. K. S. Kim and S. Y. Lee, "Nanoparticle-mediated radiofrequency capacitive hyperthermia: A phantom study with magnetic resonance thermometry," *International Journal of Hyperthermia*, vol. 31, no. 8, pp. 831–839, 2015.

112. K. S. Kim, D. Hernandez, and S. Y. Lee, "Time-multiplexed two-channel capacitive radiofrequency hyperthermia with nanoparticle mediation," *BioMedical Engineering Online*, vol. 14, no. 1, 2015.

113. D. Hernandez, K. S. Kim, E. Michel, and S. Y. Lee, "Correction of b0 drift effects in magnetic resonance thermometry using magnetic field monitoring technique," *Concepts in Magnetic Resonance Part B: Magnetic Resonance Engineering*, vol. 46B, no. 2, pp. 81–89, 2016.

114. W. Hoffmann, K. H. Rhein, F. Wojcik, R. Noeske, F. Seifert, W. Wlodarczyk, H. Fahling, P. Wust, and H. Rinneberg, "Performance and use of current sheet antennae for rf-hyperthermia of a phantom monitored by 3 tesla mr-thermography," *International Journal of Hyperthermia*, vol. 18, no. 5, pp. 454–471, 2002.

115. J. Nadobny, W. Wlodarczyk, L. Westhoff, J. Gellermann, B. Rau, G. Monich, and P. Wust, "Development and evaluation of a three-dimensional hyperthermia applicator with water-coated antennas (wacoa)," *Medical Physics*, vol. 30, no. 8, pp. 2052–2064, 2003.

116. J. Nadobny, W. Wlodarczyk, L. Westhoff, J. Gellermann, R. Felix, and P. Wust, "A clinical water-coated antenna applicator for mr-controlled deep-body hyperthermia: A comparison of calculated and measured 3-d temperature data sets," *Ieee Transactions on Biomedical Engineering*, vol. 52, no. 3, pp. 505–519, 2005.

117. T. V. Samulski, J. Macfall, Y. Zhang, W. Grant, and C. Charles, "Non-invasive thermometry using magnetic resonance diffusion imaging: Potential for application in hyperthermic oncology," *International Journal of Hyperthermia*, vol. 8, no. 6, pp. 819–829, 1992.

118. J. R. MacFall, D. M. Prescott, H. C. Charles, and T. V. Samulski, "1h mri phase thermometry in vivo in canine brain, muscle, and tumor tissue," *Medical Physics*, vol. 23, no. 10, pp. 1775–1782, 1996.

119. J. Macfall, D. M. Prescott, E. Fullar, and T. V. Samulski, "Temperature dependence of canine brain tissue diffusion coefficient measured in vivo with magnetic resonance echo-planar imaging," *International Journal of Hyperthermia*, vol. 11, no. 1, pp. 73–86, 1995.

120. T. V. Samulski, S. T. Clegg, S. Das, J. Macfall, and D. M. Prescott, "Application of new technology in clinical hyperthermia," *International Journal of Hyperthermia*, vol. 10, no. 3, pp. 389–394, 1994.

121. B. Qiu, A. M. El-Sharkawy, V. Paliwal, P. Karmarkar, F. Gao, E. Atalar, and X. Yang, "Simultaneous radiofrequency (rf) heating and magnetic resonance (mr) thermal mapping using an intravascular mr imaging/rf heating system," *Magnetic Resonance in Medicine*, vol. 54, no. 1, pp. 226–230, 2005.

122. S. Curto, P. Faridi, T. B. Shrestha, M. Pyle, L. Maurmann, D. Troyer, S. H. Bossmann, and P. Prakash, "An integrated platform for small-animal hyperthermia investigations under ultra-high-field mri guidance," *International Journal of Hyperthermia*, vol. 34, no. 4, pp. 341–351, 2018.

123. E. A. L. Raaijmakers, R. M. C. Mestrom, K. Sumser, G. Salim, G. C. van Rhoon, J. Essers, and M. M. Paulides, "An mr-compatible antenna and application in a murine superficial hyperthermia applicator," *International Journal of Hyperthermia*, vol. 34, no. 6, pp. 697–703, 2018.

124. M. M. Paulides, R. M. C. Mestrom, G. Salim, B. B. Adela, W. C. M. Numan, T. Drizdal, D. T. B. Yeo, and A. B. Smolders, "A printed yagi-uda antenna for application in magnetic resonance thermometry guided microwave hyperthermia applicators," *Physics in Medicine and Biology*, vol. 62, no. 5, pp. 1831–1847, 2017.

125. K. Sumser, A. Geerman, J. Haeck, M. Bernsen, G. C. van Rhoon, and M. M. Paulides, "Development and in vivo validation of an mr-compatible temperature controllable superficial hyperthermia applicator for small animal studies," in *2018 EMF-Med 1st World Conference on Biomedical Applications of Electromagnetic Fields (EMF-Med)*, pp. 1–2, IEEE, 2018.

126. M. E. Kowalski, B. Behnia, A. G. Webb, and J. M. Jin, "Optimization of electromagnetic phased-arrays for hyperthermia via magnetic resonance temperature estimation," *IEEE Transactions on Biomedical Engineering*, vol. 49, no. 11, pp. 1229–1241, 2002.

127. M. E. Kowalski and J. M. Jin, "Model-based optimization of phased arrays for electromagnetic hyperthermia," *IEEE Transactions on Microwave Theory and Techniques*, vol. 52, no. 8 II, pp. 1964–1977, 2004.

128. D. Yeo, X. Yang, J. Wu, L. W. Hofstetter, J. E. Piel, E. W. Fiveland, K. J. Park, and T. K. Foo, "Investigation of a dual-function applicator for rf hyperthermia and mri," *Proc of Inter Soc for Magn Reson in Med (ISMRM)*, 2011.

129. L. Winter, C. Özerdem, W. Hoffmann, D. Santoro, A. Müller, H. Waiczies, R. Seemann, A. Graessl, P. Wust, and T. Niendorf, "Design and evaluation of a hybrid radiofrequency applicator for magnetic resonance imaging and rf induced hyperthermia: Electromagnetic field simulations up to 14.0 tesla and proof-of-concept at 7.0 tesla," *PLoS ONE*, vol. 8, no. 4, 2013.

130. L. Winter, C. Oezerdem, W. Hoffmann, T. van de Lindt, J. Periquito, Y. Ji, P. Ghadjar, V. Budach, P. Wust, and T. Niendorf, "Thermal magnetic resonance: Physics considerations and electromagnetic field simulations up to 23.5 tesla (1ghz)," *Radiation Oncology*, vol. 10, no. 1, 2015.

131. B. Guérin, J. F. Villena, A. G. Polimeridis, E. Adalsteinsson, L. Daniel, J. K. White, B. R. Rosen, and L. L. Wald, "Computation of ultimate sar amplification factors for

radiofrequency hyperthermia in non-uniform body models: impact of frequency and tumour location," *International Journal of Hyperthermia*, vol. 34, no. 1, pp. 87–100, 2018.

132. K. Demura, S. Morikawa, K. Murakami, K. Sato, H. Shiomi, S. Naka, Y. Kurumi, T. Inubushi, and T. Tani, "An easy-to-use microwave hyperthermia system combined with spatially resolved mr temperature maps: Phantom and animal studies," *Journal of Surgical Research*, vol. 135, no. 1, pp. 179–186, 2006.

133. A. International, "Astm f2052-15: Standard test method for measurement of magnetically induced displacement force on medical devices in the magnetic resonance environment," *West Conshohocken, Pa: ASTM International*, 2015.

134. A. International, "F2213-17, standard test method for measurement of magnetically induced torque on medical devices in the magnetic resonance environment.," 2017.

135. I. A, "Astm f2182–11a standard test method for measurement of radio frequency induced heating on or near passive implants during magnetic resonance imaging," 2011.

136. I. . 2018, "Assessment of the safety of magnetic resonance imaging for patients with an active implantable medical device," 2018.

137. O. Dietrich, J. G. Raya, S. B. Reeder, M. F. Reiser, and S. O. Schoenberg, "Measurement of signal-to-noise ratios in mr images: influence of multichannel coils, parallel imaging, and reconstruction filters," *Journal of Magnetic Resonance Imaging: An Official Journal of the International Society for Magnetic Resonance in Medicine*, vol. 26, no. 2, pp. 375–385, 2007.

138. J. Sijbers, A. J. den Dekker, J. Van Audekerke, M. Verhoye, and D. Van Dyck, "Estimation of the noise in magnitude mr images," *Magnetic resonance imaging*, vol. 16, no. 1, pp. 87–90, 1998.

139. S. B. Reeder, B. J. Wintersperger, O. Dietrich, T. Lanz, A. Greiser, M. F. Reiser, G. M. Glazer, and S. O. Schoenberg, "Practical approaches to the evaluation of signal-to-noise ratio performance with parallel imaging: application with cardiac imaging and a 32-channel cardiac coil," *Magnetic Resonance in Medicine: An Official Journal of the International Society for Magnetic Resonance in Medicine*, vol. 54, no. 3, pp. 748–754, 2005.

140. P. Kellman and E. R. McVeigh, "Image reconstruction in snr units: a general method for snr measurement," *Magnetic resonance in medicine*, vol. 54, no. 6, pp. 1439–1447, 2005.

141. M. Jafar, Y. M. Jafar, C. Dean, and M. E. Miquel, "Assessment of geometric distortion in six clinical scanners using a 3d-printed grid phantom," *Journal of Imaging*, vol. 3, no. 3, p. 28, 2017.

142. D. Wang and D. M. Doddrell, “Geometric distortion in structural magnetic resonance imaging,” *Current Medical Imaging*, vol. 1, no. 1, pp. 49–60, 2005.

143. J. Tan, C. Mougenot, S. Pichardo, J. M. Drake, and A. C. Waspe, “Motion compensation using principal component analysis and projection onto dipole fields for abdominal magnetic resonance thermometry,” *Magnetic resonance in medicine*, vol. 81, no. 1, pp. 195–207, 2019.

144. B. D. de Senneville, C. Mougenot, B. Quesson, I. Dragonu, N. Grenier, and C. T. W. Moonen, “Mr thermometry for monitoring tumor ablation,” *European radiology*, vol. 17, no. 9, pp. 2401–2410, 2007.

145. P. Bour, V. Ozenne, F. Marquet, B. D. de Senneville, E. Dumont, and B. Quesson, “Evaluation of 2d simultaneous multi-slice epi at 1.5 t for mr-thermometry in presence of motion,” 2018.

146. G. Schaefers and A. Melzer, “Testing methods for mr safety and compatibility of medical devices,” *Minimally invasive therapy and allied technologies*, vol. 15, no. 2, pp. 71–75, 2006.

147. P. Wust, H. Fähling, W. Wlodarczyk, M. Seebass, J. Gellermann, P. Deuflhard, and J. Nadobny, “Antenna arrays in the sigmaeye applicator: Interactions and transforming networks,” *Medical Physics*, vol. 28, no. 8, pp. 1793–1805, 2001.

148. L. I. Sacolick, F. Wiesinger, I. Hancu, and M. W. Vogel, “B1 mapping by blochsiegert shift,” *Magnetic resonance in medicine*, vol. 63, no. 5, pp. 1315–1322, 2010.

149. M. Amichetti, M. Romano, L. Busana, A. Bolner, G. Fellin, G. Pani, L. Tomio, and R. Valdagni, “Hyperfractionated radiation in combination with local hyperthermia in the treatment of advanced squamous cell carcinoma of the head and neck: a phase iii study,” *Radiotherapy and oncology*, vol. 45, no. 2, pp. 155–158, 1997.

150. N. G. Huilgol, S. Gupta, and R. Dixit, “Chemoradiation with hyperthermia in the treatment of head and neck cancer,” *International Journal of Hyperthermia*, vol. 26, no. 1, pp. 21–25, 2010.

151. D. E. Thrall, R. L. Page, M. W. Dewhirst, R. E. Meyer, P. J. Hoopes, and J. N. Kornegay, “Temperature measurements in normal and tumor tissue of dogs undergoing whole body hyperthermia,” *Cancer research*, vol. 46, no. 12 Part 1, pp. 6229–6235, 1986.

152. H. P. Kok, A. Kotte, and J. Crezee, “Planning, optimisation and evaluation of hyperthermia treatments,” *International Journal of Hyperthermia*, vol. 33, no. 6, pp. 593–607, 2017.

153. V. Fortunati, R. F. Verhaart, F. van der Lijn, W. J. Niessen, J. F. Veenland, M. M. Paulides, and T. van Walsum, “Tissue segmentation of head and neck ct images for treatment

planning: a multiatlas approach combined with intensity modeling," *Medical physics*, vol. 40, no. 7, p. 071905, 2013.

154. R. F. Verhaart, G. M. Verduijn, V. Fortunati, Z. Rijnen, T. van Walsum, J. F. Veenland, and M. M. Paulides, "Accurate 3d temperature dosimetry during hyperthermia therapy by combining invasive measurements and patient-specific simulations," *International Journal of Hyperthermia*, vol. 31, no. 6, pp. 686–692, 2015.

155. H. H. Pennes, "Analysis of tissue and arterial blood temperatures in the resting human forearm," *Journal of applied physiology*, vol. 1, no. 2, pp. 93–122, 1948.

156. J. Crezee and J. J. W. Lagendijk, "Temperature uniformity during hyperthermia: the impact of large vessels," *Physics in Medicine and Biology*, vol. 37, no. 6, pp. 1321–1337, 1992.

157. C. A. T. Van den Berg, J. B. Van de Kamer, A. A. C. De Leeuw, C. R. Jeukens, B. W. Raaymakers, M. van Vulpen, and J. J. W. Lagendijk, "Towards patient specific thermal modelling of the prostate," *Physics in Medicine and Biology*, vol. 51, no. 4, p. 809, 2006.

158. J. W. Mitchell and G. E. Myers, "An analytical model of the counter-current heat exchange phenomena," *Biophysical journal*, vol. 8, no. 8, pp. 897–911, 1968.

159. J. J. W. Lagendijk, "The influence of bloodflow in large vessels on the temperature distribution in hyperthermia," *Physics in Medicine and Biology*, vol. 27, no. 1, pp. 17–23, 1982.

160. M. C. Kolios, M. D. Sherar, and J. W. Hunt, "Large blood vessel cooling in heated tissues: a numerical study," *Physics in Medicine and Biology*, vol. 40, no. 4, pp. 477–494, 1995.

161. L. Zhu, L. X. Xu, Q. He, and S. Weinbaum, "A new fundamental bioheat equation for muscle tissuepart ii: temperature of sav vessels," *Journal of biomechanical engineering*, vol. 124, no. 1, pp. 121–132, 2002.

162. H. P. Kok, J. Gellermann, C. A. T. van den Berg, P. R. Stauffer, J. W. Hand, and J. Crezee, "Thermal modelling using discrete vasculature for thermal therapy: a review," *International Journal of Hyperthermia*, vol. 29, no. 4, pp. 336–345, 2013.

163. A. Kotte, G. van Leeuwen, J. de Bree, J. van der Koijk, H. Crezee, and J. Lagendijk, "A description of discrete vessel segments in thermal modelling of tissues," *Physics in Medicine and Biology*, vol. 41, no. 5, pp. 865–884, 1996.

164. A. Kotte, G. M. J. Van Leeuwen, and J. J. W. Lagendijk, "Modelling the thermal impact of a discrete vessel tree," *Physics in Medicine and Biology*, vol. 44, no. 1, pp. 57–74, 1999.

165. G. M. J. Van Leeuwen, A. Kotte, J. De Bree, J. F. Van der Koijk, J. Crezee, and J. J. W. Lagendijk, "Accuracy of geometrical modelling of heat transfer from tissue to blood vessels," *Physics in Medicine and Biology*, vol. 42, no. 7, pp. 1451–1460, 1997.

166. G. M. J. Van Leeuwen, A. Kotte, J. Crezee, and J. J. W. Lagendijk, "Tests of the geometrical description of blood vessels in a thermal model using counter-current geometries," *Physics in Medicine and Biology*, vol. 42, no. 8, pp. 1515–1532, 1997.

167. J. M. Wardlaw, F. M. Chappell, J. J. K. Best, K. Wartolowska, and E. Berry, "Non-invasive imaging compared with intra-arterial angiography in the diagnosis of symptomatic carotid stenosis: a meta-analysis," *The Lancet*, vol. 367, no. 9521, pp. 1503–1512, 2006.

168. K. K. Kumamaru, B. E. Hoppel, R. T. Mather, and F. J. Rybicki, "Ct angiography: current technology and clinical use," *Radiologic Clinics*, vol. 48, no. 2, pp. 213–235, 2010.

169. R. F. Verhaart, V. Fortunati, G. M. Verduijn, A. Lugt, T. Walsum, J. F. Veenland, and M. M. Paulides, "The relevance of mri for patient modeling in head and neck hyperthermia treatment planning: A comparison of ct and ctmri based tissue segmentation on simulated temperature," *Medical physics*, vol. 41, no. 12, pp. 123302:1–11, 2014.

170. A. M. Mendrik, E.-J. Vonken, A. Rutten, M. A. Viergever, and B. van Ginneken, "Noise reduction in computed tomography scans using 3-d anisotropic hybrid diffusion with continuous switch," *IEEE transactions on medical imaging*, vol. 28, no. 10, pp. 1585–1594, 2009.

171. C. T. Larsen, J. E. Iglesias, and K. Van Leemput, *N3 bias field correction explained as a Bayesian modeling method*, pp. 1–12. Springer, 2014.

172. L. G. Nyúl and J. K. Udupa, "New variants of a method of mri scale normalization," in *Biennial International Conference on Information Processing in Medical Imaging*, pp. 490–495, Springer, 1999.

173. V. Fortunati, R. F. Verhaart, F. Angeloni, A. Van Der Lugt, W. J. Niessen, J. F. Veenland, M. M. Paulides, and T. Van Walsum, "Feasibility of multimodal deformable registration for head and neck tumor treatment planning," *International Journal of Radiation Oncology* Biology* Physics*, vol. 90, no. 1, pp. 85–93, 2014.

174. V. Fortunati, R. F. Verhaart, F. van der Lijn, W. J. Niessen, J. F. Veenland, M. M. Paulides, and T. van Walsum, "Hyperthermia critical tissues automatic segmentation of head and neck ct images using atlas registration and graph cuts," in *Biomedical Imaging (ISBI), 2012 9th IEEE International Symposium on*, pp. 1683–1686, IEEE, 2012.

175. A. F. Frangi, W. J. Niessen, K. L. Vincken, and M. A. Viergever, "Multiscale vessel enhancement filtering," in *International conference on medical image computing and computer-assisted intervention*, pp. 130–137, Springer, 1998.

176. D. Selle, B. Preim, A. Schenk, and H. O. Peitgen, "Analysis of vasculature for liver surgical planning," *IEEE transactions on medical imaging*, vol. 21, no. 11, pp. 1344–1357, 2002.

177. C. Gabriel, S. Gabriel, and y. E. Corthout, "The dielectric properties of biological tissues: I. literature survey," *Physics in Medicine and Biology*, vol. 41, no. 11, pp. 2231–2249, 1996.

178. P. Hasgall, F. Di Gennaro, C. Baumgartner, E. Neufeld, B. Lloyd, M. Gosselin, D. Payne, K. A., and K. N., "It'is database for thermal and electromagnetic parameters of biological tissues," *Version 4.0*, 2018.

179. J. F. Bakker, M. M. Paulides, E. Neufeld, A. Christ, X. L. Chen, N. Kuster, and G. C. Van Rhoon, "Children and adults exposed to low-frequency magnetic fields at the icnirp reference levels: theoretical assessment of the induced electric fields," *Physics in Medicine and Biology*, vol. 57, no. 7, pp. 1815–1829, 2012.

180. M. D. Ford, N. Alperin, S. H. Lee, D. W. Holdsworth, and D. A. Steinman, "Characterization of volumetric flow rate waveforms in the normal internal carotid and vertebral arteries," *Physiological measurement*, vol. 26, no. 4, pp. 477–488, 2005.

181. C. D. Murray, "The physiological principle of minimum work: I. the vascular system and the cost of blood volume," *Proceedings of the National Academy of Sciences*, vol. 12, no. 3, pp. 207–214, 1926.

182. A. L. van Lier, A. N. T. J. Kotte, B. W. Raaymakers, J. J. W. Lagendijk, and C. A. T. van den Berg, "Radiofrequency heating induced by 7t head mri: thermal assessment using discrete vasculature or pennes' bioheat equation," *Journal of Magnetic Resonance Imaging*, vol. 35, no. 4, pp. 795–803, 2012.

183. V. M. M. Flyckt, B. W. Raaymakers, and J. J. W. Lagendijk, "Modelling the impact of blood flow on the temperature distribution in the human eye and the orbit: fixed heat transfer coefficients versus the pennes bioheat model versus discrete blood vessels," *Physics in Medicine and Biology*, vol. 51, no. 19, pp. 5007–5021, 2006.

184. H. P. Kok, C. A. T. Van den Berg, A. Bel, and J. Crezee, "Fast thermal simulations and temperature optimization for hyperthermia treatment planning, including realistic 3d vessel networks," *Medical physics*, vol. 40, no. 10, pp. 103303:1–15, 2013.

185. G. M. J. Van Leeuwen, A. Kotte, B. W. Raaymakers, and J. J. W. Lagendijk, "Temperature simulations in tissue with a realistic computer generated vessel network," *Physics in Medicine and Biology*, vol. 45, no. 4, p. 1035, 2000.

186. D. E. Lemons, S. Chien, L. I. Crawshaw, S. Weinbaum, and L. M. Jiji, "Significance of vessel size and type in vascular heat transfer," *American Journal of Physiology-Regulatory, Integrative and Comparative Physiology*, vol. 253, no. 1, pp. R128–R135, 1987.

187. B. W. Raaymakers, J. Crezee, and J. J. W. Lagendijk, "Modelling individual temperature profiles from an isolated perfused bovine tongue," *Physics in Medicine and Biology*, vol. 45, no. 3, pp. 765–780, 2000.

188. M. Kroesen, H. T. Mulder, N. van Holthe, A. Aangeenbrug, J. W. Mens, L. van Doorn, M. M. Paulides, E. Oomen-de Hoop, R. Vernhout, and L. Lutgens, "The effect of the time interval between radiation and hyperthermia on clinical outcome in 400 locally advanced cervical carcinoma patients," *Frontiers in oncology*, vol. 9, p. 134, 2019.

189. J. Crezee, C. M. van Leeuwen, A. L. Oei, L. E. van Heerden, A. Bel, L. J. A. Stalpers, P. Ghadjar, N. A. P. Franken, and H. P. Kok, "Biological modelling of the radiation dose escalation effect of regional hyperthermia in cervical cancer," *Radiation Oncology*, vol. 11:14, no. 1, pp. 14–23, 2016.

190. N. Datta, S. G. Ordóñez, U. Gaipl, M. Paulides, H. Crezee, J. Gellermann, D. Marder, E. Puric, and S. Bodis, "Local hyperthermia combined with radiotherapy and-/or chemotherapy: Recent advances and promises for the future," *Cancer treatment reviews*, vol. 41, no. 9, pp. 742–753, 2015.

191. P. Wust, C. H. Cho, B. Hildebrandt, and J. Gellermann, "Thermal monitoring: invasive, minimal-invasive and non-invasive approaches," *International Journal of Hyperthermia*, vol. 22, no. 3, pp. 255–262, 2006.

192. F. Adibzadeh, K. Sumser, S. Curto, D. T. B. Yeo, A. A. Shishegar, and M. M. Paulides, "Systematic review of pre-clinical and clinical devices for magnetic resonance-guided radiofrequency hyperthermia," *International Journal of Hyperthermia*, vol. 37, no. 1, pp. 15–27, 2020.

193. P. Takook, M. Persson, J. Gellermann, and H. D. Trefná, "Compact self-grounded bowtie antenna design for an uwb phased-array hyperthermia applicator," *International Journal of Hyperthermia*, vol. 33, no. 4, pp. 387–400, 2017.

194. P. Takook, M. Persson, and H. D. Trefná, "Performance evaluation of hyperthermia applicators to heat deep-seated brain tumors," *IEEE Journal of Electromagnetics, RF and Microwaves in Medicine and Biology*, vol. 2, no. 1, pp. 18–24, 2018.

195. X. Yang, J. Wu, X. Chu, T. Foo, and D. Yeo, "Characterization of a mri-rf hyperthermia dual-function coil element design," in *Proc Intl Soc Mag Reson Med*, 2011.

196. M. M. Paulides, S. H. J. A. Vossen, A. P. M. Zwamborn, and G. C. van Rhoon, "Theoretical investigation into the feasibility to deposit rf energy centrally in the head-and-neck region," *International Journal of Radiation Oncology* Biology* Physics*, vol. 63, no. 2, pp. 634–642, 2005.

197. H. T. Dobíek, J. Crezee, M. Schmidt, D. Marder, U. Lamprecht, M. Ehmann, J. Nadobny, J. Hartmann, N. Lomax, and S. Abdel-Rahman, "Quality assurance guidelines for superficial hyperthermia clinical trials: Ii. technical requirements for heating devices," *Strahlentherapie und Onkologie: Organ der Deutschen Rontgengesellschaft...[et al]*, vol. 193, no. 5, pp. 351–366, 2017.

198. G. Cappiello, T. Drizdal, B. Mc Ginley, M. OHalloran, M. Glavin, G. Van Rhoon, E. Jones, and M. Paulides, "The potential of time-multiplexed steering in phased array microwave hyperthermia for head and neck cancer treatment," *Physics in Medicine & Biology*, vol. 63, no. 13, p. 135023, 2018.

199. S. Chen, "Swarm optimization toolbox version 20130702," in *Available from: http://www.mathworks.com/matlabcentral/fileexchange/25986*, 2016.

200. J. Hoffmann, A. Henning, I. A. Giapitzakis, K. Scheffler, G. Shajan, R. Pohmann, and N. I. Avdievich, "Safety testing and operational procedures for selfdeveloped radiofrequency coils," *NMR in Biomedicine*, vol. 29, no. 9, pp. 1131–1144, 2016.

201. P. Jezzard and R. S. Balaban, "Correction for geometric distortion in echo planar images from b0 field variations," *Magnetic resonance in medicine*, vol. 34, no. 1, pp. 65–73, 1995.

202. M. M. Paulides, J. F. Bakker, N. Chavannes, and G. C. Van Rhoon, "A patch antenna design for application in a phased-array head and neck hyperthermia applicator," *IEEE Transactions on Biomedical Engineering*, vol. 54, no. 11, pp. 2057–2063, 2007.

203. T. Drizdal, M. Paulides, J. Vrba, and G. van Rhoon, "Waveguide-based applicators for superficial hyperthermia treatment: is tuning really required?," *Journal of Electromagnetic Waves and Applications*, vol. 27, no. 6, pp. 682–690, 2013.

204. K. Sumser, G. G. Bellizzi, R. Forner, T. Drizdal, J. A. H. Tamames, G. C. Van Rhoon, and M. M. Paulides, "Dual-function mr-guided hyperthermia: An innovative integrated approach and experimental demonstration of proof of principle," *IEEE Transactions on Biomedical Engineering*, 2020.

205. M. Paulides, J. Bakker, E. Neufeld, J. van der Zee, P. Jansen, P. Levendag, and G. van Rhoon, "On heating head and neck tumours using the novel clinical em applicator: The hypercollar," *International Journal of Hyperthermia*, pp. 1–18, 2007.

206. T. Drizdal, K. Sumser, G. G. Bellizzi, G. C. Van Rhoon, D. T. B. Yeo, and M. M. Paulides, "Simulation guided design of the mrcollar:a mr compatible applicator for deep heating in the head and neck region," *International Journal of Hyperthermia*, vol. Under Review, 2021.

207. K. Sumser, E. Neufeld, R. F. Verhaart, V. Fortunati, G. M. Verduijn, T. Drizdal, T. van Walsum, J. F. Veenland, and M. M. Paulides, "Feasibility and relevance of discrete vasculature modeling in routine hyperthermia treatment planning," *International Journal of Hyperthermia*, vol. 36, no. 1, pp. 800–810, 2019.

208. L. Lüdemann, W. Wlodarczyk, J. Nadobny, M. Weihrauch, J. Gellermann, and P. Wust, "Non-invasive magnetic resonance thermography during regional hyperthermia," *International Journal of Hyperthermia*, vol. 26, no. 3, pp. 273–282, 2010.

209. M. Fink, "Time reversal of ultrasonic fields. i. basic principles," *IEEE transactions on ultrasonics, ferroelectrics, and frequency control*, vol. 39, no. 5, pp. 555–566, 1992.

210. J. F. Bakker, M. M. Paulides, A. H. Westra, H. Schippers, and G. C. Van Rhoon, "Design and test of a 434 mhz multi-channel amplifier system for targeted hyperthermia applicators," *International Journal of Hyperthermia*, vol. 26, no. 2, pp. 158–170, 2010.

211. D. A. Low, W. B. Harms, S. Mutic, and J. A. Purdy, "A technique for the quantitative evaluation of dose distributions," *Medical physics*, vol. 25, no. 5, pp. 656–661, 1998.

212. M. M. Paulides, D. H. M. Wielheesen, J. Van Der Zee, and G. C. Van Rhoon, "Assessment of the local sar distortion by major anatomical structures in a cylindrical neck phantom," *International journal of hyperthermia*, vol. 21, no. 2, pp. 125–140, 2005.

213. O. M. Bucci, C. Gennarelli, and C. Savarese, "Representation of electromagnetic fields over arbitrary surfaces by a finite and nonredundant number of samples," *IEEE Transactions on Antennas and Propagation*, vol. 46, no. 3, pp. 351–359, 1998.

214. H. P. Kok, P. M. A. Van Haaren, J. B. Van de Kamer, J. Wiersma, J. D. P. Van Dijk, and J. Crezee, "High-resolution temperature-based optimization for hyperthermia treatment planning," *Physics in Medicine and Biology*, vol. 50, no. 13, p. 3127, 2005.

215. G. G. Bellizzi, T. Drizdal, G. C. van Rhoon, L. Crocco, T. Isernia, and M. M. Paulides, "The potential of constrained sar focusing for hyperthermia treatment planning: analysis for the head and neck region," *Physics in medicine and biology*, 2018.

216. G. Cappiello, B. Mc Ginley, M. A. Elahi, T. Drizdal, M. M. Paulides, M. Glavin, M. O'Halloran, and E. Jones, "Differential evolution optimization of the sar distribution for head and neck hyperthermia," *IEEE Transactions on Biomedical Engineering*, vol. 64, no. 8, pp. 1875–1885, 2017.

217. T. Köhler, P. Maass, P. Wust, and M. Seebass, "A fast algorithm to find optimal controls of multiantenna applicators in regional hyperthermia," *Physics in Medicine and Biology*, vol. 46, no. 9, p. 2503, 2001.

218. F. Adibzadeh, M. M. Paulides, and G. C. van Rhoon, "Sar thresholds for electromagnetic exposure using functional thermal dose limits," *International Journal of Hyperthermia*, vol. 34, no. 8, pp. 1248–1254, 2018.

219. H. P. Kok, P. Wust, P. R. Stauffer, F. Bardati, G. C. Van Rhoon, and J. Crezee, "Current state of the art of regional hyperthermia treatment planning: a review," *Radiation Oncology*, vol. 10, no. 1, p. 196, 2015.

220. V. Rieke and K. B. Pauly, "Echo combination to reduce proton resonance frequency (prf) thermometry errors from fat," *Journal of Magnetic Resonance Imaging*, vol. 27, no. 3, pp. 673–677, 2008.

221. S. Rieseberg, J. Frahm, and J. Finsterbusch, "Twodimensional spatiallyselective rf excitation pulses in echoplanar imaging," *Magnetic Resonance in Medicine: An Official Journal of the International Society for Magnetic Resonance in Medicine*, vol. 47, no. 6, pp. 1186–1193, 2002.

222. W. A. Grissom and S. Allen, "Reducing temperature errors in transcranial mrguided focused ultrasound using a reducedfieldofview sequence," *Magnetic Resonance in Medicine*, vol. 83, no. 3, pp. 1016–1024, 2020.

223. R. Chopra, K. Tang, M. Burtnyk, A. Boyes, L. Sugar, S. Appu, L. Klotz, and M. Bronskill, "Analysis of the spatial and temporal accuracy of heating in the prostate gland using transurethral ultrasound therapy and active mr temperature feedback," *Physics in Medicine and Biology*, vol. 54, no. 9, p. 2615, 2009.

224. S. P. Allen, T. Steeves, A. Fergusson, D. Moore, R. M. Davis, E. Vlaisialjevich, and C. H. Meyer, "Novel acoustic coupling bath using magnetite nanoparticles for mrguided transcranial focused ultrasound surgery," *Medical physics*, vol. 46, no. 12, pp. 5444–5453, 2019.

225. T. R. Nelson and S. M. Tung, "Temperature dependence of proton relaxation times in vitro," *Magnetic resonance imaging*, vol. 5, no. 3, pp. 189–199, 1987.

226. O. M. Bucci, G. Bellizzi, and G. G. Bellizzi, "Microwave broadband characterization of a diluted water-based ferrofluid in presence of a polarizing magnetic field," *IEEE Transactions on Magnetics*, vol. 53, no. 3, pp. 1–8, 2016.

227. G. B. Chavhan, P. S. Babyn, B. Thomas, M. M. Shroff, and E. M. Haacke, "Principles, techniques, and applications of t2*-based mr imaging and its special applications," *Radiographics*, vol. 29, no. 5, pp. 1433–1449, 2009.

228. R. A. M. Canters, P. Wust, J. F. Bakker, and G. C. Van Rhoon, "A literature survey on indicators for characterisation and optimisation of sar distributions in deep hyperthermia, a plea for standardisation," *International Journal of Hyperthermia*, vol. 25, no. 7, pp. 593–608, 2009.

229. G. G. Bellizzi, T. Drizdal, G. C. van Rhoon, L. Crocco, T. Isernia, and M. M. Paulides, "Predictive value of sar based quality indicators for head and neck hyperthermia treatment quality," *International Journal of Hyperthermia*, vol. 36, no. 1, pp. 456–465, 2019.

230. M. Kroesen, H. T. Mulder, J. van Holthe, A. Aangeenbrug, J. Mens, H. van Doorn, M. M. Paulides, E. Oomen-de Hoop, R. Vernhout, L. Lutgens, *et al.*, "The effect of the time interval between radiation and hyperthermia on clinical outcome in 400 locally advanced cervical carcinoma patients," *Frontiers in oncology*, vol. 9, p. 134, 2019.

231. D. E. Thrall, S. M. LaRue, D. Yu, T. Samulski, L. Sanders, B. Case, G. Rosner, C. Azuma, J. Poulson, A. F. Pruitt, *et al.*, "Thermal dose is related to duration of local control in canine sarcomas treated with thermoradiotherapy," *Clinical Cancer Research*, vol. 11, no. 14, pp. 5206–5214, 2005.

232. E. Jones, D. Thrall, M. W. Dewhirst, and Z. Vujaskovic, "Prospective thermal dosimetry: the key to hyperthermia's future," *International Journal of Hyperthermia*, vol. 22, no. 3, pp. 247–253, 2006.

233. J. Gellermann, H. Faehling, M. Mielec, C. H. Cho, V. Budach, and P. Wust, "Image artifacts during mrt hybrid hyperthermia - causes and elimination," *International Journal of Hyperthermia*, vol. 24, no. 4, pp. 327–335, 2008.

234. M. Johannsen, U. Gneveckow, L. Eckelt, A. Feussner, N. Waldöfner, R. Scholz, S. Deger, P. Wust, S. A. Loening, and A. Jordan, "Clinical hyperthermia of prostate cancer using magnetic nanoparticles: presentation of a new interstitial technique," *International journal of hyperthermia*, vol. 21, no. 7, pp. 637–647, 2005.

235. N. van den Tempel, C. Laffeber, H. Odijk, W. A. van Cappellen, G. C. van Rhoon, M. Franckena, and R. Kanaar, "The effect of thermal dose on hyperthermia-mediated inhibition of dna repair through homologous recombination," *Oncotarget*, vol. 8, no. 27, p. 44593, 2017.

236. S. Curto, B. Aklan, T. Mulder, O. Mils, M. Schmidt, U. Lamprecht, M. Peller, R. Wessalowski, L. H. Lindner, and R. Fietkau, "Quantitative, multi-institutional evaluation of mr thermometry accuracy for deep-pelvic mr-hyperthermia systems operating in multivendor mr-systems using a new anthropomorphic phantom," *Cancers*, vol. 11, no. 11, p. 1709, 2019.

237. M. M. Paulides, W. C. M. Numan, T. Drizdal, G. Kotek, D. T. B. Yeo, and G. C. Van Rhoon, "Feasibility of mri-guided hyperthermia treatment of head and neck cancer," in *The 8th European Conference on Antennas and Propagation (EuCAP 2014)*, pp. 1474–1477, IEEE, 2014.

238. M. V. Kulkarni, J. A. Patton, and R. R. Price, "Technical considerations for the use of surface coils in mri," *American Journal of Roentgenology*, vol. 147, no. 2, pp. 373–378, 1986.

239. G. Schooneveldt, H. Dobíek Trefná, M. Persson, T. M. De Reijke, K. Blomgren, H. P. Kok, and H. Crezee, "Hyperthermia treatment planning including convective flow in

cerebrospinal fluid for brain tumour hyperthermia treatment using a novel dedicated paediatric brain applicator," *Cancers*, vol. 11, no. 8, p. 1183, 2019.

240. T. W. Eigentler, L. Winter, H. Han, E. Oberacker, A. Kuehne, H. Waiczies, S. Schmitter, L. Boehmert, C. Prinz, and H. D. Trefna, "Wideband selfgrounded bowtie antenna for thermal mr," *NMR in Biomedicine*, 2020.

241. E. Minalga, A. Payne, R. Merrill, N. Todd, S. Vijayakumar, E. Kholmovski, D. L. Parker, and J. R. Hadley, "An 11channel radio frequency phased array coil for magnetic resonance guided highintensity focused ultrasound of the breast," *Magnetic resonance in medicine*, vol. 69, no. 1, pp. 295–302, 2013.

242. R. Deckers, L. G. Merckel, B. D. de Senneville, G. Schubert, M. Köhler, F. M. Knuttel, W. P. T. M. Mali, C. T. W. Moonen, M. van den Bosch, and L. W. Bartels, "Performance analysis of a dedicated breast mr-hifu system for tumor ablation in breast cancer patients," *Physics in Medicine and Biology*, vol. 60, no. 14, p. 5527, 2015.

243. M. M. Paulides, J. F. Bakker, A. P. M. Zwamborn, and G. C. Van Rhoon, "A head and neck hyperthermia applicator: Theoretical antenna array design," *International journal of hyperthermia*, vol. 23, no. 1, pp. 59–67, 2007.

244. K. P. Pruessmann, M. Weiger, M. B. Scheidegger, and P. Boesiger, "Sense: sensitivity encoding for fast mri," *Magnetic Resonance in Medicine: An Official Journal of the International Society for Magnetic Resonance in Medicine*, vol. 42, no. 5, pp. 952–962, 1999.

245. S. Moeller, E. Yacoub, C. A. Olman, E. Auerbach, J. Strupp, N. Harel, and K. Uurbil, "Multiband multislice geepi at 7 tesla, with 16fold acceleration using partial parallel imaging with application to high spatial and temporal wholebrain fmri," *Magnetic resonance in medicine*, vol. 63, no. 5, pp. 1144–1153, 2010.

246. C. J. Ferrer, L. W. Bartels, T. A. van der Velden, H. Grüll, E. Heijman, C. T. W. Moonen, and C. Bos, "Field drift correction of proton resonance frequency shift temperature mapping with multichannel fast alternating nonselective free induction decay readouts," *Magnetic Resonance in Medicine*, vol. 83, no. 3, pp. 962–973, 2020.

247. V. N. Harry, S. I. Semple, F. J. Gilbert, and D. E. Parkin, "Diffusion-weighted magnetic resonance imaging in the early detection of response to chemoradiation in cervical cancer," *Gynecologic oncology*, vol. 111, no. 2, pp. 213–220, 2008.

248. I. VilasBoas-Ribeiro, P. A. Wielopolski, F. Martine, J. A. Hernandez-Tamames, G. C. van Rhoon, and M. M. Paulides, "Potential impact of mr-only treatment planning in mr guided deep pelvic hyperthermia," in *European Society for Hyperthermic Oncology (ESHO), 2019 33rd Annual Meeting of the European Society for Hyperthermic Oncology*, ESHO, 2019.

249. V. Murthy, Z. Master, P. Adurkar, I. Mallick, U. Mahantshetty, G. Bakshi, H. Tongaonkar, and S. Shrivastava, "plan of the dayadaptive radiotherapy for bladder cancer using helical tomotherapy," *Radiotherapy and Oncology*, vol. 99, no. 1, pp. 55–60, 2011.

250. U. Katscher and C. A. T. van den Berg, "Electric properties tomography: biochemical, physical and technical background, evaluation and clinical applications," *NMR in Biomedicine*, vol. 30, no. 8, p. e3729, 2017.

251. J. Liu, Y. Wang, U. Katscher, and B. He, "Electrical properties tomography based on b_1 maps in mri: Principles, applications, and challenges," *IEEE Transactions on Biomedical Engineering*, vol. 64, no. 11, pp. 2515–2530, 2017.

252. Y. P. Du and Z. Jin, "Simultaneous acquisition of mr angiography and venography (mrav)," *Magnetic Resonance in Medicine: An Official Journal of the International Society for Magnetic Resonance in Medicine*, vol. 59, no. 5, pp. 954–958, 2008.

List of Publications

International journal articles

EA Raaijmakers, RM Mestrom, **K Sumser**, G Salim, GC van Rhoon, J Essers, MM Paulides. An MR-compatible antenna and application in a murine superficial hyperthermia applicator. *International Journal of Hyperthermia*. 2018 Aug 18;34(6):697-703.

K Sumser, E Neufeld, RF Verhaart, V Fortunati, GM Verduijn, T Drizdal, T van Walsum, JF Veenland, MM Paulides. Feasibility and relevance of discrete vasculature modeling in routine hyperthermia treatment planning. *International Journal of Hyperthermia*. 2019 Jan 1;36(1):800-810.

F Adibzadeh*, **K Sumser***, S Curto, DT Yeo, AA Shishegar, MM Paulides. Systematic review of pre-clinical and clinical devices for magnetic resonance-guided radiofrequency hyperthermia. *International Journal of Hyperthermia*. 2020 Jan 1;37(1):15-27.
*Both authors contributed equally to this paper.

K Sumser, GG Bellizzi, GC van Rhoon, MM Paulides. The Potential of Adjusting Water Bolus Liquid Properties for Economic and Precise MR Thermometry Guided Radiofrequency Hyperthermia. *Sensors*. 2020 Jan;20(10):2946.

GG Bellizzi, **K Sumser**, I VilasBoas-Ribeiro, S Curto, T Drizdal, GC van Rhoon, M Franckena, MM Paulides. Standardization of patient modeling in hyperthermia simulation studies: introducing the Erasmus Virtual Patient Repository. *International Journal of Hyperthermia*. 2020 Jan 1;37(1):608-616.

K Sumser*, GG Bellizzi*, R Forner, T Drizdal, JA Hernandez-Tamames, GC Van Rhoon, MM Paulides. Dual-Function MR-guided Hyperthermia: An Innovative Integrated Approach and Experimental Demonstration of Proof of Principle. *IEEE Transactions on Biomedical Engineering*. 2020 Jul 29.
*Both authors contributed equally to this paper.

L Farina, **K Sumser**, GC van Rhoon, S Curto. Thermal Characterization of Phantoms Used for Quality Assurance of Deep Hyperthermia Systems. *Sensors*. 2020 Aug;20(16):4549.

GG Bellizzi, **K Sumser**, MT Bevacqua. On The Optimal Matching Medium and The Working Frequency in Deep Pelvic Hyperthermia. *IEEE Journal of Electromagnetics, RF and Microwaves in Medicine and Biology*. 2020 Dec 29, (Early Access).

T Drizdal, **K Sumser**, GG Bellizzi, O Fiser, J Vrba, GC van Rhoon, DTB Yeo, MM Paulides, Simulation guided design of the MRcollar: a MR compatible applicator for deep heating in the head and neck region. *International Journal of Hyperthermia*. 2021 March 7;38(1):382-392.

K Sumser, T Drizdal, GG Bellizzi, GC van Rhoon, JA Hernandez-Tamames, MM Paulides, Experimental Validation of an MR-Compatible Head and Neck Hyperthermia Applicator. *International Journal of Hyperthermia*. In preparation.

International conferences articles

K Sumser, A Geerman, J Haeck, M Bernsen, GC van Rhoon, MM Paulides. Development and in vivo validation of an MR-compatible temperature controllable superficial hyperthermia applicator for small animal studies. *In 2018 EMF-Med 1st World Conference on Biomedical Applications of Electromagnetic Fields (EMF-Med)* 2018 Sep 10 (pp. 1-2). IEEE.

MM Paulides, K Sumser, IV Ribeiro, E Neufeld, GC van Rhoon. Challenges and opportunities in thermal tissue modelling for electromagnetic applications. *In 2019 13th European Conference on Antennas and Propagation (EuCAP)* 2019 Mar 31 (pp. 1-4). IEEE.

K Sumser, MM Paulides, GG Bellizzi, GC van Rhoon, JA Hernandez-Tamames, S Curto. Influence of the BSD-2000 3D/MR hyperthermia applicator on MR Image Quality: A Quantitative Assessment. *In 2020 14th European Conference on Antennas and Propagation (EuCAP)* 2020 Mar 15 (pp. 1-3). IEEE.

GG Bellizzi, K Sumser, MM Paulides. The Required Patient Modeling Realism in Radiofrequency Heating Simulation Studies. *In 2020 14th European Conference on Antennas and Propagation (EuCAP)* 2020 Mar 15 (pp. 1-3). IEEE.

GG Bellizzi, K Sumser, GC van Rhoon, R Forner, MM Paulides. Feasibility of Integrating an MR Receive Coil Array into the MRcollar. *In 2020 XXXIV General Assembly and Scientific Symposium (GASS) of the International Union of Radio Science* 2020 August 29.

International conference abstracts

K Sumser, JA Hernandez-Tamames, GC van Rhoon, MM Paulides. Intravoxel Incoherent Motion Imaging of Thermoregulation in Skeletal Muscle. *In 2018 10th Annual Meeting of International Society of Magnetic Resonance in Medicine Benelux Chapter* 2018 January 26, Antwerp, Belgium.

K Sumser, JA Hernandez-Tamames, GC van Rhoon, MM Paulides. Intravoxel Incoherent Motion Imaging of Thermoregulation in Skeletal Muscle. *In 2018 ISMRM-ESMRMB Joint Annual Meeting of International Society of Magnetic Resonance in Medicine and The European Society for Magnetic Resonance in Medicine and Biology* 2018 June 16-21, Paris, France.

K Sumser, WM Brink, DHJ Poot, MM Paulides. In vivo Temperature Monitoring by Multipeak Multi Echo Modelling PRFS MR Thermometry. *In 2019 11th Annual Meeting of International Society of Magnetic Resonance in Medicine Benelux Chapter* 2018 January 17, Leiden, The Netherlands.

GG Bellizzi, K Sumser, T Drizdal, GC Van Rhoon, JA Hernandez-Tamames, DTC Yeo, MM Paulides. MR guided Head&Neck Hyperthermia: Accuracy Through Integration. *In 2019 STM 36th Annual Society for Thermal Medicine Meeting* 2019 April 28 - May 2, Rotterdam, The Netherlands.

K Sumser, T Drizdal, JA Hernandez-Tamames, GC van Rhoon, GG Bellizzi, MM Paulides. MR thermometry guided RF hyperthermia in the head and neck region does the new MRcollar affect the imaging? *In 2019 ISMRM 27th Annual Meeting of International Society of Magnetic Resonance in Medicine* 2019 May 11-16, Montreal, Canada.

K Sumser, E Neufeld, RF Verhaart, GM Verduijn, T Drizdal, JF Veenland, GC van Rhoon, MM Paulides. Effect Of Discrete Vasculature On Head And Neck Hyperthermia Treatment Quality. *In 33rd ESHO Annual Congress of European Society of Hyperthermic Oncology*. 2019 May 22-24, Warsaw, Poland.

K Sumser, GG Bellizzi, GC van Rhoon, JA Hernandez-Tamames, MM Paulides, S Curto. Effect of the BSD-2000 3D/MR hyperthermia applicator on MR Image Quality. *In 2019 ESMRMB 36th Annual Scientific Meeting of The European Society for Magnetic Resonance in Medicine and Biology* 2020 October 3-5, Rotterdam, The Netherlands.

GG Bellizzi, K Sumser, R Forner, T Drizdal, GC Van Rhoon, JA Hernandez-Tamames, DTC Yeo, MM Paulides. Development of the First Dual-Function Head & Neck Hyperthermia Applicator: The MRcollar. *In 2019 ESMRMB 36th Annual Scientific Meeting of The European Society for Magnetic Resonance in Medicine and Biology* 2020 October 3-5, Rotterdam, The Netherlands.

K Sumser, GG Bellizzi, GC van Rhoon, MM Paulides. The Benefits of Using Fe3O4 Nanoparticles Doped Water in Water Bolus of MR compatible RF Hyperthermia Devices. *In 2020 ESMRMB 36th Annual Scientific Meeting of The European Society for Magnetic Resonance in Medicine and Biology* 2020 September 30 - October 2, Online.

PhD portfolio

PhD portfolio

Name of the Student	Kemal Sumser
Erasmus MC Department	Radiation Oncology
Research School	Molecular Medicine
PhD Period	2016 - 2020
Promoters	Prof. dr. ir. G. C. van Rhoon
	Prof. dr. J.A. Hernandez-Tamames
Copromoter	Dr. ir. M.M. Paulides

	Year	Workload (ECTS)
Courses		
Basic Introduction Course on SPSS	2017	1.0
Translational Imaging Workshop by AMIE: From mouse to man	2017	1.4
Scientific Integrity	2017	0.3
Lectures on MR 2017, Measurement of Perfusion and capillary exchange	2017	1.0
Programming with Python	2017	1.0
Basis Training OpenClinica	2018	0.3
Biomedical English Writing and Communication	2017 - 2018	4.0
1st EMF-Med 2018 Training School on Biomedical Applications of Electromagnetic Fields	2018	1.0
Presentations at international conferences		
Oral Presentation at ISMRM Benelux Chapter Meeting 2018	2018	1.0
Oral Presentation at	2018	1.0

EMF-Med 2018		
Oral Presentation at	2019	1.0
ISMRM Benelux Chapter Meeting 2019		
Oral Presentation at	2019	1.0
ESMRMB 2019		
Poster Presentation at	2018	0.5
ISMRM 2018		
Poster Presentation at	2019	0.5
ISMRM 2019		
Poster Presentation at	2020	0.5
EuCAP 2020		
In-house presentations		
Research Day 2018,	2018	1.0
Department of Radiotherapy		
Journal Clubs (x4)	2017 - 2020	0.4
Referee (x6)	2017 - 2020	0.6
Workshops		
Oral Presentation at	2019	1.0
Thermal Dose Workshop		
Teaching Activities		
Supervising Bachelor Students (x5)	2017 - 2020	15.0

Other teaching activities:

MRI hands on training for technicians, PhD students and resident doctors of Erasmus MC, Department of Radiotherapy.

Reviews

Reviewer for full papers of Cancers, International Journal of Hyperthermia, IEEE Journal of Biomedical and Health Informatics, IEEE Journal of Electromagnetics, RF, and Microwaves in Medicine and Biology, Applied Sciences.

Honors

Cancer EMF Interaction and Applications Best Paper Award at the 1st EMF-Med World Conference on Biomedical Applications of Electromagnetic Fields, Split, Crotia, 2018

ISMRM Trainee Stipend 2018, 2019

COST EMF-MED (Action BM1309) STSM Grant

Member of 12th Annual ISMRM Benelux Chapter Meeting Organizing Committee

Member of the ASME Standards Committee on Thermal Medicine

Curriculum Vitae

Kemal Sumser was born on February 11, 1991 in Ankara, Turkey.

- 1997-2005: Primary school, Nuh Eskiyapan Primary School, Ankara, Turkey.
- 2005-2009: High school, Ankara Ataturk Anatolian High School, Ankara, Turkey.
- 2009-2013: Bachelor in Electrical and Electronics Engineering, Middle East Technical University, Ankara, Turkey.
- 2013-2016: Master of Electrical and Electronics Engineering, Middle East Technical University, Ankara, Turkey.
- 2016-2020: PhD student at Erasmus MC - Cancer Institute, Rotterdam, The Netherlands.
- 2020-...: Post doctoral researcher at Erasmus MC - Cancer Institute, Rotterdam, The Netherlands.

Acknowledgments

Almost five years ago, I started a new chapter in my life with starting my PhD trajectory as a researcher at Erasmus MC, Hyperthermia Unit. The ending of this chapter is marked by this book which would not have happened without the contributions of the following people that was in my life in Rotterdam.

I would like to thank my promotors Prof. dr. Gerard van Rhoon, Prof dr. Juan Hernandez Tamames, and Dr. Maarten Paulides. Dear Gerard, I am grateful to have you as a boss. I admire your approach, attitude, and mannerism. It was a relief knowing that you would find a solution when I had a problem. Dear Maarten, I find myself very lucky that I had you as my co-promoter. You are the ideal supervisor that I imagined before starting my PhD. Your brilliant mind, ideas, guidance, and support made this book possible. Furthermore, you were not only there at work, but also outside of it. You and your family made me feel welcome and let me experience the Dutch culture. Dear Juan, I thank you for collaborating in this project. Your expertise in MRI made this research complete.

I would like to thank Tomas Drizdal. Tomas, even though you were not officially my supervisor, I saw you as one. I am very thankful that you were there when I started my PhD, without you I would feel alone. With your expertise, guidance and teaching, you made working with Sim4Life and python a joy. I admire your love for biking which pushed me to get a bike. And it was a pleasure to have beer with you after work.

I would like to thank Gennaro Bellizzi. Gennaro, when I look back I have nothing but fond memories together. You were my colleague, flat mate but above all you are my friend. I clearly remember the moment after your goodbye party when we made a promise that you will return and we will rent a penthouse in Rotterdam, bargaining with makelaars in Split and spending one and a half year as colleagues and flat mates. We worked, run, ate, and have fun together. I cannot thank you enough for everything. And I am glad that you will be by my side as my paranymph.

I would like thank Daniel de Jong and Ali Ameziane. Without your help, research in Hyperthermia Unit would not be possible. I am thankful that in addition to your clinical duties, you always found time to help me.

I would like to thank my colleagues in Hyperthermia Unit. Sergio, Bob, Iva, Tim, Anderson, Remo, Jannis, Theresa, Rogier, Ellen, Lisa, Andrea, Niels. It was a pleasure to share the workplace with you. I wish you all many occasions that you have to bring a cake.

I would like to thank the students that I had a chance to work with. Dear Anthony, Maarten, Marleen, Annemarije and Hao, I am proud of the work that you have done.

I would like to thank the following people that without their support outside of work, I would not be able to complete this book. Dear Gizem, after we left Ankara, out of thousands of possibilities, we ended up in the same city. It feels assuring to have a piece of what you left behind nearby. I am thankful to have you in Rotterdam.

Dear Sharlene, when I look back in my time in Rotterdam, I see a lot of you. We spent thousands of kilometers running together. We shared a lot of good and bad moments. Thank you for bringing color to my life. Your brush shaped me who I am today. You are a wonderful person.

Dear Rosa, I havent met anyone who is as caring, thoughtful and dedicated as you are. I am thankful that you were with me to get me to the end. I find comfort when you are by my side. I hope you will always be there.

Dear Buğra and Cem, the time that I know you is now longer than the time that I dont. I am grateful for the friendship that we have.

I would like to thank Tunay, Burak Ü, İren, Burak A, Fırat, Can, Kaan, Eralp and Tayfun for holding their promise and visiting me in the Netherlands.

Necmiye Yenge, ülkemden uzakta, ailemden birine yakın olduğum için çok şanslıyım. Bana kendi oğlun gibi davrandığın için sana çok teşekkür ederim.

Son olarak aileme teşekkür etmek istiyorum. Anne ve Baba, sizlerin emekleri olmasaydı, bu satırları yazma fırsatına asla sahip olamazdım. Size ne kadar teşekkür edersem edeyim, hakkınızı ödeyemeyeceğimi biliyorum. Abla, birbirimizin yakınında olamasak da, aklında ve düşüncelerinde yakın olduğumuzu biliyorum ve bunun için minnettarım.